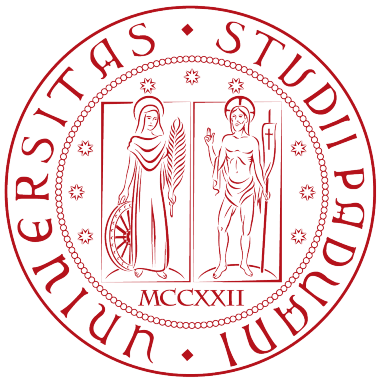

Università di Padova

Dipartimento di Fisica e Astronomia

Laura Magistrale in Fisica

A HOMODYNE QUADRATURE INTERFEROMETER FOR THE STUDY OF THERMAL NOISE IN SOLIDS IN NON-EQUILIBRIUM STEADY STATES

Relatore
Chiar.mo Prof.
Giacomo Ciani
Co-relatore:
Chiar.ma dott.ssa
Livia Conti

Candidato:
Alvise Pizzella

Anno Accademico 2017/2018

to my grandfather Guido..

measure

etimology: italian *misura*, french *mésure*, latin MENSURA, coming from MENSUS, past participle of the verb METÍRI meanint *to measure*. This verb has its origins in the indoeuropean root $MA\hat{A}$; to be compared with the sanscrit *mâti* meaning *measure, to measure*, $mâtram$ = greek mètron, slavish and serbian *mata*, celtic *mead, meas*, ancient alt german *mëz*, *mâza* and the modern $Maas$, ancient german *mezzan* and modern *messen*, gotic *mitan* *mäta*.

This root can also be found in the words *meter* - the fundamental unit to measure lenghts, *imitate, mimic* - the act of 'measuring' someone or something in order to reproduce it, *mathematics* (since this root gained also the metaphorical meaning of "thinking", *moon* - since the lunar period was the fundamental unit to measure *months*' duration - and hence *month*.

Contents

Introduction **7**

1 Gravitational Waves Detection **9**
1.1 Gravitational Waves 9
1.2 Gravitational Waves Experiments 12
1.2.1 Resonant Bar Detectors 12
1.2.2 Gravitational Waves Interferometers 14
1.3 The Detected GW signals 17

2 Thermal Noise and Thermodynamic Equilibrium **21**
2.1 Thermal Noise 21
2.2 Thermal Noise in GW Interferometers 23
2.3 The "Rarenoise" Experiment 23

3 The Interferometric Readout **29**
3.1 The Intensity Signals - Ideal Case 31
3.2 The Ideal Two Photodiodes Readout 33
3.3 The Intensity Signals - Realistic Case 34
3.4 The Realistic Two Photodiodes Readout (2PDR) 35
3.5 The Realistic Three Photodiodes Readout (3PDR) 36
3.6 The Four Photodiodes Phase Readout (4PDR) 37

4 Interferometer's Testing **39**
4.1 Laser Beam 39
4.2 Interferometer Bench 45
4.3 Bench Test of the Interferometer 46
4.4 Test Setup Sensitivity to Temperature 53

5 Interferometric Measurement of the Oscillator's Motion **57**
5.1 The Experimental Setup 57
5.1.1 Heater 57
5.1.2 The Mechanical Filter 57
5.1.3 The Vacuum System 58
5.1.4 Interferometer Setup 61
5.1.5 Acquisition System 61
5.2 Noise Budget 65
5.3 Three Photodiodes Phase Readout Results 67
5.4 Four Photodiodes Phase Readout Results 70
5.5 Measurement of the Heated Oscillator 75

5.6 Oscillator Modes' Peaks 77
5.7 Future Improvements 83

Conclusions **85**

A Power Spectral Density **86**

B Phase Unwrapping **87**

C Gaussian Beams **89**

D Optics Formalism: Jones Calculus **91**

E Optics Characterization **94**
E.1 Power Beam Splitter Lambda Research Optics NPB-25.4B-R1064-50 used as BS1 94
E.2 Power Beam Splitter Lambda Research Optics NPB-25.4B-R1064-50 used as return interceptor 96
E.3 Phase Offset induced by the Beam Splitters 96
E.4 Aluminum Reflectance Characterization 98
E.4.1 Aluminum Surface 98
E.4.2 Oscillator's Surface Reflectance 98
E.5 Reference Mirror Reflectance 100
E.6 The Octal-Wave Plate 100
E.7 The Photodiodes Calibrations 102

Introduction

Modern gravitational waves interferometers are currently limited in mid and low frequencies by the thermal noise. Thermal noise is modeled by means of the fluctuation dissipation theorem, which itself sits on the hypothesis of thermodynamic equilibrium. However, the suspension fibers and mirrors, whose thermal noise affects the sensitivity operate rather in non equilibrium condition, due to heat fluxes generated by the absorbed laser power and by thermal compensation techniques. So far, the theoretical knowledge of thermal noise extends only to the thermodynamical equilibrium condition, whereas the nonequilibrium condition has been little explored.

On the other hand, nonequilibrium driving is expected to increase in the future generations of interferometers: thus it is now mandatory to understand what the impact would be on the estimation of the thermal noise. Some measurements in conditions similar to those in GW detectors have already been performed in a metal system by the 'Rarenoise' experiment, within the VIRGO collaboration. Measurements suggested that in a nonequilibrium state the noise can depend not only on the (local) thermodynamic temperature but also on the heat flux. However, the outcome of somewhat similar measurements on silicon differ.

What is then needed is a phenomenological relation between the thermal noise level and the parameters that characterize the non-equilibrium condition. A better comprehension of this problem would help the future interferometer's design, so to minimize heat fluxes if they prove to affect the thermal noise level. For example, the beam size could be re-defined in order to minimize the temperature gradients in the mirrors.

In this thesis I am going to collaborate with the Rarenoise experiment. The target is to try to improve the 'Rarenoise' experiment by substituting its previously used capacitive readout with an interferometric one. The capacitive measurements were affected by a systematic error due to calibration issues. The interferometric readout should be instead independent on this. I am going to build and characterize the interferometric readout setup, bringing its sensitivity down to the desired level of $10^{-29} m^2/Hz$ in the 100-2000 Hz frequency band.

Chapter 1

Gravitational Waves Detection

1.1 Gravitational Waves

I will summarize here the basic concepts about Gravitational Waves (GW). For a more general argumentation see [7] or [8].

GW have been predicted by Albert Einstein in 1915 in the context of the General Relativity theory. Thanks to the equivalence principle, gravity is no longer described as a distance interaction between massive bodies but as the curvature of the space-time's geometry induced by the mass and energy distribution. The spacetime is described as a Riemannian manifold, whose properties are summarized in the symmetric *metric tensor* $g_{\mu\nu}(x)$. Einstein's field equations [1.1] relate the energy-momentum tensor $T_{\mu\nu}(x)$ to the metric tensor as it follows:

$$R_{\mu\nu} - \frac{1}{2}Rg_{\mu\nu} = \frac{8\pi G}{c^4}T_{\mu\nu} \tag{1.1}$$

where G is Newton's constant, c is the speed of light, $R_{\mu\nu}$ is the Ricci tensor and R is the Ricci scalar. The constant on the right hand side is very small: $\frac{8\pi G}{c^4} \approx 2.071 \times 10^{-43} s^2 m^{-1} kg^{-1}$, and so a huge amount of matter and energy density is needed to influence the spacetime's curvature. In absence of matter, the metric $g_{\mu\nu}(x)$ reduces to the flat Minkowsky metric $\eta_{\mu\nu}$ = diag(-1, 1, 1, 1).

GWs emerge when trying to study the small perturbations of a metric. For simplicity the flat metric is chosen. In the *weak field approximation* the matter-energy density contribution is very small, and the metric $g_{\mu\nu}$ will be barely different from the flat Minkowsky metric. The small deviation from the flat metric can be enclosed in a symmetric tensor $h_{\mu\nu}$ which respects the following equations:

$$g_{\mu\nu} = \eta_{\mu\nu} + h_{\mu\nu} \qquad |h_{\mu\nu}| << 1 \qquad |\partial_\mu h_{\nu\rho}| << 1 \tag{1.2}$$

The field equations [1.1] can be then linearized, and after some mathematical computations, one can obtain a wave equation for the tensor $\bar{h}_{\mu\nu} = h_{\mu\nu} - \frac{1}{2}\eta_{\mu\nu}h^\rho_\rho$:

$$\Box\bar{h}_{\mu\nu} = \frac{8\pi G}{c^4}T_{\mu\nu} \tag{1.3}$$

where $\Box$ is defined as the flat space d'Alambertian $\Box = \eta_{\mu\nu}\partial^\mu\partial^\nu$, along with the condition $\partial^\mu\bar{h}_{\mu\nu} = 0$ (transverse condition). Equation 1.3 is the basic result for computing the generation of GWs within linearized theory. To study the propagation or the interaction with test masses of GWs we are interested to a solution in vacuum ($T_{\mu\nu}(x) = 0$), which turns out to be:

$$\Box\bar{h}_{\mu\nu} = 0 \tag{1.4}$$

This equation can be solved with the Green function method, and one can obtain

$$\bar{h}_{\mu\nu} = A_{\mu\nu} e^{ik_\rho x^\rho} \tag{1.5}$$

along with the conditions $k^\mu A_{\mu\nu} = 0$ (transverse condition), $k_\rho k^\rho = 0$ (light speed propagation). Freedom in the gauge choice can be used to set the trace $\bar{h}$ to 0, making the wave tensor Transverse and Traceless (TT gauge). For a wave propagating in the z direction $k = (1, 0, 0, 1)$ and the solution in this gauge is then:

$$\bar{h}^{TT}_{\mu\nu} = \begin{pmatrix} 0 & 0 & 0 & 0 \\ 0 & h_+ & h_\times & 0 \\ 0 & h_\times & -h_+ & 0 \\ 0 & 0 & 0 & 0 \end{pmatrix} e^{i\omega(t-\frac{z}{c})} \tag{1.6}$$

where ω is the gravitational wave's frequency and $t - \frac{z}{c}$ is the retarded time, since the waves take time to propagate. As shown, two degrees of freedom are left, as in the case of the electromagnetic waves. The resulting wave is a superposition of two polarizations, named respectively + (plus) and × (cross). By defining two polarization tensors ϵ_+ and $\epsilon_\times$

$$\epsilon^+_{\mu\nu} = \begin{pmatrix} 0 & 0 & 0 & 0 \\ 0 & 1 & 0 & 0 \\ 0 & 0 & -1 & 0 \\ 0 & 0 & 0 & 0 \end{pmatrix} \qquad \epsilon^\times_{\mu\nu} = \begin{pmatrix} 0 & 0 & 0 & 0 \\ 0 & 0 & 1 & 0 \\ 0 & 1 & 0 & 0 \\ 0 & 0 & 0 & 0 \end{pmatrix} \tag{1.7}$$

a generic wave can be written as

$$\bar{h}^{TT}_{\mu\nu} = \sum_{i=+,\times} h_i \epsilon^i_{\mu\nu} e^{i\omega(t-\frac{z}{c})} \tag{1.8}$$

The physical effect of GWs is the following: due to a GW's transit, the metric varies:

$$\eta_{\mu\nu} + GW \to g_{\mu\nu} = \eta_{\mu\nu} + h^{TT}_{\mu\nu} = \begin{pmatrix} -1 & 0 & 0 & 0 \\ 0 & 1 + h_+ cos(\omega(t - \frac{z}{c})) & h_\times cos(\omega(t - \frac{z}{c})) & 0 \\ 0 & h_\times cos(\omega(t - \frac{z}{c})) & 1 - h_+ cos(\omega(t - \frac{z}{c})) & 0 \\ 0 & 0 & 0 & 1 \end{pmatrix} \tag{1.9}$$

The proper distance between two points at rest is then modified. Considering only the + polarization and two events $\mathbf{x_1} = (ct, x_1, 0, 0)$, $\mathbf{x_2} = (ct, x_2, 0, 0)$, $\mathbf{\Delta x} = (0, x_1 - x_2, 0, 0)$, one can obtain:

$$s^2 = \eta_{\mu\nu}\Delta x^\mu \Delta x^\nu + h^{TT}_{\mu\nu}\Delta x^\mu \Delta x^\nu \to s \approx (x_1 - x_2)\left(1 + \frac{1}{2} h_+ cos(\omega t)\right) \tag{1.10}$$

This means that the proper distance between the two events is changing with time. In the general case we can say that the amplitude of the wave is elongation ratio $h \sim \frac{\Delta L}{L}$.

The polarization's name is due to the effect they singularly have on a a ring of particles lying on a plane perpendicular to the propagation direction as shown in figure 1.1

As for electromagnetic (EM) radiation , GW radiation is expected to span a wide range of frequencies, depending on the source.

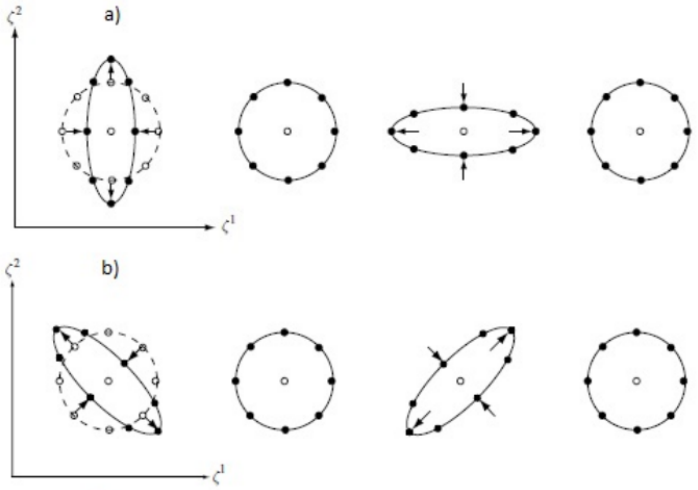

Figure 1.1: The effect of + wave (a) and a × wave (b) propagating in direction ζ_3 and hitting a ring of matter lying on the plane defined by ζ_1 and ζ_2 during one wave cycle. The picture shows the wave's effect when ωt is equal respectively to 0, $\pi/2$, π and $3\pi/2$. The effect of the two polarization is the same, but one is rotated with respect to the other one by a $\frac{\pi}{4}$ angle on the ring's plane [8] (figure from [8]).

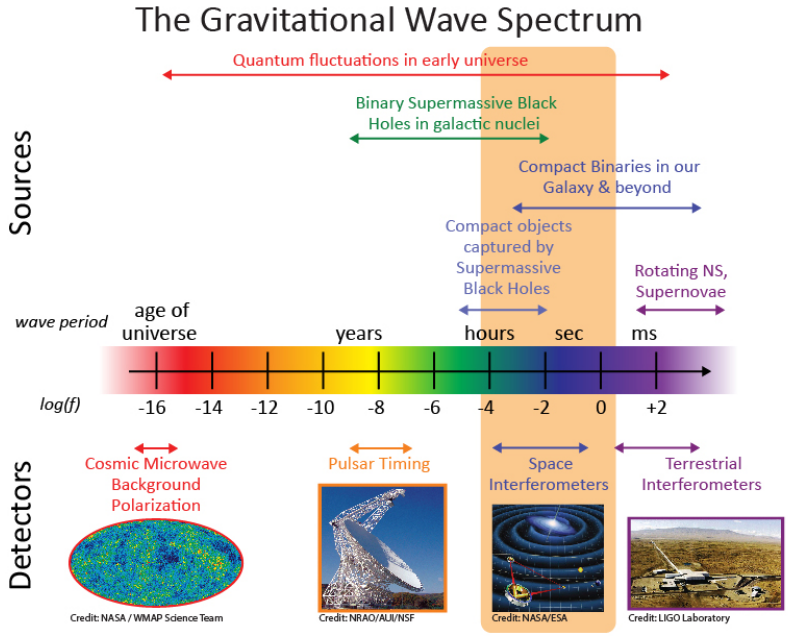

Figure 1.2: The expected Gravitational Waves Spectrum, with expected sources and current (or proposed) detection methods. The currently ground-based interferometers are sensible to GWs in the acoustic band, generated by black holes binaries, neutron star binaries and stellar supernovas [7]. The planned LISA space interferometer will be sensible at low frequencies to waves expected to be generated by super massive black holes [**?**]. To measure even lower frequencies pulsar timing arrays are used: taking advantage or their very regular spinning period, they are perfect clocks. If a GW passes between the pulsar and the earth, an anomaly in the pulsar's periodicity would be seen [15]. GWs are also expected to have been generated by quantum fluctuations in the early universe, and to generate a stochastic GW background as the CMB does with EM waves [16] (figure from [**?**]).

1.2 Gravitational Waves Experiments

Since the prediction by Einstein, physicists have inquired if there could be some physical effect associated to gravitational waves, or if they were just an artifact caused by a bad coordinate choice, i.e. they could be set to zero with an appropriate coordinate change [7]. After more than four decades of debate, most of the scientific community concluded that the gravitational waves should have been a physical reality and one could attempt to measure them [1]. The technological advances of the 40's and the 50' made it also feasible to start some new gravitational experiments [1].

1.2.1 Resonant Bar Detectors

The first experiment for the detection of GW was realized by Joseph Weber. He tried to "measure the Riemann tensor" [2] using resonant aluminum bars.

The detection principle is the following: an aluminum bar is a high quality factor oscillator, whose mechanical modes are going to be excited by a transiting GW. Each mode of the bar can be studied independently. The most relevant one is the lowest frequency longitudinal mode, since it has a higher quadrupole moment, and it is therefore the mode which the GW transfers more of it's energy to. The interaction can be explained by simplifying the bar's structure to that of two of points separated by a distance r and coupled by a spring. As a GW passes by, each of the two points is going to try to follow its own geodesic, but the spring is being so elongated, and the force applied by her would try to get the points back. One can demonstrate, from the geodesic deviation equation, that under the effect of a gravitational wave a particle accelerates as if under the effect of a newtonian force

$$F_{GW,\,i} = \frac{m}{2}\ddot{h}_{ij}^{TT}\zeta^j \tag{1.11}$$

where ζ^i is a vector indicating the point's spatial position. This effect is resumed in the following equation which puts together acceleration, dissipation force, restoring force, external force caused by the GW and external force caused by noise (b is the dissipation factor, m is the mass of each point, k is the spring's constant) [17]:

$$\ddot{\zeta} + \frac{b}{m}\dot{\zeta} + \frac{k}{m}\zeta = \frac{1}{m}(F_{GW} + F_N) \tag{1.12}$$

Resonant bars were huge and heavy ($\sim$ 3 tons) high quality aluminum cylinders [17]. The size was chosen to maximize the GW cross section [17]. The frequency of the first longitudinal mode determines the frequency the bar is most sensible to. The resonance frequency was around 1 kHz, which also was the expected wave frequency of supernovae GW emission [17].

The most relevant issue of these detectors was *thermal noise*. The average square amplitude of oscillation of a cylindrical bar due to thermal fluctuations (Brownian-noise forces or Langevin forces) was many orders of magnitude larger than the oscillation amplitudes induced by an expected gravitational wave [1]. To solve this, in the idea was to cool down the resonant bars to cryogenic temperatures $\sim 4K$. Anyway, the bar's noise was still dominated by the thermal noise (both thermo-mechanical and thermo-electrical). The noise in the amplifier were other important noise sources (figure 1.4).

AURIGA and NAUTILUS have been the most sensitive resonant GW detectors. Up to now, resonant bars have made no confirmed detections, and they have been dismissed because they have been overcome by the GW interferometers.

Figure 1.3: The NAUTILUS cryogenic resonant detector (open), installed at the "Laboratori Nazionali di Frascati" (INFN) in the years 1994-2016 operating at 2 K. [1].

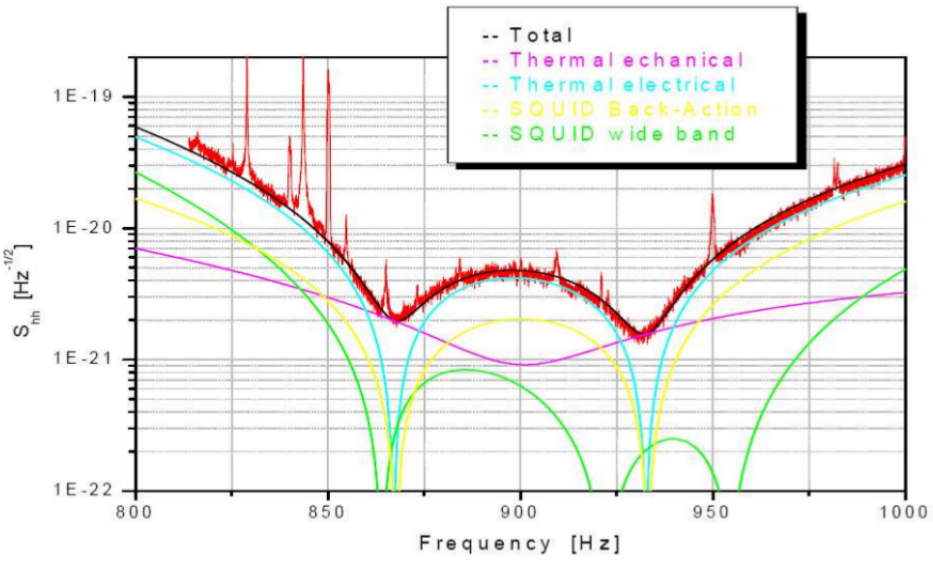

Figure 1.4: Power spectral density of the cryogenic AURIGA detector, installed at the "Laboratori Nazionali di Legnaro" (INFN) in the years 1998-2016 operating a 4.5 K [1].

1.2.2 Gravitational Waves Interferometers

Currently interferometry is the physical principle used to detect GWs in the acoustic band. Since GWs stretch and contract distances (as in figure 1.1), interferometry can be used to precisely measure if the relative length of two perpendicular paths changes in time due to the transit of a GW . The used scheme is that of a Michelson Interferometer. In the simplest case, it consists in a laser source, a beam splitter, two mirrors and a photodiode (a simple scheme is reported in figure 1.6(a)).

(a) The VIRGO interferometer in Cascina, near Pisa, Italy

(b) The LIGO interferometers in Hanford (Wasington, left) and Livingston (Louisiana, right) in the United States

Figure 1.5: Pictures of the three currently active ground-based interferometers [**?**].

The operation is as follows: let the incoming beam be $E(r) = E_0 e^{i(kz-\omega t)}$ (where $k = \frac{2\pi}{\lambda}$ is the wave vector, λ is the laser's wavelength, and z a length parameter along the beam's path). The beam's intensity is then $I_0 \propto EE^* = |E|^2$. The beam is splitted by a 50% power beam splitter (BS), obtaining two different beams ($U_1(r)$ and $U_2(r)$) propagating along the two arms, long respectively L_1 and L_2 and forming a 90° angle between them. The beams are reflected back by the two mirrors at the end of the arms, then they are recombined in the beam splitter and finally hit the photodiode, where the outcoming intensity I_{out} is readed. If the two beams have the opposite phase (modulo 2π) at recombination, the intensity on the photodiode is the same as the one entering the interferometer. If the length of the two arms is different, the two beams have a different phase at recombination, and we see interference. The two beams, once they have gone back and forth the two arms and recombine at the BS,

singularly are

$$L_1(t) \to E_1(r) = \frac{1}{2} E_0 e^{i(kz-\omega t)} e^{i2kL_1(t)} \tag{1.13}$$

$$L_2(t) \to E_2(r) = \frac{1}{2} E_0 e^{i(kz-\omega t)} e^{i2kL_2(t)} \tag{1.14}$$

$$\tag{1.15}$$

The outcoming beam is the superposition of two beams which have a phase difference between them. The intensity readed by the photodiode is then:

$$\begin{aligned} I_{out}(t) &= |E_1(r) + E_2(r)|^2 = |E_1(r)|^2 + |E_2(r)|^2 + E_1(r)E_2(r)^* + E_1(r)^* E_2(r) \\ &= \frac{1}{2}E_0^2 - \frac{1}{2}E_0^2 cos(2k(L_2(t) - L_1(t))) \\ &= \frac{1}{2} I_0 (1 - cos(2k\Delta L(t)\,) \end{aligned} \tag{1.16}$$

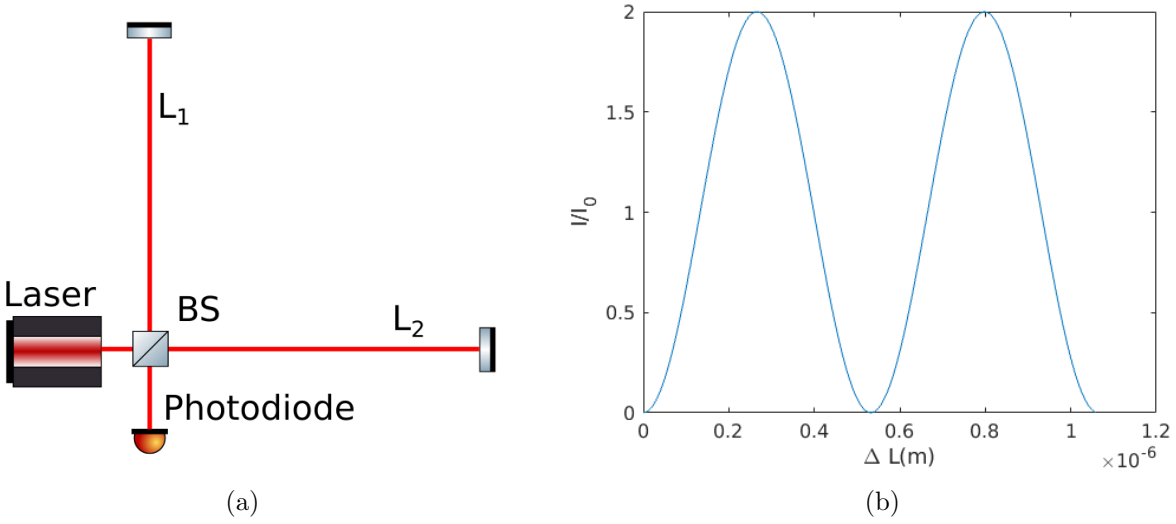

(a) (b)

Figure 1.6: Left: A simple Michelson interferometer scheme, consisting in a laser source, a beam splitter, two mirrors and a photodiode. Right: Plot of the ideal intensity output in function of the relative displacement ΔL by an interferometer in equation (1.16).

As we can see, the phase difference $\Delta\phi(t) = 2k(L_2(t) - L_1(t)) = \frac{4\pi}{\lambda}\Delta L(t)$ originates a modulation in $I_{out}(t)$, which is now a periodic function of the displacement ΔL, varying from 0 to I_0 and with period equal to $\frac{\lambda}{2}$. When $I_{out} = 0$ we have a dark fringe, and when $I_{out} = I_0$ we have a white fringe. If the phase increases by 2π, the relative position changes, but the output does not. Looking at the output in figure 1.6(b), in this case a fringe is said to have been crossed.

Of course the reality is much more complicated than this, and many other devices are being added in order to measure that $\frac{\lambda}{2} \approx 1\mu m$ displacement with a 10^{-12} resolution in the desired frequency band of 100-1000Hz in the $10^3 m$ long arms of the currently used interferometers, and reach the expected strain of $h = \frac{\Delta L}{L} = 10^{-21}$.

With general relativistic computation, [7] demonstrates that the phase difference induced by a + polarized GW to the laser beams in the two arms if the arms lie respectively on the

x and y axis and the wave propagates along z is

$$\Delta\phi_{gw} = \omega_l \frac{2L}{c} h_0 \, cos\left(\omega_{gw} t + \frac{L}{c}\right) sinc\left(\frac{\omega_{gw} L}{c}\right) \tag{1.17}$$

where L is the length of the two arms, ω_l is 2π times the laser beam's frequency and ω_{gw} is 2π times the gravitational wave's frequency. This is the case, if we have only one polarization propagating perpendicularly to the detector's plane. In this condition the detector is completely insensible to the other polarization, since the two arms would be elongated and contracted simultaneously in the same way. More in general one can calculate the antenna pattern of the interferometer applying two rotation matrices and obtain (a shown in [7])

$$h(t) = \frac{1}{2}(1 + cos^2(\theta))cos(2\phi)h_+(t) + cos(\theta)sin(2\phi)h_\times(t) \tag{1.18}$$

The antenna pattern is shown in figure 1.7: where θ and ϕ are respectively the zenith and azimuthal angles of the GW source.

Figure 1.7: The antenna pattern for an interferometer decomposed into its sensitivity in the + polarization (left) and the × polarization (right) [5].

The main noise sources affecting interferometers are the *quantum noise* form the laser beam, gravity gradients from the earth and again *thermal noise*, in the mirror coatings and in the mirror suspension. The noise spectrum of VIRGO and LIGO is reported in figure 1.8:

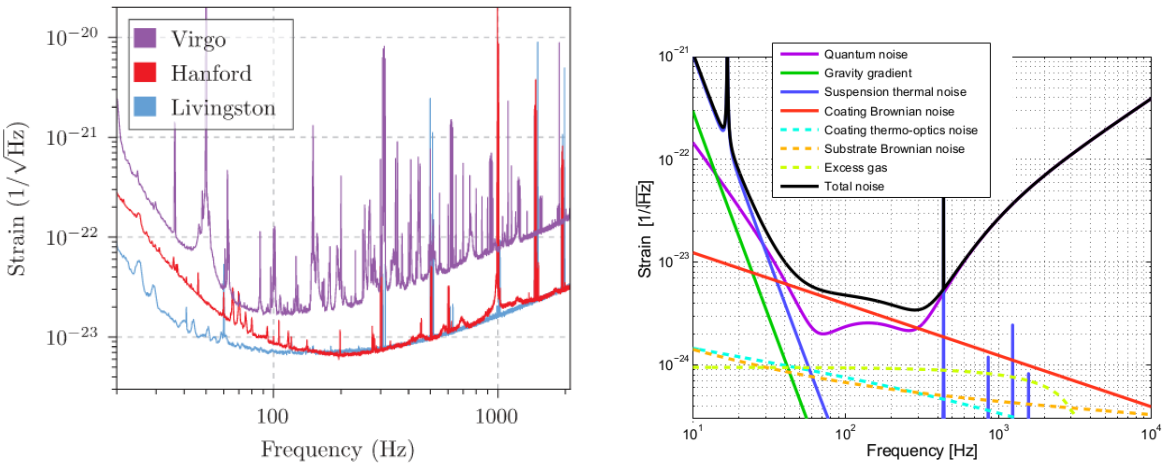

(a) The noise spectrum of both LIGO and VIRGO [21]

(b) The estimated noise causes in the VIRGO detector. Note the blue and the red line, which indicate the thermal noise contribution. [4].

Figure 1.8: The noise in the LIGO and VIRGO detectors

As shown in this plot, the thermal noise in the suspension system and in the mirror coatings is limiting the sensitivity of the interferometer at mid and low frequency.

1.3 The Detected GW signals

Anyway the sensitivity reached by the interferometers was high enough that after one hundred years of experimental effort, on September 14, 2015 the event called GW140915 was finally detected by the LIGO interferometers (figure 1.9). The signal came from a black hole binary merger, and corresponded to a relative displacement of the interferometer arms at the level of 10^{-18}m [18]. Since it was detected only by two interferometers, the sky location of the event primarly determinated by the relative time arrival of the signal, and the 90% confidence level sky area was of 600 deg^2 [18] (figure 1.10(b)).

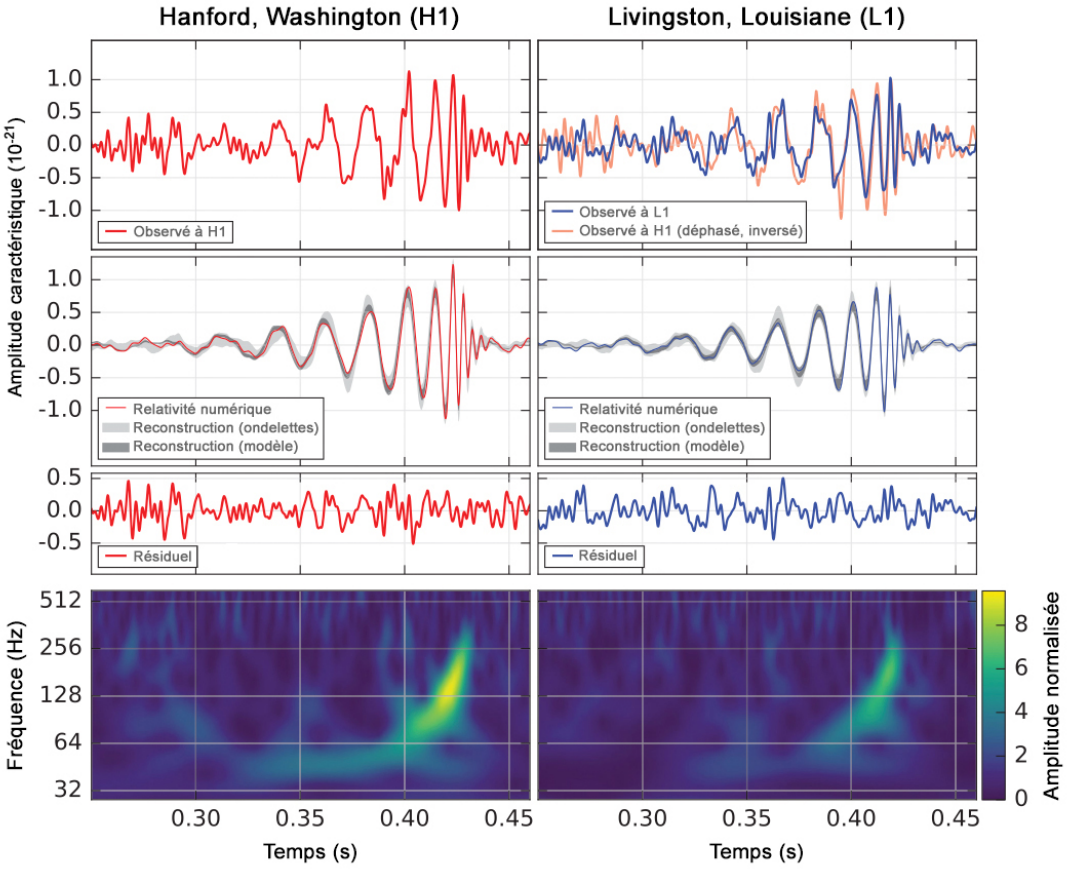

Figure 1.9: The gravitational-wave event GW150914 observed by the LIGO Hanford (H1, left column panels) and Livingston (L1, right column panels) detectors. GW150914 was generated by the inspiral and merger of two black holes of masses $m_1 = 36^{+5}_{-4}M_\odot$ and $m_2 = 29^{+4}_{-4}M_\odot$ at a luminosity distance of 410^{+160}_{-180} Mpc. The resulting Black Hole had a mass of $M = 62^{+4}_{-4}M_\odot$. The missing mass of $3^{+0.5}_{-0.5}M_\odot$ was radiated away as gravitational waves. On the top row, the strain measured by the two LIGO. On the second row, the gravitational-wave strain projected onto each detector, with solids lines showing a numerical relativity waveform from a system with parameters consistent with those recovered from GW150914. On the third row, the residuals after subtracting the filtered numerical relativity waveform from the filtered detector time series. On the bottom row a time-frequency representation of the strain data. The signal's frequency increasing over time as predicted by GR is evidenced. Picture from [18].

The O1 LIGO run ended with an other detection, GW151226 [19], and with a third possible detection, LVT151012, which was not confirmed because of it's low statistical significance

of 1.7 σ [20]. LIGO was running again in from November 30, 2016, and some time after, on August 1, 2017, VIRGO started running to [**?**], and during the joined run GW170814 was the first event detected by three interferometers [21]. Putting together the information from the three interferometers, the event's localization was much more precise, going from a 90% credible region of 1160 deg^2 using only the LIGO information to a 90% credible region of 60deg^2 using also that of VIRGO (improvement of a factor $\sim$ 20 in the precision) [21](see figure 1.10(b)).

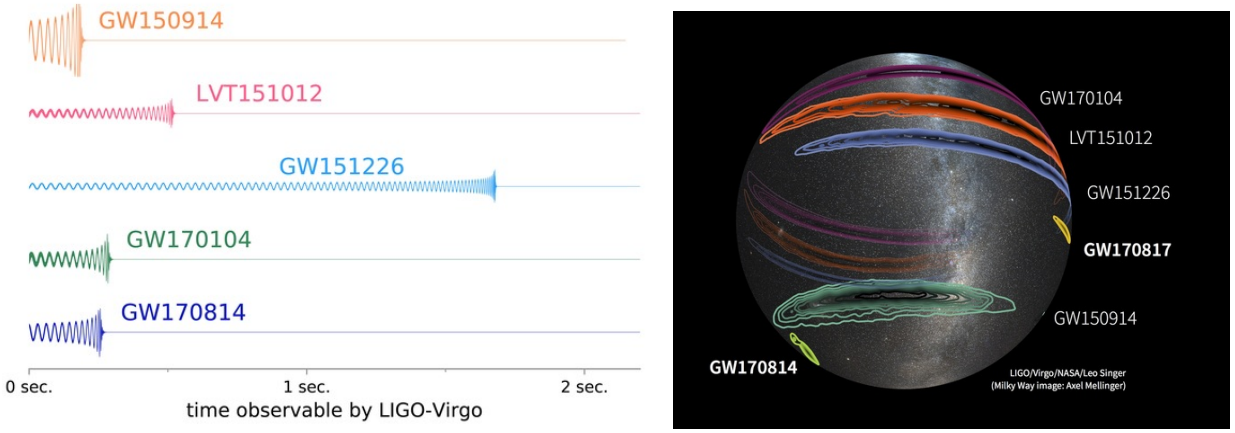

Figure 1.10: Left: the detected BH-BH waveforms. Right: the sky location of the detected events. In both pictures the event GW170608 is not reported. Pictures from [6].

Three days after GW170817 was detected by the LIGO interferometers, while VIRGO did not see it, even though his sensitivity was good enough to detect it. The source was well localized in one of VIRGO's blind spots [22]. It turned out that the signal was generated by a binary neutron star merger [22]. Since the neutron stars' masses were much smaller than those of the previously detected black holes, and hence the signal lasted much more. The source was then searched with the telescopes the and detected less than 11 hours after [23]. Having seen both electromagnetic and gravitational radiation from the same source gave officially birth to the *multimessanger astronomy*. Light from the source was observed fading in the days after [23] (see figure 1.12) .

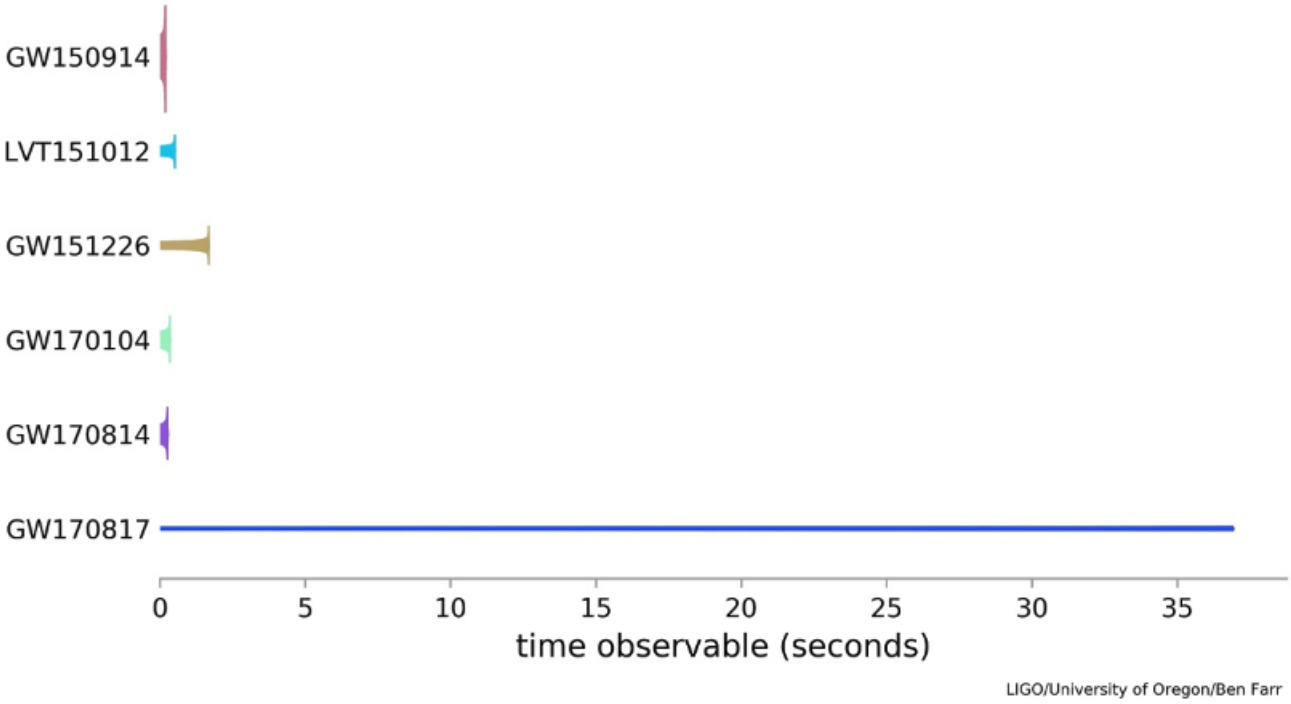

Figure 1.11: All of the detected GW signals. Since the masses were much smaller, GW170817 event's duration is much longer with respect to the binary black holes ones. Picture from [**?**]

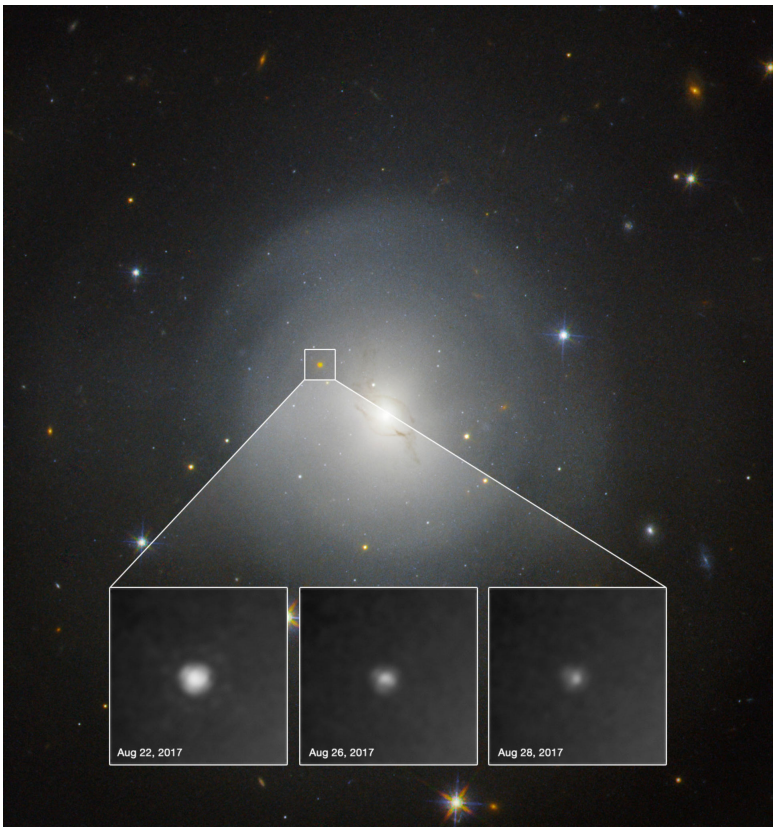

Figure 1.12: The light detected from the source of the GW170817 event in the 606nm-1.6μm wavelength band. The smaller pictures show how the emitted intensity evolved respectively 5, 9 and 11 days later. Picture from [**?**]

Chapter 2

Thermal Noise and Thermodynamic Equilibrium

2.1 Thermal Noise

Thermal noise originates one of the fundamental limits in the precision of mechanical measurements and high-sensitivity galvanometers [7]. It is caused by the thermal kinetic energy of the atoms in the detector and the most straightforward way to prevent it is cooling down the experimental apparati to cryogenic temperatures.

Thermal noise can be thought as a stochastic force F_{th} acting on each atom of the apparatus. Because it's randomness, only statistical hypothesis can be made on it, as it having a null time average $\langle F_{th}(t) \rangle = 0$. The Fluctuation Dissipation Theorem (FDT) states that thermal noise's power spectral density (PSD) (see appendix A) in a mechanical system is [12]

$$S_{F_{th}F_{th}}(\omega) = 4k_B T R(\omega) \tag{2.1}$$

where $R(\omega)$ is the mechanical resistance of the system, defined as the real part of the impedence $Z = F/\dot{x}$ [12].

For a particle subject to a velocity damping (VD), a restoring force and to thermal noise, the equation of motion is

$$m\ddot{x}(t) + f\dot{x}(t) + kx(t) = F_{th}(t) \tag{2.2}$$

where m is the mass of the particle, f is the velocity damping coefficient and k is the spring's constant [12]. The thermal noise's spectrum in case of velocity damping can be straightforward computed:

$$R(\omega)_{VD} = \Re\left[\frac{F}{\dot{x}}\right] = \Re\left[\frac{\ddot{x} + f\dot{x} + kx}{\dot{x}}\right] = \Re\left[i\omega m + f + \frac{k}{i\omega}\right] = f \tag{2.3}$$

resulting in a white noise spectrum $S_{F_{th}F_{th}}(\omega) = 4k_B T f$ [12] .

The PSD of the mass's position $S_{xx}(\omega)$ induced by thermal noise can be then computed solving equation (2.2) in the frequency domain and finding the transfer function $H(\omega)$ of thermal noise and position:

$$x(\omega) = \frac{1}{-m\omega^2 + i\omega f + k} F_{th}(\omega) = H(\omega) F_{th}(\omega) \tag{2.4}$$

Finally the PSD of the mass's position is [12]

$$S_{xx,VD}(\omega) = |H(\omega)|^2 S_{F_{th}F_{th}}(\omega) = \frac{4k_B T f}{(k - m\omega^2)^2 + (\omega f)^2} \tag{2.5}$$

In the description of a solid, which is the case of this thesis, the damping is modeled as *internal damping* (ID) [12], an extension of Hooke's law which uses a *complex spring constant* so that the restoring force is $F_s = -k(1 + i\phi(\omega))x$ [12]. The imaginary part of the spring constant causes a lag between the spring's response and the force, and a fraction $2\pi\phi(\omega)$ of the energy stored in the spring is be dissipated in each cycle [12]. The PSD of thermal noise in the case of internal damping is:

$$S_{F_{th}F_{th}\,ID}(\omega) = 4k_BTk\phi(\omega)\omega^{-1} \tag{2.6}$$

and is not white anymore. The PSD of the position of a particle subject to internal damping is [12]:

$$S_{xx,\,ID}(\omega) = |H(\omega)|^2 S_{F_{th}}(\omega) = \frac{4k_BTk\phi(\omega)}{\omega[(k - m\omega^2)^2 + (k\phi(\omega))^2]} \tag{2.7}$$

The sharpness of the resonance is determined by the quality factor Q defined as the ratio between the resonant frequency ω_0 and the full-width-at-half-maximum (FHWH). In the case of VD $Q = m\omega_0/f$ and for ID $Q = 1/\phi(\omega_0)$ [12]. For low loss systems the PSD of the position is sharply peaked around ω_0 [12]. A plot of equation the two modeled spectra is reported in figure 2.1:

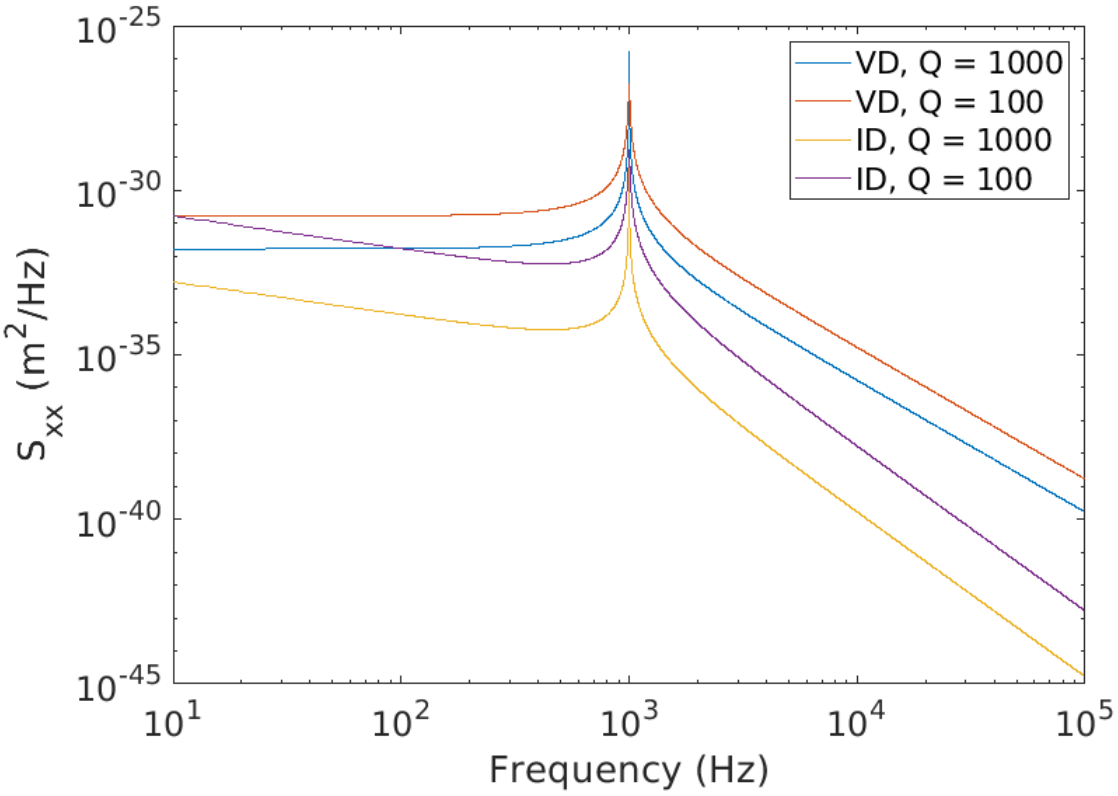

Figure 2.1: Examples of the PSD of the mass's position if subject to VD and ID with $m = 1g$, $\omega_0 = 1000Hz$, $T = 300K$ and $Q = 100$, 1000.

The integral in frequency domain of the two spectra (2.5, 2.7) gives a mean-square displacement of the mass's position [12]:

$$\langle x_{th}^2 \rangle = k_BT/k \tag{2.8}$$

consistently with the equipartition theorem, stating that each quadratic term in the energy has a mean value of $\frac{1}{2}k_BT$.

2.2 Thermal Noise in GW Interferometers

As shown in figure 1.8, GW interferometers are limited in the mid and low frequency band by thermal noise originated in the mirror coatings and in the mirror suspensions. Thermal noise's is currently modeled by means of the FDT, which sits on the hypothesis of thermodynamic equilibrium [28]. Whereas thermal noise prediction made with FDT are well verified in precision experiments, GW interferometer can not be considered equilibrium devices. This thermodynamical picture of interferometers is not fully justified, since it has been shown that non-equilibrium conditions arise [28]. A non-equilibrium modeling should be preferred, but currently there is no complete theory in statistical mechanics explaining thermal noise in solids in non equilibrium states. A first investigation has been started by the Rarenoise Experiment (see [13]), but more experimental data is needed.

Currently the detectors are being upgraded, and new experimental techniques are being added in order to achieve better sensitivity. Many proposals for the upgrades of new detectors foresee substantially higher circulating optical powers, often paired with cryogenic operation. Absorbed laser powers and thermal compensation techniques are going to add many thermal gradients and non-thermodynamical equilibrium situations. The inevitable heat flows present in these conditions make the approximation of equilibrium for thermal noise hardly applicable. It is therefore important to study how thermal noise behaves in non equilibrium conditions, and the impact this may have in particular on the performance of GW detectors.

2.3 The "Rarenoise" Experiment

The Rarenoise Experiment (see [13]) consists in the high precision measurement of the vibrations of a mechanical resonator, i.e. the low-frequency acoustic modes of vibration of a macroscopic and monolithic aluminum piece, in both thermodynamical equilibrium and non-thermodynamical equilibrium steady states (NESS). The aluminum piece is hosted in a vacuum environment and isolated from external perturbations with a cascade of mechanical filters. The dominant noise force acting on the aluminum piece is of thermal origin, at least in the frequency range where the lowest transverse and longitudinal acoustic mode resonate [13]. (see figure 2.2 (b), (c)).

The resonator is machined from a single piece of Al5056, a material with low intrinsic mechanical losses. The resonator consist in a squared cross section, $10cm$ rod kept in vertical position. The top is clamped and the bottom is loaded with a $4.35cm$ cuboid mass of about 0.25 kg, which is free to move. Dimensions are chosen after a FEM modeling, so that the first longitudinal and transverse modes resonate in a frequency range high enough so that the mechanical filter is effective but no internal resonances of its structure are present. The first transverse mode resonates at $\sim 320Hz$ and the first longitudinal mode resonates at $\sim 1420Hz$. In the first version of the experiment, which I will refer to as *Rarenoise-Capacitor*, parallel to the vertical rod, two protrusions hold a metal plate used to realize a *capacitive readout* (figure 2.3) to measure the vibrations of the resonator. The capacitor is formed by the metal plate and by the cuboid mass's surface. The plate is electrically insulated from the protrusions by a 100um thick teflon spacer.

The oscillators can be driven out of thermal equilibrium by means of a thermal source heating the cuboid mass (see figure 2.2(a)). Temperature is measured on the top of the rod (T_1) and on the cuboid mass (T_2) (see figure 2.2, 2.3) to detect the induce thermal difference ΔT.

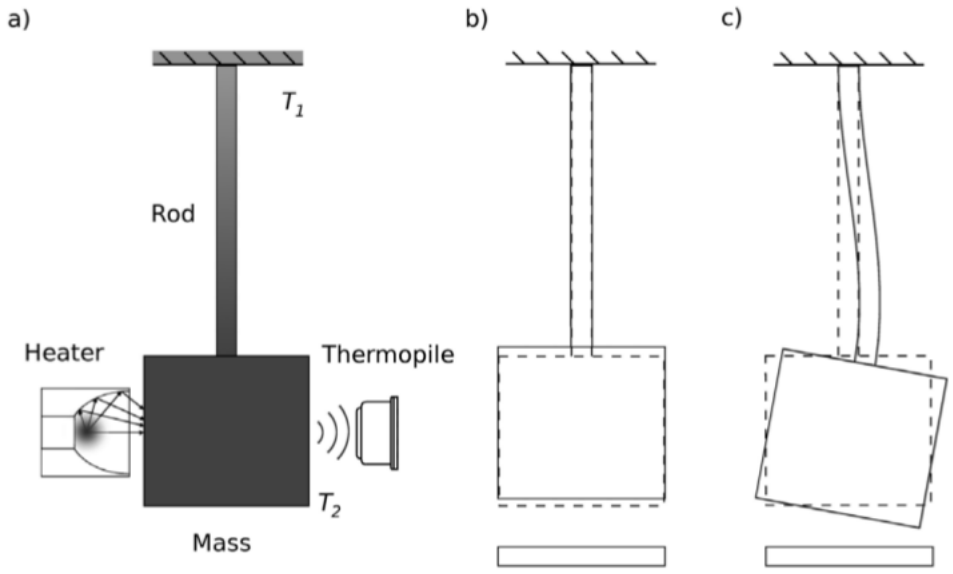

Figure 2.2: Schematic drawing of the elastic body, consisting in a rod with one extreme fixed and the other loaded by a mass free to move. (a) A NTC thermometer is used to measure the temperature T_1 on the top of the rod, while a contactless thermopile is used to read the temperature of the cuboid mass T_2. A heater heats the cuboid load mass. The rest of the experiment is at room temperature. The first longitudinal mode (b) expected around 1.4 kHz and the first transverse mode (c) around 300 Hz. In figures (b) and (c) the metal plate used for the capacitive readout is also represented. Figure from [13].

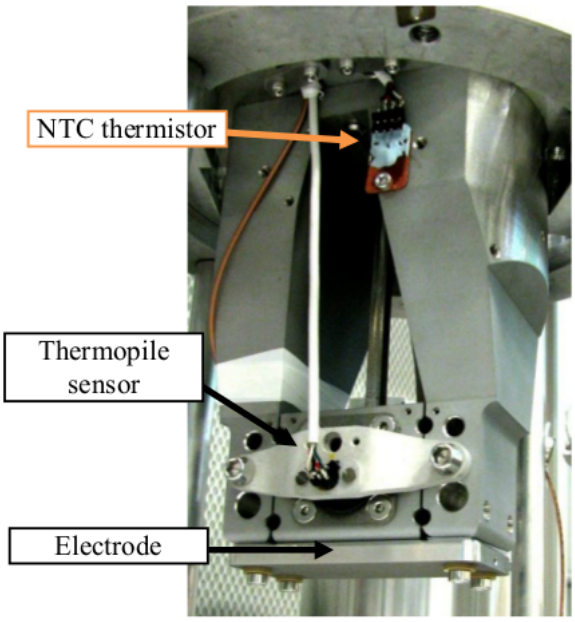

Figure 2.3: Picture of one resonator from the Rarenoise experiment. The resonator in the center, while the two side protrusions are used to hold the plate beneath the resonator, used to realize the capacitive readout. The thermopile is visible, while the heater is on the opposite side of the oscillator. Figure from [14].

The PSD (see appendix A) of the measured position was computed. In correspondence of the modes' resonances at $\sim 300Hz$ and $\sim 1400Hz$, peaks stood off on the PSD: these

peaks were then fitted around the resonance using a lorentzian curve [13]

$$y(f) = \frac{2}{\pi} A \frac{w}{4(f - f_0)^2 + w^2} + y_0 \tag{2.9}$$

where f_0 is the resonant frequency, w is the full width at half maximum (FHWH), A is the area of the Lorentzian curve and y_0 is the constant fitting the additive background noise level. Equation (2.9) is a good approximation of both equations (2.5, 2.7) near the resonance.

The area of the curve can be used as an estimate of the time averaged mean square vibration $\langle x_1(t) \rangle$ of the oscillator. At thermodynamic equilibrium with low losses and in absence of external noise, the root-mean-squared vibration induced by thermal noise is related to the thermodynamic temperature (see equation 2.8), hence an *effective temperature* T_{eff} can be estimated from the area of the peaks:

$$T_{eff} = \frac{m_1 \omega_1^2 \langle x_1(t)^2 \rangle}{k_B} \tag{2.10}$$

where m_1 is the mass of the longitudinal mode that resonates at ω_1.

The equilibrium measurements first confirmed that T_{eff} was a good extimation of the resonator's temperature.

The same kind of measurement were repeated in presence of stationary heat fluxes. This originated nonequilibrium steady states which were characterized by the temperature difference $\Delta T = T_2 - T_1$ and $T_{avg} = \frac{1}{2}(T_1 + T_2)$. As reported in figure 2.4, an increase of the PSD around the resonance was observed [13]. The results of these measurements can be comprehended better by plotting $R_{NEQ/EQ} = T_{eff}/T_{EQ}$ against the temperature difference at the rod extremes, normalized by T_{avg} (figure 2.5). T_{EQ} is the thermodynamical temperature T_{eff} measured in equilibrium condition.

The most evident feature is that $R_{NEQ/EQ} > 1$ [13]. At the maximum relative temperature difference, $R_{NEQ/EQ} > 1$ by more than 4 standard deviations. A 4% relative temperature difference is enough to increase the nonequilibrium T_{eff} by 20% for the longitudinal mode, and hence over the hottest physical temperature present in the piece. For the transverse mode this effect is even more evident: the nonequilibrium T_{eff} increases by a factor of 3-4. This means that in NESS T_{eff} is not a valid estimate of the physical temperature anymore, and that energy equipartition may be not valid in non-equilibrium conditions [13].

Parallely a numerical experiment using a 1D chain of oscillators was made. The results qualitatively match the experimental data, and are also reported in figure 2.5.

Measurements suggest that in non-equilibrium condition the energy is not anymore equiparted between the modes, and hence different modes have different temperatures. These results have been interpreted as a correlation between the modes, which are normal in equilibrium condition, but in non-equilibrium are not normal anymore.

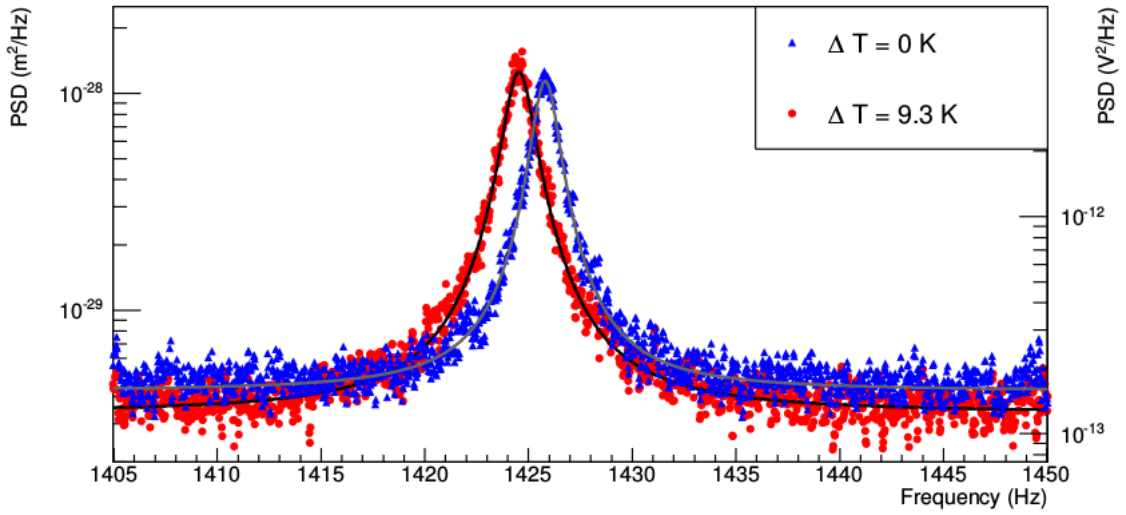

Figure 2.4: The time averaged power spectral densities (PSD) of the measured position around the first longitudinal mode in equilibrium ($T_{avg} = 288.14$ K, blue triangles) and in the non-equilibrium steady state (NESS) ($\Delta T = 9.3K, T_{avg} = 292K$, red circles). PSDs were taken with the same sensitivity of the capacitive readout (about $2 \times 10^{-6} V/m$). The gray line is the fit of the equilibrium PSD using equation (2.9) : $T_{eff} = [319 \pm 5(stat.) \pm 18(syst.)]$ K. The black line fits the NESS PSD $T_{eff} = [402 \pm 6(stat.) \pm 18(syst.)]$ K. The peak's frequency is changed due to the thermal elongation of the rod. Pictures from [13]

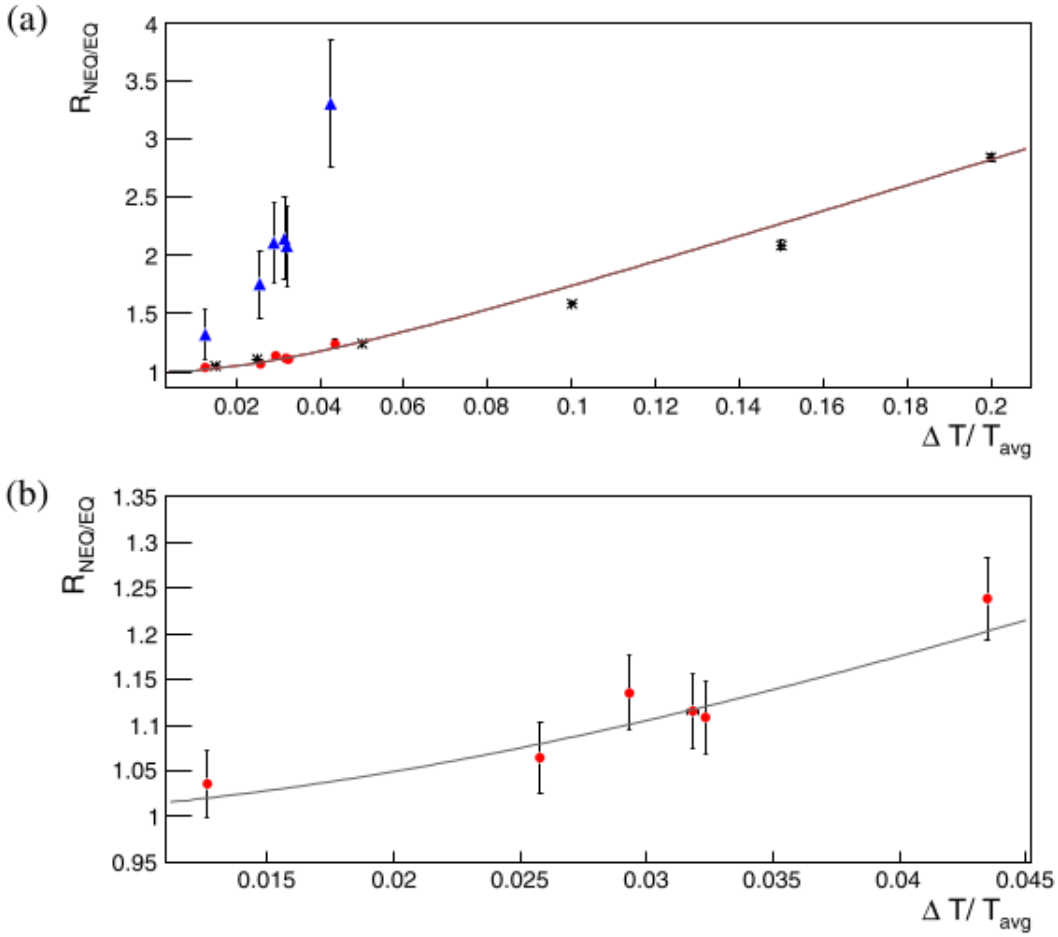

Figure 2.5: (a) Plot of $R_{NEQ/EQ}$ vs Δ_T/T_{avg} for the transverse (blue triangles) and longitudinal (red circles) acoustic modes in NESS. The error bars show the statistical uncertainty. Stars show the result of the numericical experiment with their errorbars. The gray line is the best fit of the numerical data with a theoretical model ([13], equation (11)). (b) zoom on the longitudinal mode of figure (a). Figure from [13].

Chapter 3

The Interferometric Readout

Despite being sensitive enough to detect a deviation of thermal noise from the behavior expected at equilibrium, the capacitive readout used in the Rarenoise-Capacitor experiment had a few limitations. These measurements are affected by a 5% systematical error, mainly caused by the thermal expansion of the aluminum rod and that of the cuboid mass which were changing the reference capacity. Furthermore the calibration of the sensing capacity would change during the heating transients, which made the calibration more complicated adding a bigger error in the transient's estimation.

To improve the measurements already performed by RareNoise and possibly extend them to transient states, we decided to implement an *interferometric readout* which (in principle) is self-calibrated and is able to track the mass's motion with no systematic error due to the thermal expansion of the resonator, allowing calibrated measurements during heating transients.

We observe that a standard interferometer is not suitable to follow the mass motion during thermal transients. A homodyne interferometer does not measure distance 'directly, but measures the cosine of a relative displacement ($cos(2k\Delta L)$). Information from the cosine inevitably has some 'blind spots', since where the derivative of intensity with respect to position (or to phase) vanishes, no information about the motion can be extracted. In our case, the root-mean-square (rms) of displacement due to thermal motion at the resonant modes we are interested to monitor is much smaller than the wavelength, as shown in figure 2.4. On the other hand, the aluminum thermal expansion coefficient is $\alpha_{Al} = 23 \times 10^{-6} K^{-1}$. This means, that a $\Delta T = 10K$ induced temperature difference on a $L \sim 0.1m$ long object would cause an expansion of $\Delta L = \frac{1}{2}\alpha_{Al} \cdot \Delta T \cdot L \approx 12 \times 10^{-6} m$. Thermal expansion will make the interferometer cross one of this blind spots, and during these periods measurements would have a very low accuracy.

As a solution to this problem we chose to implement a *homodyne quadrature interferometer*. Two superimposed interferometers are built exploiting two orthogonal linear polarizations of light. One interferometer's output is retarded by $\frac{\pi}{2}$ with respect to the other's one using an octal-wave plate crossed twice, so if previously we had $ITF1 \sim (1 - cos(2k\Delta L))$, now we would have also $ITF2 \sim (1 - sin(2k\Delta L)$, and combining the two informations the phase can be unambiguously extracted, being independent on fringe crossings. The needed experimental setup to achieve this is in figure 3.1.

To integrate the interferometric readout in the setup of the Rarenoise-capacitor experiment, a compact optical bench has been designed, for it to be screwed in place fo the capacitive readout plate. The interferometer's bench hosts a 50% beam splitter, a reference high reflectivity mirror (end of the first arm), octal-wave plate, and a mirror used to divert the horizontally propagating interferometer output downwards. The mass's surface the end

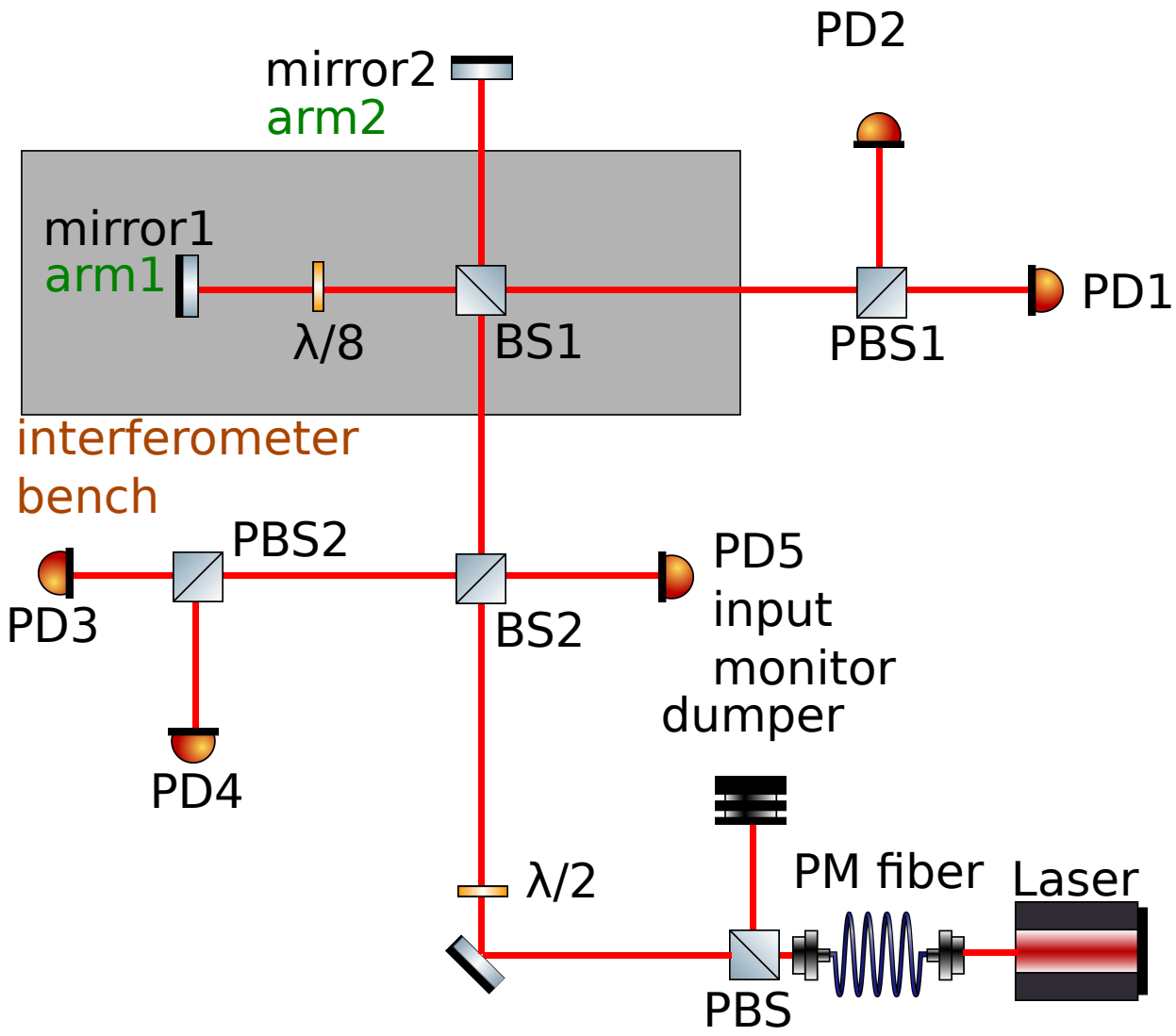

Figure 3.1: Scheme of the interferometer's setup. The laser source gives a 1064 nm wavelength beam. Using a PBS only the $\hat{p}$ polarization is selected. A half-wave plate ($\lambda/2$) turns the polarization angle of 45°. A pick off (BS2) then reflects half of the beam's intensity to an input intensity monitor photodiode (PD5). The transmitted beam heads towards the interferometer. A 50% beam splitter (BS1) splits the beam into the two arms. Mirror 1 is a fixed reference mirror, while mirror 2 is the resonator's surface, which has been mirror-polished. The octal-wave plate is placed in arm1 to add a phase delay to one polarization with respect to the other one. The beams from the two arms then recombine in BS1, and get partially transmitted or reflected. This generates two outputs. A first output from the interferometer propagates towards the right in figure and a second output propagates downwards, back to the laser source. The output going back to the laser source is not detected. The output going right is splitted in its polarization components by (PBS1). The two beams are the detected by PD1 (detecting FMP) and PD2 (detecting FMS). The elements that will be mounted on the interferometer bench are drawn inside the gray rectangle. All of the other optics except mirror 2 are going to be mounted on the optical bench.

mirror of the second arm. The whole experiment is then placed over an air suspended optical bench, where the remaining components needed for the interferometric readout are mounted.

3.1 The Intensity Signals - Ideal Case

In this section I compute the signal that can be extracted by the combination of two $\pi/2$ shifted interferometers described in section at the beginning of the chapter. For simplicity I will start with an ideal case, where all mirrors have perfect 100% reflection and all BSs split the beam's intensity perfectly in two equal parts (50-50 Beam Splitters). The conceptual design of the intereformetric readout is depicted in figure 3.1, where mirror2 represents the oscillator whose motion we want to measure. The linear p-polarization of the incoming beam is set by the polarizer (PBS) positioned after the laser source. The beam's electric field is

$$\vec{E} = \hat{p}\,\sqrt{2}E_0 e^{i(kz-\omega t)} \tag{3.1}$$

where $\hat{p}$ ($\hat{s}$) is the vector representing the p-polarization (s-polarization). The polarization angle is then turned by 45° using a half-wave plate ($\lambda/2$, figure 3.1). This is equivalent to have two superimposed beams, each of them having half of the intensity it had before, one polarized in $\hat{p}$ and the other one polarized in $\hat{s}$. Since electromagnetism is linear, the two beams act as independent. The electric field becomes

$$\vec{E} = (\hat{p}+\hat{s})E_0 e^{i(kz-\omega t)} \tag{3.2}$$

Half of the intensity is reflected by BS2 and is acquired by a photodiode (PD5, figure 3.1) as monitor of the incoming intensity to the interferometer. I then define $I_0 = |E|^2$ to be the intensity of the beam transmitted by BS2. The transmitted beam then goes towards the interferometer, is splitted by the 50% beam splitter (BS1, figure 3.1) into the two arms. In arm 2 the beam simply heads towards mirror 2 and is reflected backwards. The electric field gains a phase $2kL_2(t)$ and a factor $\frac{1}{2}$ since it passes twice through the BS1. A factor $e^{i\pi}$ is also gained by the output on the right (see figure 3.1) because of a reflection of the beam from arm 2 on a material with higher refraction index. The electric field of the beam heading back from mirror 2 in BS1 is:

$$\vec{E}_{arm2} = \frac{\hat{p}+\hat{s}}{2\sqrt{2}}E_0 e^{i(kz-\omega t)}e^{ik2L_2(t)}e^{i\pi} \tag{3.3}$$

In arm 1 the same happens for a different length L_1, but the presence of the octal-wave plate ($\lambda/8$, figure 3.1) adds to one polarization, lets say the $\hat{s}$ polarization, a $\frac{\pi}{4}$ phase with respect to the $\hat{p}$ polarization each time the beam goes through it. Since the plate is crossed twice, this effect cumulates, and the electric field in $\hat{s}$ earns a total $\frac{\pi}{2}$ delay with respect to the electric field in $\hat{p}$. The electric field of the beam reflected off of mirror 1 in BS1 is:

$$\vec{E}_{arm1} = \frac{\hat{p}}{2\sqrt{2}}E_0 e^{i(kz-\omega t)}e^{ik2L_1(t)} + \frac{\hat{s}}{2\sqrt{2}}E_0 e^{i(kz-\omega t)}e^{ik2L_1(t)+\frac{\pi}{2}} \tag{3.4}$$

The beams recombine and interfere in BS1, and there are two possible outputs: the output composed by the reflected beam from arm1 and the transmitted beam from arm2 the output composed by the transmitted beam from arm1 and the reflected beam from arm2. I will refer to these respectively as *forward output* (the one heading towards PBS1), and *return output* (the one heading back to the laser source).

The electric field in the forward output is:

$$\vec{E}_{forward} = \frac{E_0 e^{i(kz-\omega t)}}{2\sqrt{2}}\left(\hat{p}\left(e^{i(k2L_2(t)+\pi)}+e^{ik2L_1(t)}\right)+\hat{s}\left(e^{i(k2L_2(t)+\pi)}+e^{i(k2L_1(t)+\frac{\pi}{2})}\right)\right) \tag{3.5}$$

Each output contains the information about the interference of the $\hat{p}$ beam and the information about the interference of the $\hat{s}$ beam. The two polarizations in the output beam can be separated using a polarizing beam splitter (PBS1 in figure 3.1 in the *forward* output and PBS2 in figure 3.1 for the *return output*). The intensity on the $\hat{p}$ polarization for the ideal forward output (i.e. on the PBS1 transmission) which I named "Forward Michelson P" *intensity signal* (FMP) is:

$$FMP(t) = \frac{I_0}{4}(1 - cos(2k\Delta L(t)\,)) \tag{3.6}$$

with $\Delta L(t) = L_2(t) - L_1(t)$ and $I_0 = E_0^2$. This result can be compared with equation 1.16. The forward $\hat{s}$ output (the one reflected by the PBS1) "Forward Michelson S" (FMS) is

$$FMS(t) = \frac{I_0}{4}(1 - sin(2k\Delta L(t)\,)) \tag{3.7}$$

The beam the retur output follows the incoming beam's path backwards and is then half reflected by BS2. PBS2 separates the two polarizations. After the same computations (no residual $e^{i\pi}$ factors are gained this time) the ideal "Return Michelson P" (RMP) and "Return Michelson S" (RMS) *intensity signal* are

$$RMP(t) = \frac{I_0}{8}(1 + cos(2k\Delta L(t)\,)) \tag{3.8}$$

$$RMS(t) = \frac{I_0}{8}(1 + sin(2k\Delta L(t)\,)) \tag{3.9}$$

Energy must conserve: the consistency of these results can be checked by summing the intensity of the four outputs (the return outputs are considered before BS2 and have a factor 2 in front. The result is $FMP + 2RMP = I_0/2$, $FMS + 2RMS = I_0/2$ so the intensity in the two independent beams is conserved. Totally $FMP + 2RMP + FMS + 2RMS = I_0$.

An example of the four outputs (3.6, 3.7, 3.8, 3.9) is shown in figure 3.2.

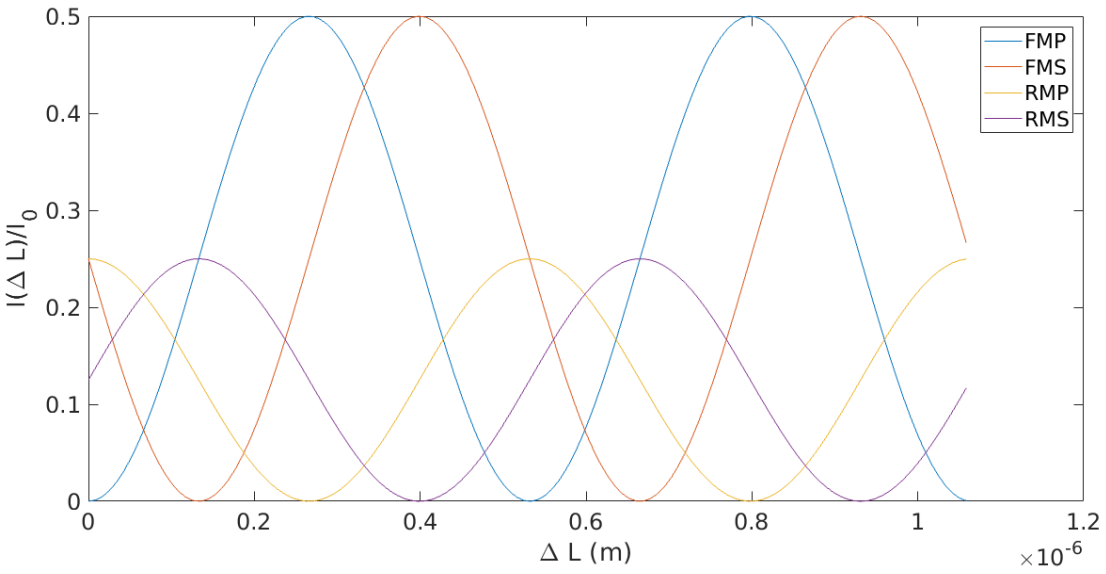

Figure 3.2: Plot of the signals of the four output photodiodes (3.6, 3.7, 3.8, 3.9) if $\Delta L(t)$ linearly varies from 0 o λ).

3.2 The Ideal Two Photodiodes Readout

In principle, all the information needed to compute $\Delta L(t)$ can be extracted from just two forward photodiodes. I will concentrate on the forward outputs.

The intensity signals (3.6, 3.7) consist of two parts: a *constant term* ($\frac{I_0}{4}$), which is just the sum of the intensities of the beams from the two arms as if they had had no interference, and the *interference term*, i.e. the modulation due to interferometry ($\frac{I_0}{4}cos(2k\Delta L)$). The information about the relative motion is encoded inside the *interference term*, which has to be isolated and extracted in order to reconstruct the relative motion of the mirrors.

Generically, the extraction of a interferometric signal from an ideal intensity signal can be done by measuring just the maximum value of the signal: for example, considering FMP: $max(FMP) = \frac{1}{2}I_0$. At this point I can compute the *normalized interference term*:

$$- cos(2k\Delta L(t)\,) = \frac{FMP(t) - \frac{1}{2}max(FMP)}{\frac{1}{2}max(FMP)} \tag{3.10}$$

and similarly extending to FMS. Note that this method requires the intensity signal to go through it's maximum at some point.

The phase $\varphi = 2k\Delta L$ is then computed as the *four quadrant arctangent* (see figure 3.3) of the two *normalized interferometric signals*: The result of this computation, unlike the usual arctangent, gives a value in the interval $[-\pi, \pi]$. I will refer to this ϕ value as *computed phase*.

$$\phi(t) = 2k\Delta L = atan2(sin(2k\Delta L(t)\,), cos(2k\Delta L(t)\,)) \tag{3.11}$$

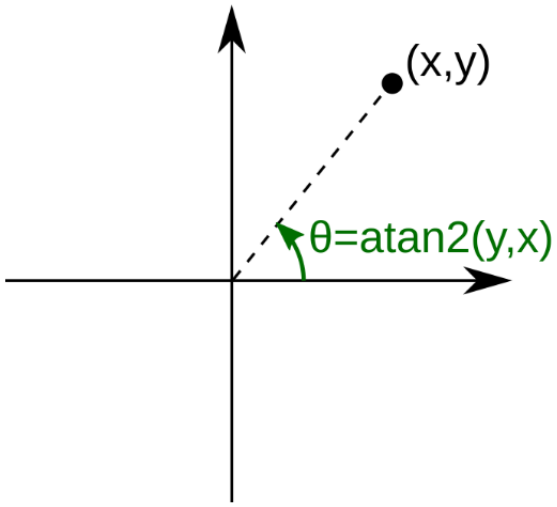

Figure 3.3: The four quadrant arctangent (*atan2(y, x)*) is an usual arctangent computation that takes advantage also of the information of the variable's signs to extend its'range from $[-\pi/2, \pi/2]$ to $[-\pi, \pi]$.

The resulting computed phase angles $\phi(t)$ lie in the $[-\pi, \pi]$ interval, and need to be *unwrapped* (see appendix B) to recover the physical meaning of a continuous motion. Finally the *unwrapped phase* $\psi(t)$ is

$$\psi(t) = unwrap(\, atan2(sin(2k\Delta L(t)\,), cos(2k\Delta L(t)\,)\,) \tag{3.12}$$

Then, since $\psi(t) = \varphi(t) = 2k\Delta L(t)$, the relative motion of the two mirrors $\Delta L(t)$ is then computed as

$$\Delta L(t) = \psi(t)\frac{\lambda}{4\pi} \tag{3.13}$$

The whole procedure can be summarized as

$$\Delta L(t) = \frac{\lambda}{4\pi} unwrap\left(atan2\left(-\frac{FMS(t) - \frac{1}{2}max(FMS)}{\frac{1}{2}max(FMS)}, -\frac{FMP(t) - \frac{1}{2}max(FMP)}{\frac{1}{2}max(FMP)} \right) \right) \tag{3.14}$$

Note that in the ideal case there is no need to monitor the input intensity to the interferometer, since it finds no use in the analysis.

3.3 The Intensity Signals - Realistic Case

Results in section 3.1 are derived assuming no losses, ideal 50% BSs and perfect beam overlap. In a realistic case though losses are present, the BSs don't transmit or reflect 50% and furthermore behave differently with the two polarizations of the beam. The beam's intensity fluctuates in time and the overlap of the beams from the two arms is not perfect and depends on time.

To account for this a series constant and time varying coefficients has to be added to the previously found relations (equations 3.6, 3.7). As previously I will treat only FMP and FMS.

Fist of all, I will define the intensity of the beam transmitted by BS2 to be I_0. A function of time $\iota(t), \langle \iota(t) \rangle = 1$ is used to represent the laser source's intensity fluctuations.

In the realistic case the polarization rotation angle is not exactly 45°, and hence an angle 2θ which ideally is equal to 45° will describe the polarization rotation. The electric field going to the interferometer is then

$$\vec{E} = \iota(t)E_0(cos(2\theta)\hat{p} + sin(2\theta)\hat{s})) \tag{3.15}$$

The 2θ polarization rotation means that in general the intensity going to the interferometer in $\hat{p}$ is not equal to that in the $\hat{s}$ polarization.

The interferometer's response has to account for the realistic values of reflectance and transmission of both mirrors and the two BSs in figure 3.1) in each polarization. BS1 and BS2 can be characterized using some transmission and reflection coefficients for each polarization: $r_{BS1,\hat{p}}, t_{BS1,\hat{p}}, r_{BS1,\hat{s}}, t_{BS1,\hat{s}}$ and $r_{BS2,\hat{p}}, t_{BS2,\hat{p}}, r_{BS2,\hat{s}}, t_{BS2,\hat{s}}$. The two mirrors at the end of the two arms can be characterized with two coefficients r_1 and r_2. Reflection and transmission coefficients are assumed to be constant in time and their value lies in the range [0, 1].

A function of time $\varepsilon(t) \in [0, 1]$ accounts for the non perfect and time varying overlap of the two beams coming from the two arms (arm1 and arm 2 in figure 3.1): $\varepsilon = 0$ means no beam overlap and hence no interference, and $\varepsilon = 1$ means complete overlap and complete interference.

By taking into account these coefficients I obtain the interferometer outputs:

$$FMP = \iota(t)^2 I_0 cos^2(2\theta)(r_{BS1,\hat{p}} t_{BS1,\hat{p}})^2 (r_1^2 + r_2^2 - \varepsilon(t)\, 2r_1 r_2 cos(2k\Delta L)) \tag{3.16}$$

$$RMP = r_{BS2,\hat{p}}^2\, \iota(t)^2 I_0 cos^2(2\theta)(r_1^2 r_{BS1,\hat{p}}^4 + r_2^2 t_{BS1,\hat{p}}^4 + \varepsilon(t)\, 2r_1 r_2 r_{BS1,\hat{p}}^2 t_{BS1,\hat{p}}^2 cos(2k\Delta L)) \tag{3.17}$$

The same holds for the s polarization, by substituting $\hat{p} \to \hat{s}$ and cos() → sin():

$$FMS = \iota(t)^2 I_0 sin^2(2\theta)(r_{BS1,\hat{s}} t_{BS1,\hat{s}})^2(r_1^2 + r_2^2 - \varepsilon(t)\, 2r_1 r_2 sin(2k\Delta L)) \tag{3.18}$$

$$RMS = r_{BS2,\hat{s}}^2\, \iota(t)^2 I_0 sin^2(2\theta)(r_1^2 r_{BS1,\hat{s}}^4 + r_2^2 t_{BS1,\hat{s}}^4 + \varepsilon(t)\, 2r_1 r_2 r_{BS1,\hat{s}}^2 t_{BS1,\hat{s}}^2 sin(2k\Delta L)) \tag{3.19}$$

An important parameter for an interferometer quality is the *visibility*, defined as

$$V = \frac{I_{max} - I_{min}}{I_{max} + I_{min}} \tag{3.20}$$

Visibility reaches its maximum when $I_{min} = 0$ resulting in $V = 1$. This was the case with no losses and perfect 50% BSs. For the forward output

$$V_{forward} = \frac{\varepsilon(t)\, 2r_1 r_2}{r_1^2 + r_2^2} \tag{3.21}$$

and has no dependence on the BS's transmission and reflectance coefficients or on the beam's intensity. It is clearly maximized if $\varepsilon(t) = 1$ and $r_1 = r_2$. For the return output

$$V_{return} = \frac{\varepsilon(t)\, 2r_1 r_2 t_{BS1}^2 r_{BS1}^2}{r_1^2 r_{BS1}^4 + r_2^2 t_{BS1}^4} \tag{3.22}$$

depends on BS1's characteristics and on the polarization. V_{return} is generally maximized if $r_1 r_{BS1}^2 = r_2 t_{BS1}^2$.

By substituting the measured reference mirror's reflectance r_1^2 reported in section E.5, r_2^2 to be the oscillator's surface's reflectance given in table E.6 and BS1's reflectance and transmission coefficients given in section E.1, the visibility values can be computed in the case of perfect beam overlap ($\varepsilon(t) = 1$). The expected visibility for FMP and FMS is very close to 1, while the visibility for the return outputs is close to 0.9.

3.4 The Realistic Two Photodiodes Readout (2PDR)

In the realistic situation, the method presented in subsection 3.2 to extract the *interferometric signal* from the two *intensity signals* (3.16, 3.18) is no longer correct.

A first naive approach would require a calibration of the interferometeric signal, since it depends on the beam overlap ε_0 and the input intensity I_0, which are now treated as constant. These two parameters can be obtained measuring the maximum and the minimum of the signal;

Hence the maximum and minimum values for FMP are:

$$max(FMP) = I_0 cos^2(2\theta)(r_{BS1,\hat{p}} t_{BS1,\hat{p}})^2(r_1^2 + r_2^2 + \varepsilon_0\, 2r_1 r_2) \tag{3.23}$$

$$min(FMP) = I_0 cos^2(2\theta)(r_{BS1,\hat{p}} t_{BS1,\hat{p}})^2(r_1^2 + r_2^2 - \varepsilon_0\, 2r_1 r_2) \tag{3.24}$$

the constant term can be computed as

$$\frac{max(FMP) + min(FMP)}{2} = I_0 cos^2(2\theta)(r_{BS1,\hat{p}} t_{BS1,\hat{p}})^2(r_1^2 + r_2^2) \tag{3.25}$$

which is independent on ε_0.

The *interferometric term* can be then isolated subtracting the constant term from the intensity signal:

$$FMP(t) - \frac{max(FMP) - min(FMP)}{2} = -I_0 cos^2(2\theta)(r_{BS1,\hat{p}} t_{BS1,\hat{p}})^2 \varepsilon(t)\, 2r_1 r_2 cos(2k\Delta L) \tag{3.26}$$

Note that no error on the constant term is induced by a wrong estimation of ε_0.

The amplitude of the interferometric signal has to be accounted for, in order to obtain the *normalized interferometric signal* (i.e. just the the sine/cosine). This again can be achieved using the maximum and minimum information:

$$\frac{|max(FMP) - min(FMP)|}{2} = I_0 cos^2(2\theta)(r_{BS1,\hat{p}} t_{BS1,\hat{p}})^2 \varepsilon_0 2 r_1 r_2 cos(2k\Delta L) \tag{3.27}$$

The final solution is:

$$-\frac{\varepsilon(t)}{\varepsilon_0} cos(2k\Delta L(t)\,) = 2\,\frac{FMP(t) - \frac{max(FMP)-min(FMP)}{2}}{|max(FMP) - min(FMP)|} \tag{3.28}$$

the same holds for FMS. Note that this time the result is not independent on ε_0.

Once the normalized interferometric signals have been obtained, the position computation can be done as previously (see subsection 3.2). Since atan2(y, x) = atan2(αy, αx) $\forall \alpha > 0$, the resulting position is independent on both the factor $\frac{1}{\varepsilon_0}$ induced by the normalization and on the time variations of the beams' overlap $\varepsilon(t)$:

$$\phi(t) = atan2\left(\frac{\varepsilon(t)}{\varepsilon_0} cos(2k\Delta L(t)\,), \frac{\varepsilon(t)}{\varepsilon_0} sin(2k\Delta L(t)\,)\right) \tag{3.29}$$

$$\Delta L(t) = \frac{\lambda}{4\pi} unwrap(\phi(t)) \tag{3.30}$$

This procedure is though limited by the fact that both the intensity I_0 and the beam overlap ε change in time. The beam overlap is expected to change at very slow frequency, while laser intensity fluctuations manifest also in the frequency bands we are interested to and need hence to be taken into account.

3.5 The Realistic Three Photodiodes Readout (3PDR)

To get rid of the intensity as calibration parameter we use the information from PD5. Photodiode PD5 measures the intensity reflected by BS2, which is:

$$I(t) = \iota(t)^2 I_{0,\,PD5} \tag{3.31}$$

where $I_{0,\,PD5}$ is the mean value of the intensity of the beam impinging on PD5.

Signals FMP (equation 3.16) and FMS (equation 3.18) can be divided by $I(t)$, obtaining

$$\frac{FMP(t)}{I(t)} = \frac{I_0}{I_{0,\,PD5}} cos^2(2\theta)(r_{BS1,\hat{p}} t_{BS1,\hat{p}})^2 (r_1^2 + r_2^2 - \varepsilon(t)\, 2 r_1 r_2 cos(2k\Delta L)) \tag{3.32}$$

$$\frac{FMS(t)}{I(t)} = \frac{I_0}{I_{0,\,PD5}} sin^2(2\theta)(r_{BS1,\hat{p}} t_{BS1,\hat{p}})^2 (r_1^2 + r_2^2 - \varepsilon(t)\, 2 r_1 r_2 sin(2k\Delta L)) \tag{3.33}$$

This way the intensity fluctuations $\iota(t)$ are eliminated, and the signals are divided by the same factor $I_{0,\,PD5}$. The two signals (3.32, 3.33) can undergo the same 2PDR analysis, where only the visibility needs to be calibrated. The final result is independent on both visibility and laser intensity.

3.6 The Four Photodiodes Phase Readout (4PDR)

Another method to be independent on the intensity fluctuations is to make use of all four outputs (3.16, 3.18, 3.17, 3.19). The two $\hat{p}$ outputs and the two $\hat{s}$ outputs can be combined together to obtain:

$$\begin{aligned}
\Sigma_{\hat{p}} &= FMP + r_{BS2,\hat{p}}^{-2} RMP \\
&= \iota(t) I_0 cos(2\theta)^2 (r_1^2 r_{BS1,\hat{p}}^2 + r_2^2 t_{BS1,\hat{p}}^2)(r_{BS1,\hat{p}}^2 + t_{BS1,\hat{p}}^2) \\
&= \iota(t) I_0 cos(2\theta)^2 \, \Sigma_{ITF,\hat{p}} \, \Sigma_{BS1,\hat{p}} \qquad (3.34) \\
\Delta_{\hat{p}} &= FMP - r_{BS2,\hat{p}}^{-2} RMP \\
&= \iota(t) I_0 cos(2\theta)^2 (r_1^2 r_{BS1,\hat{p}}^2 - r_2^2 t_{BS1,\hat{p}}^2)(r_{BS1,\hat{p}}^2 - t_{BS1,\hat{p}}^2) - 4 r_1 r_2 r_{BS1,\hat{p}}^2 t_{BS1,\hat{p}}^2 cos(2k\Delta L) \\
&= \iota(t) I_0 cos(2\theta)^2 \, (\Delta_{ITF,\hat{p}} \, \Delta_{BS1,\hat{p}} - \varepsilon(t) A_{\hat{p}} cos(2k\Delta L)) \qquad (3.35)
\end{aligned}$$

Where I defined some auxiliary terms whose value can be computed from the characterization of the mirrors and of BS1 reported in chapter E.

$$\begin{aligned}
\Sigma_{ITF,\hat{p}} &= r_1^2 r_{BS1,\hat{p}}^2 + r_2^2 t_{BS1,\hat{p}}^2 && = 0.935 \pm 0.002 && (3.36) \\
\Sigma_{BS1,\hat{p}} &= r_{BS1,\hat{p}}^2 + t_{BS1,\hat{p}}^2 && = 0.976 \pm 0.003 && (3.37) \\
\Delta_{ITF,\hat{p}} &= r_1^2 r_{BS1,\hat{p}}^2 - r_2^2 t_{BS1,\hat{p}}^2 && = 0.014 \pm 0.002 && (3.38) \\
\Delta_{BS1,\hat{p}} &= r_{BS1,\hat{p}}^2 - t_{BS1,\hat{p}}^2 && = -0.025 \pm 0.003 && (3.39) \\
A_{\hat{p}} &= 4 r_1 r_2 r_{BS1,\hat{p}}^2 t_{BS1,\hat{p}}^2 && = 0.912 \pm 0.002 && (3.40)
\end{aligned}$$

The same happens for the $\hat{s}$ polarization:

$$\begin{aligned}
\Sigma_{\hat{s}} &= \iota(t) I_0 sin(2\theta)^2 \, \Sigma_{ITF,\hat{s}} \, \Sigma_{BS1,\hat{s}} && (3.41) \\
\Delta_{\hat{s}} &= \iota(t) I_0 sin(2\theta)^2 \, (\Delta_{ITF,\hat{s}} \, \Delta_{BS1,\hat{s}} - \varepsilon(t) A_{\hat{s}} cos(2k\Delta L)) && (3.42)
\end{aligned}$$

with

$$\begin{aligned}
\Sigma_{ITF,\hat{s}} &= r_1^2 r_{BS1,\hat{s}}^2 + r_2^2 t_{BS1,\hat{s}}^2 && = 0.926 \pm 0.001 && (3.43) \\
\Sigma_{BS1,\hat{s}} &= r_{BS1,\hat{s}}^2 + t_{BS1,\hat{s}}^2 && = 0.970 \pm 0.007 && (3.44) \\
\Delta_{ITF,\hat{s}} &= r_1^2 r_{BS1,\hat{s}}^2 - r_2^2 t_{BS1,\hat{s}}^2 && = -0.062 \pm 0.001 && (3.45) \\
\Delta_{BS1,\hat{s}} &= r_{BS1,\hat{s}}^2 - t_{BS1,\hat{p}}^2 && = -0.104 \pm 0.007 && (3.46) \\
A_{\hat{s}} &= 4 r_1 r_2 r_{BS1,\hat{s}}^2 t_{BS1,\hat{s}}^2 && = 0.891 \pm 0.04 && (3.47)
\end{aligned}$$

The ratio of Δ and Σ differs from the normalized interference term due to some coefficients which can be computed from the characterization of BS1 and of the mirrors. Δ and Σ do not depend on the intensity:

$$\begin{aligned}
\frac{\Delta_{\hat{p}}}{\Sigma_{\hat{p}}} &= \frac{\iota(t) I_0 cos(2\theta)^2 \, (\Delta_{ITF,\hat{p}} \, \Delta_{BS1,\hat{p}} - \varepsilon(t) A_{\hat{p}} cos(2k\Delta L))}{\iota(t) I_0 cos(2\theta)^2 \, \Sigma_{ITF,\hat{p}} \, \Sigma_{BS1,\hat{p}}} \\
&= \frac{\Delta_{ITF,\hat{p}} \, \Delta_{BS1,\hat{p}} - \varepsilon(t) A_{\hat{p}} cos(2k\Delta L)}{\Sigma_{ITF,\hat{p}} \, \Sigma_{BS1,\hat{p}}} \qquad (3.48) \\
&= -0.00038 - 0.999 \varepsilon(t) cos(2k\Delta L)
\end{aligned}$$

$$\begin{aligned}\frac{\Delta_{\hat{s}}}{\Sigma_{\hat{s}}} &= \frac{\iota(t)I_0 sin(2\theta)^2\left(\Delta_{ITF,\hat{s}}\,\Delta_{BS1,\hat{s}} - \varepsilon(t)A_{\hat{s}} sin(2k\Delta L)\right)}{\iota(t)I_0 sin(2\theta)^2\,\Sigma_{ITF,\hat{s}}\,\Sigma_{BS1,\hat{s}}} \\ &= \frac{\Delta_{ITF,\hat{s}}\,\Delta_{BS1,\hat{s}} - \varepsilon(t)A_{\hat{s}} sin(2k\Delta L)}{\Sigma_{ITF,\hat{s}}\,\Sigma_{BS1,\hat{s}}} \\ &= 0.0072 - 0.992\varepsilon(t) sin(2k\Delta L)\end{aligned} \tag{3.49}$$

Hence we arrive at:

$$\varepsilon(t)cos(2k\Delta L) = \frac{1}{0.999}\left(\frac{\Delta_{\hat{p}}}{\Sigma_{\hat{p}}} + 0.00038\right) \tag{3.50}$$

$$\varepsilon(t)sin(2k\Delta L) = \frac{1}{0.992}\left(\frac{\Delta_{\hat{s}}}{\Sigma_{\hat{s}}} - 0.0072\right) \tag{3.51}$$

The atan2 procedure from here on is the same as in the 2PDR, and makes the final result independent on the beam overlap $\varepsilon(t)$. In this procedure is self-calibrated, and hence does not need the signals to cross a maximum and a minimum. Note that in equations (3.34, 3.35, 3.41, 3.42) $r^{-2}_{BS2,\hat{p}}$ is indicated as the ideal summation coefficient, but in the analysis the coefficient needs to be estimated from the data since it depends on the reflectivity of the optics along the beams'path from BS1 to the photodiodes.

Finally, one could think about a five photodiode readout using the four outputs and the input intensity monitor. Unfortunately the hardware we can use for the digital acquisition of the data is limited to up to 4 channels. Thus we did not investigate further this possibility as we would be not able to implement it.

Chapter 4

Interferometer's Testing

4.1 Laser Beam

Our laser beam is a 1064 nm wavelength laser coming from a Mephisto M500NE laser source fixed on a optical bench which will from now on refer to as 'squeezer bench'. Since there was not enough space on the squeezer bench for our experiment, we routed a pickoff of the laser beam to a different table (from now on named 'Rarenoise bench') using a polarization maintaining optical fiber(PM fiber).

The setup on the squeezer bench before the pick-off for the Rarenoise experiment is reported in figure 4.1. The laser beam is reflected twice, corrected in ellipticity using a quarter-wave plate and in polarization direction using a half-wave plate[1]. The Faraday isolator blocks back reflections from reaching the laser source. We realized a pick-off using a half-wave plate and a polarizing beam splitter (PBS). By turning the half-wave plate we can choose how much power we are sending to the interferometer. We then coupled the reflected beam with the PM fiber's input collimator.

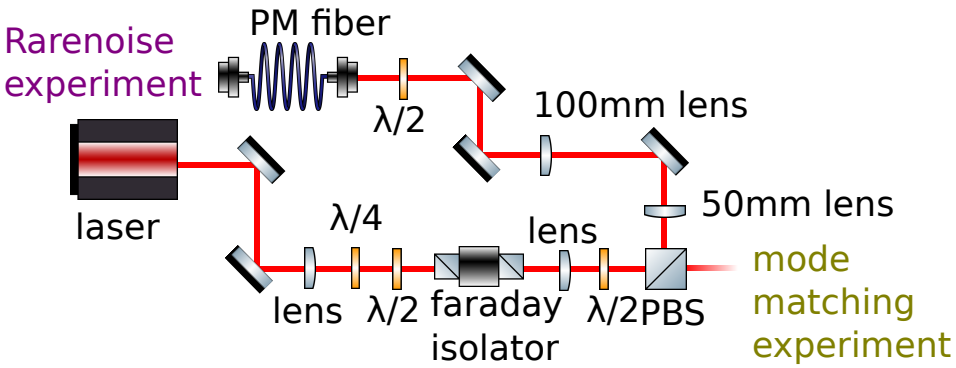

Figure 4.1: The squeezer bench's setup before the pick off going to the Rarenoise experiment.

Theory about Gaussian beams is reported in appendix C. In order to optimize the mode matching between the collimator and the laser beam, we profiled the beam coming from the PBS and the beam coming out from the input collimator of the fiber. The second step was achieved by coupling the laser beam with the output collimator, and profiling the beam coming out from the input collimator. We then realized an optical telescope to bring the beam from the PBS to have a profile close to that of the beam exiting from the input collimator. The beam profiling measurements are reported in figure 4.2:

[1]For the wave plates effect on a beam, see appendix D.

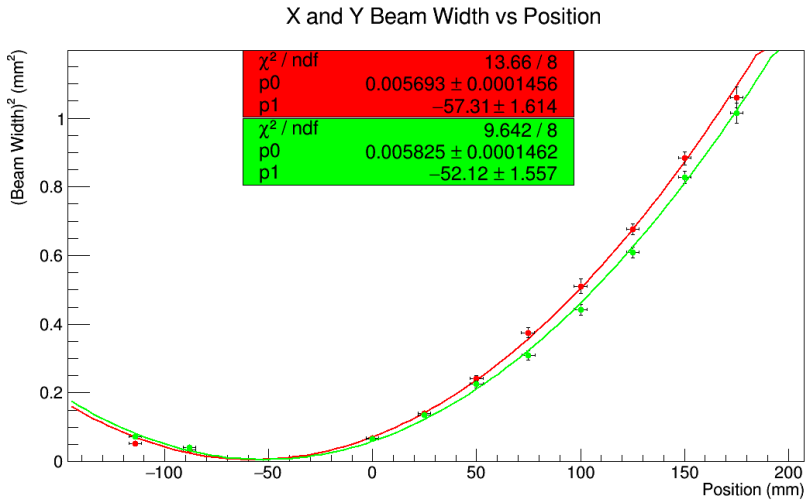

(a) Profile of the beam coming out from the PBS. The 0 position value is defined 2.5 cm further of the PBS with respect to the beam's path. The beam waist is $w_0 = (75.68 \pm 0.26)\mu m$. The waist's position is inside the PBS.

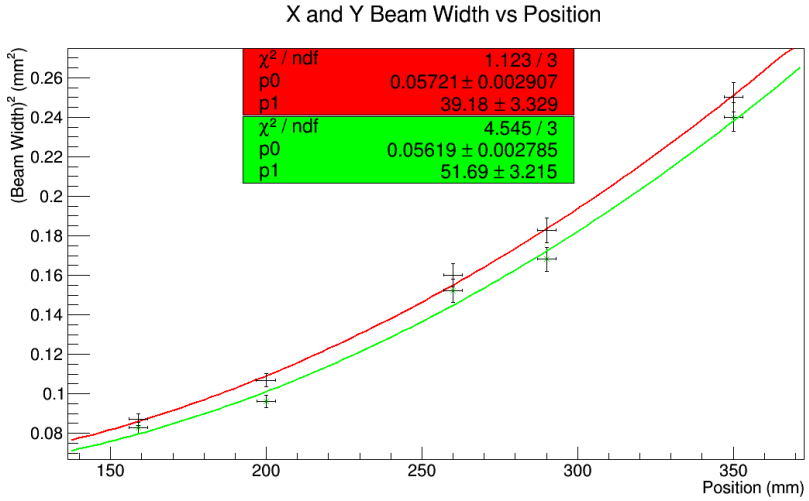

(b) Profile of the beam coming out from the input collimator. The 0 position is set at the collimator's entrance. The beam waist is $w_1 = (239.4 \pm 2.2)\mu m$ and the waist position is 4.5 cm before the collimator with respect to the outgoing beam's path.

Figure 4.2: Profile of the beam reflected by the PBS (above) and of the beam exiting from the input collimator (below). The red measurements refer to the horizontal beam's profile (x-profile), while the green values refer to the vertical profile (y-profile). The measurements obtained with the beam profiler were fitted with equation (C.8) adding a fit parameter for the waist's position: $y = p0 + \frac{(x-p1)^2}{p0(\lambda/\pi)^2}$ where p0 is the parameter indicating the square of beam's waist and p1 is the parameter indicating the waist's position. Both beams have low ellipticity.

The measured beam's waist is $w_0 = (75.68 \pm 0.26)\mu m$ situated 2 cm before the PBS, while the beam from the input collimator has a $(239.4 \pm 2.2)\mu m$ waist placed 4.5 cm before the collimator. Using the optics simulation program *JamMt* [30] we designed an optical telescope using a 50mm lens and a 100 mm lens in order to obtain a beam having a waist of $\sim 240\mu m$ without needing more than $50cm$ of beam propagation path(see figure 4.3(a)).

I then realized the telescope shown in figure 4.3(b):

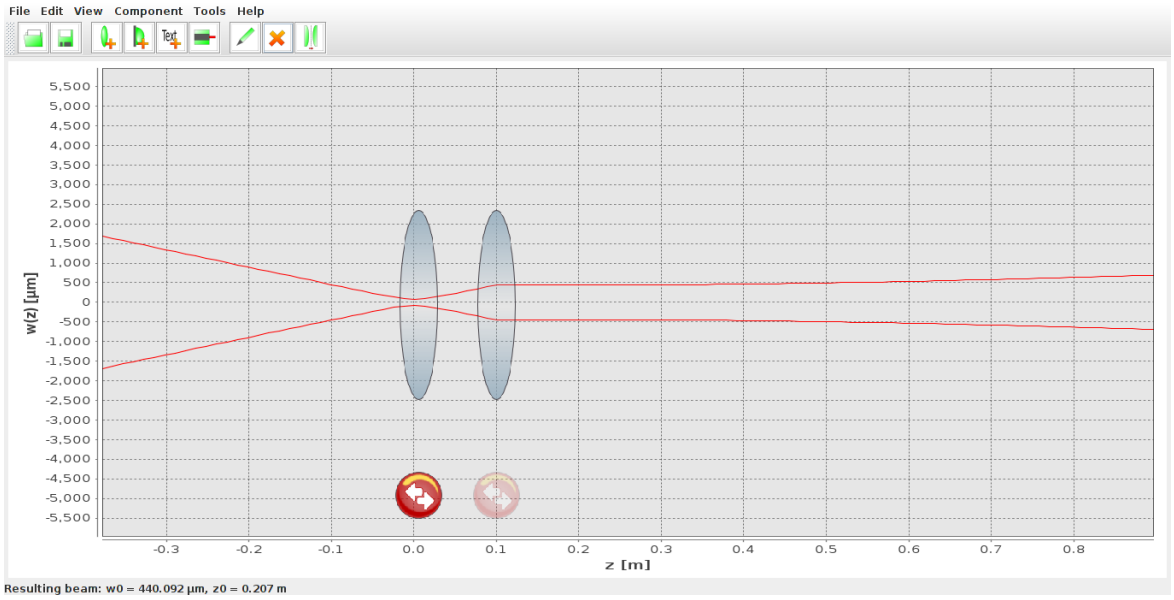

(a) The simulation of the optical telescope with the measured incoming beam realized using JamMt [30]. The number below is the beam's diameter, resulting to be 440μm situated 20cm away from the initial beam's waist position.

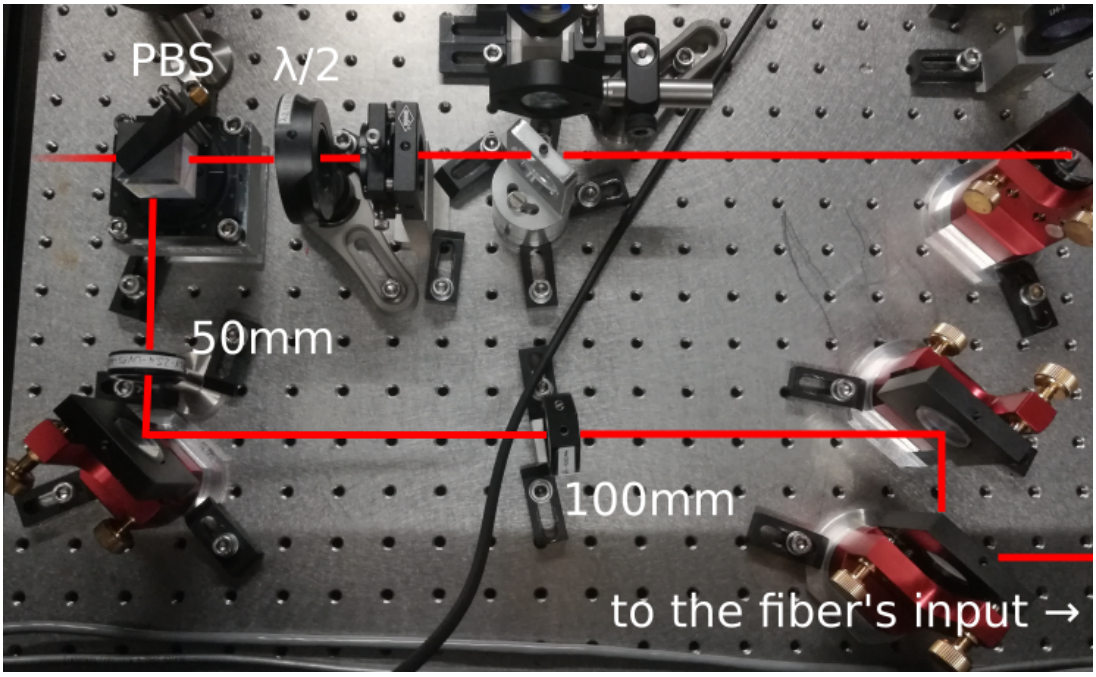

(b) Picture of the optical telescope realized to couple the laser beam reflected from the PBS with the collimator of the PM optical fiber. In this figure part of the setup in figure 4.1 is visible.

This is the resulting beam profile is reported in figure 4.3):

With careful positioning and alignment of the fiber coupler, we achieved a ∼75% coupling between the beam and the fiber [2].

The fiber's coupling is expected to change slowly in time. The PM fiber then gives in output a linearly polarized beam if the input beam is also linearly polarized, but the

[2] i.e. the beam coming out of the fiber has ∼75% of the intensity of the beam sent to the fiber's input

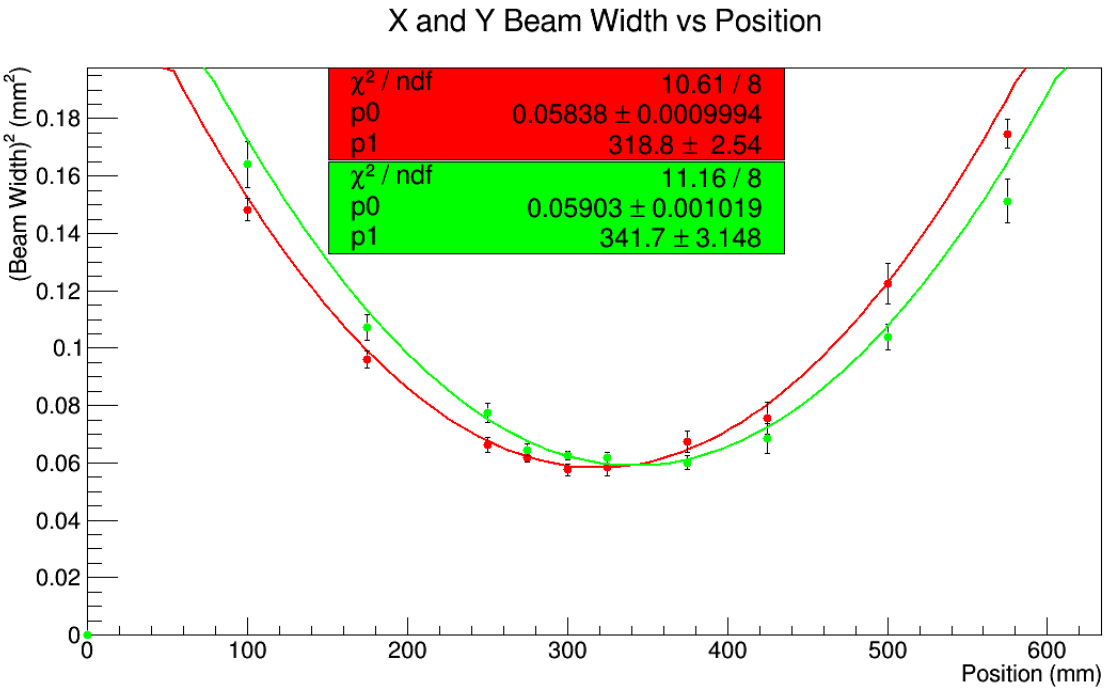

Figure 4.3: The resulting beam profile after the telescope. The fit was performed using equation (C.8). The measured waist is of $(242.28 \pm 0.14)\mu m$ placed 32 cm after the PBS.

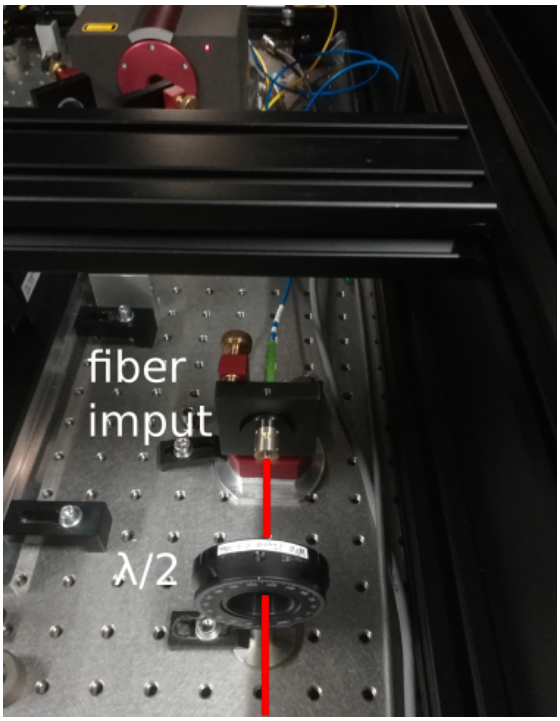

Figure 4.4: The fiber's input collimator, with the half-wave plate in front of it. The fiber's collimator has been mounted on a mirror mounting to ease the coupling with the beam. On the top right of the picture the laser source is visible.

input beam must also be aligned to one of the fiber's preferential axis. In this condition the coupling of ambient noise with the fiber's output is minimum. If the preferential axis is missed, the output beam's polarization is not linear, and the ambient noise couples more

strongly to the output beam.

We found out that placing a PBS after the fiber's output the transmitted beam intensity was noisier than the fiber's output itself, suggesting that the major noise coupling was with the output beam's polarization angle. We used this effect to match the input beam's polarization alignment. We disturbed the fiber with a monochromatic noise at a frequency $\nu_0 = 1350Hz$ (a sound wave generated with a phone app placing the phone next to the fiber), and looked at the real time PSD of the intensity of the beam transmitted by the PBS, where a peak appeared at frequency ν_0. We added a half-wave plate (see figure 4.1 and 4.4) before the fiber collimator in order be able to turn the polarization angle. The half-wave plate angle was finally set where the peak's height was minimized.

The beam from the fiber's output then needs to match the interferometer's requirements. The beam must be collimated, since we need it's amplitude not to diverge during an at least $1 \sim m$ long path, and we want the beam's width to be $\sim 1mm$ when it is reflected on the interferometer's mirrors, in order average the small local fluctuations of the cuboid mass's surface and average them out, and thus increasing the sensitivity to global motion of the cuboid mass. We profiled the beam from the output collimator. The measurements are reported in figure 4.5, and the beam diverges after $30cm$.

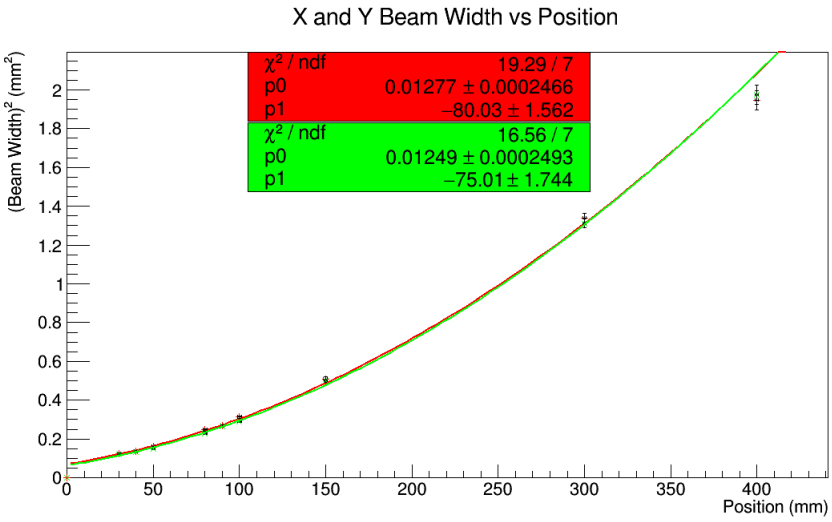

Figure 4.5: The beam from the output collimator. The measurements were fitted using equation (C.8).

We realized a second telescope after the polarizer. We designed the telescope using a 300 mm lens and a 500 mm lens in order to obtain, starting from the profile in figure 4.5, a beam with waist $w_3 = (640.6 \pm 1.6)\mu m$ situated 70 cm away from the output collimator's position. We finally profiled the beam after the telescope. A picture of the telescope is reported in figure 4.6(a) and he beam's profile is reported in figure 4.6(b).

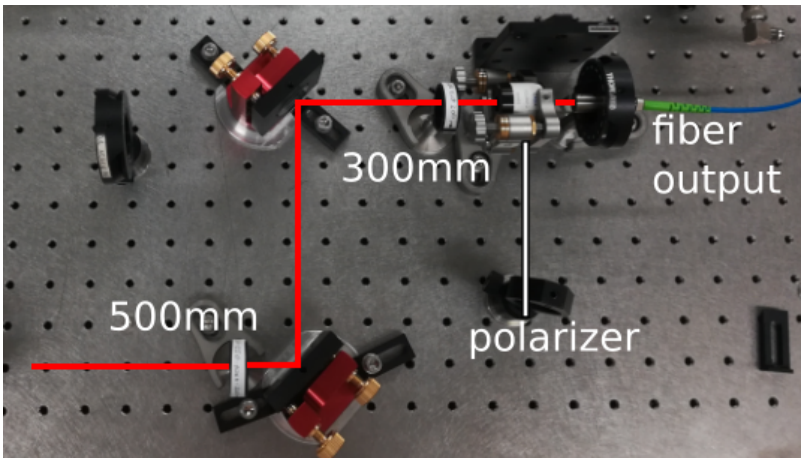

(a) Picture of the final telescope on the Rarenoise bench, with the polarizer placed right after the fiber's output collimator.

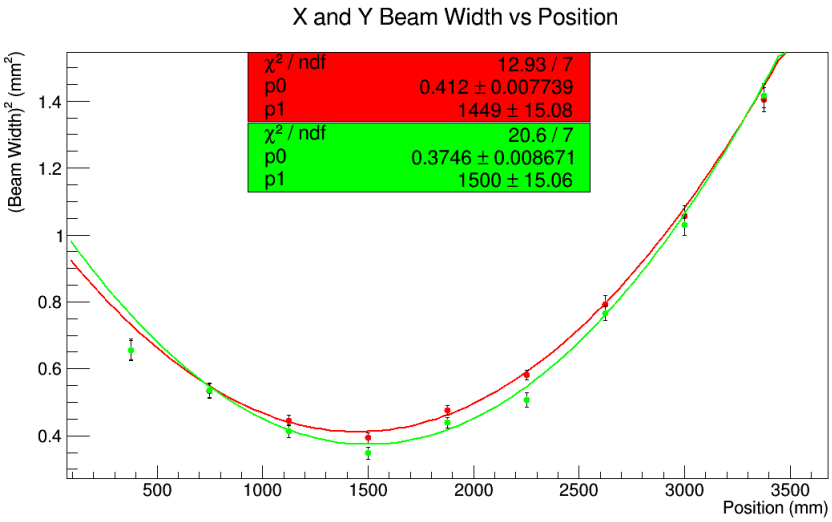

(b) Fit of the final beam's profile. The resulting waist is $w_4 = (628.5 \pm 4.5)\mu m$ situated in the desired position.

4.2 Interferometer Bench

The interferometer bench designed in chapter 3 consists in a compact $119.5mm \times 65mm$ aluminum plate, where the optics are screwed. The center hosts a 50% BS (see figure) and on the left a support for the reference mirror and a rotator for the octal-wave plate are mounted. On the right a 45° mirror is mounted in order to reflect the output beam downwards. A second plate (the blue plate in figure 4.6) is screwed into the bench and will be then screwed into the two protrusions in place of the fixed electrode of the capacitor. The bench was designed so that when coupled with the oscillator $L_1 - L_2 \lesssim 1mm$.

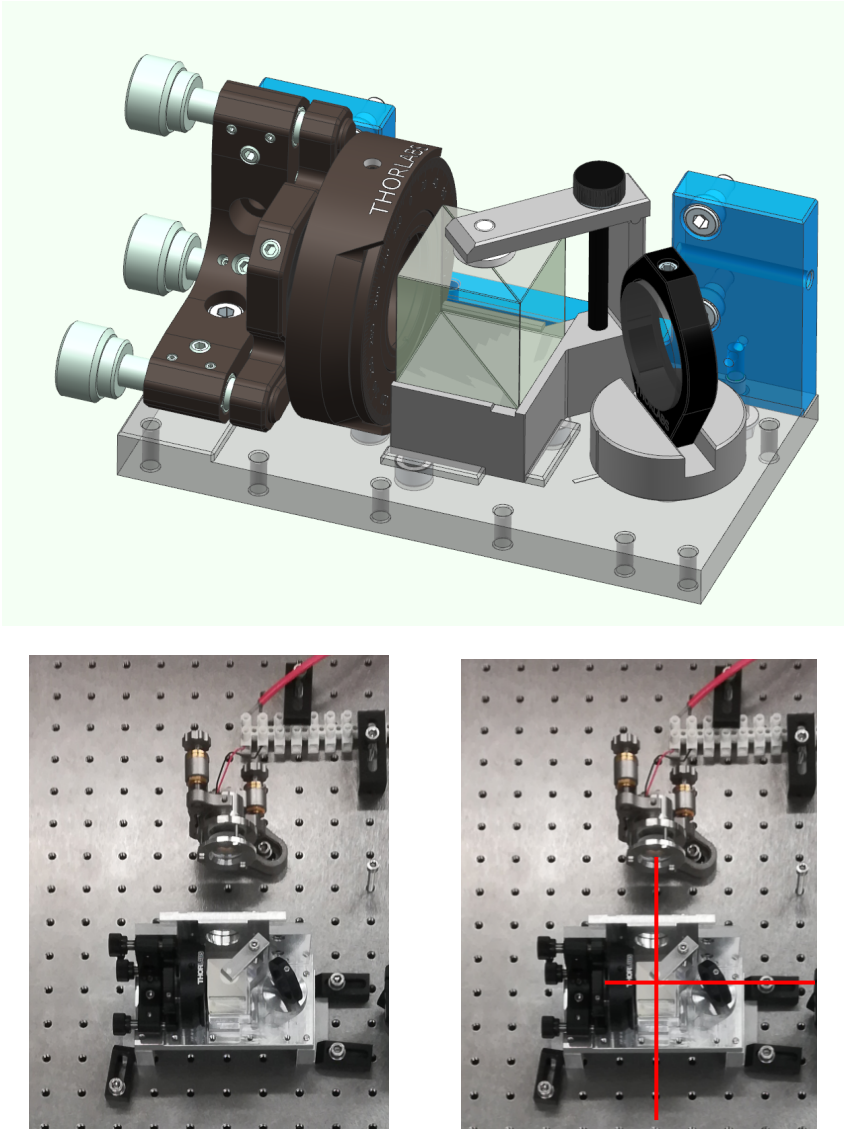

Figure 4.6: Above: Design of the interferometer's bench. The 45° mirror on the right has not been used during testing. Below, left: Picture of the interferometer's bench mounted on the optical table during the testing described in section 4.3. Two supports have been added under the bench to keep it at the right height. Above in the picture the externally mounted mirror2 is visible. Below, right: Same picture, with the beam's path evidenced: the beam comes in from below, and the forward output is being transmitted towards the right. The return output has not been acquired.

4.3 Bench Test of the Interferometer

To test the interferometric readout, we placed the interferometer bench (figure 4.6) horizontaly on the optical table and used it with a mirror mounted on a piezoelectric crystal as mirror 2. The outputs FMP and FMS were acquired using the old photodiodes reported in appendix E. We used a 2PDR analysis (see section 3.4). The intensity of the laser beam sent to the interferometer was $8mW$.

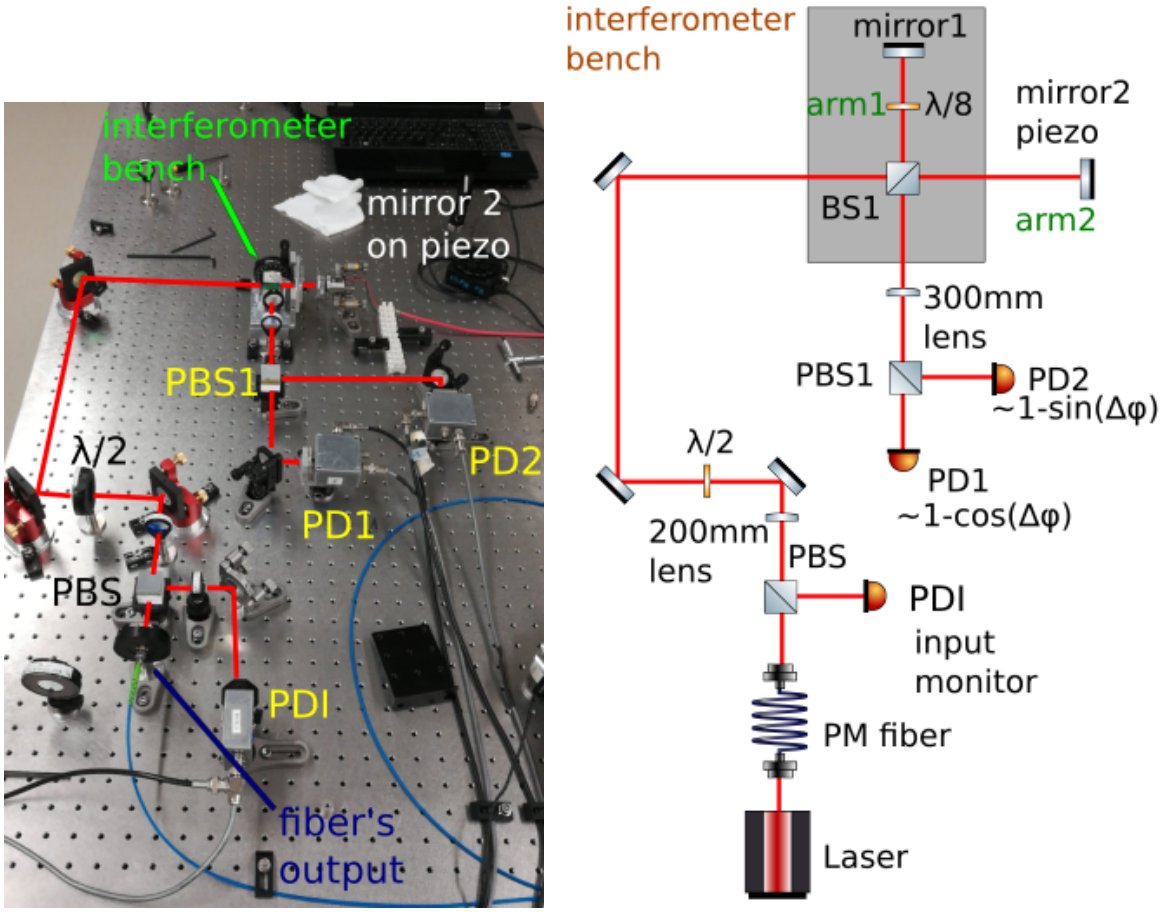

(a) (b)

Figure 4.7: The optical setup on the table used to test the interferometer. The beam from the fiber output is polarized by the polarizing beam splitter PBS. The transmitted beam heads towards the interferometer. The polarization is rotated 45° by the half-wave plate $\lambda/2$. The beam then goes to the interferometer's bench. Mirror 2 has been mounted on a piezo crystal which we send the ramp signal in figure 4.8 to. PD1, PD2 and PDI were respectively PDZ, PDB and PDTR3, whose calibration is reported in appendix E.

The piezoelectric crystal is a P-016.00H manufactured by Physik Instrumente and with a nominal deformation coefficient of $k = \frac{5\mu m}{1000V}$. The piezo was driven with a positive $700V$ peak to peak ramp signal at a frequency of 0.005 Hz which I will refer to as $V(t)$ (see figure 4.8). The total expected displacement of the mirror is $\Delta x = k \cdot 700V = 3438nm$, bringing to a total of 6 or 7 crossed fringes should be in general visible, depending on the starting position.

The photodiode's signal was then acquired at low frequency (1 Hz) for a 11 minute run. Figure 4.9shows the calibrated intensity signals of PD1 and PD2:

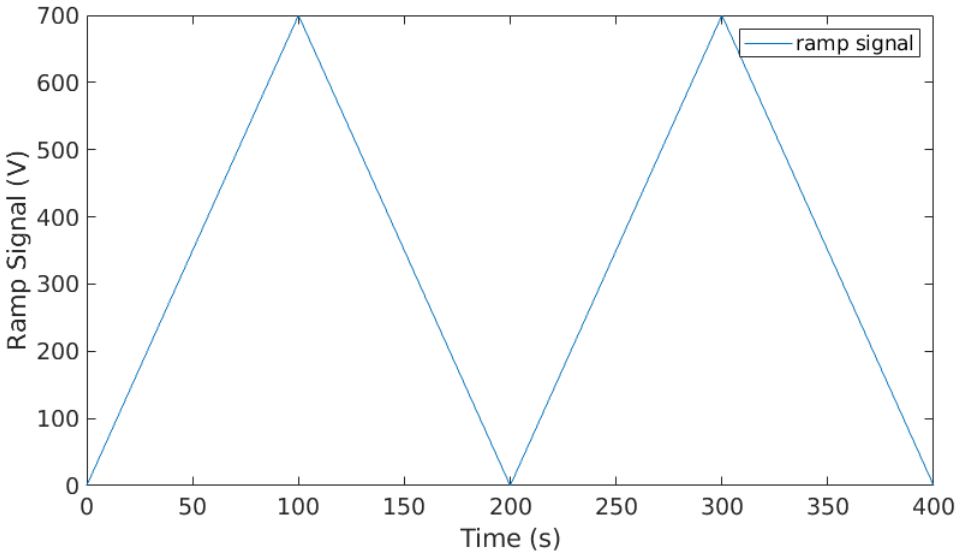

Figure 4.8: The 700 V_{pp} 0.005 Hz positive ramp signal which was driving the piezo crystal.

Two main features stand out. The second picture 4.9(b) is a 40 seconds long zoom on the intensity signals, where a low frequency modulation of the intensity stands out. The signal in the first picture 4.9(a) then appears to be dominated by an other lower frequency variation, which is the beam overlap $\varepsilon(t)$, which varies because mirror2 is being moved by the piezo. $\varepsilon(t)$ appears to be maximum at the mirror's starting position (where the alignment was optimized), ad minimum at it's maximum displacement. Note that when the mirror goes back to it's starting position, the initial overlap is recovered.

The visibility of the two interferometers (equation 3.20) is 77.3% for FMP and 78.6% for FMS at the maximum beam overlap point and 50.2% for FMP and 54.5% for FMS in the minimum beam overlap point. The visibility is assumed to be the same in $\hat{p}$ and $\hat{s}$: the low sampling frequency is probably not resolving the maxim of the intensity signals.

In the following we detail the steps and intermediate results of the 2PDR analysis described in section 3.4.

The normalized interferometric signals extraction is the achieved using equation (3.28), which subtracts from the intensity signal the constant term and divides the interferometric signal by it's amplitude. As said, this formula only works if the intensity signal goes through the maximum and the minimum, which is the case in the analyzed run. The result of this procedure is shown in figure 4.10:

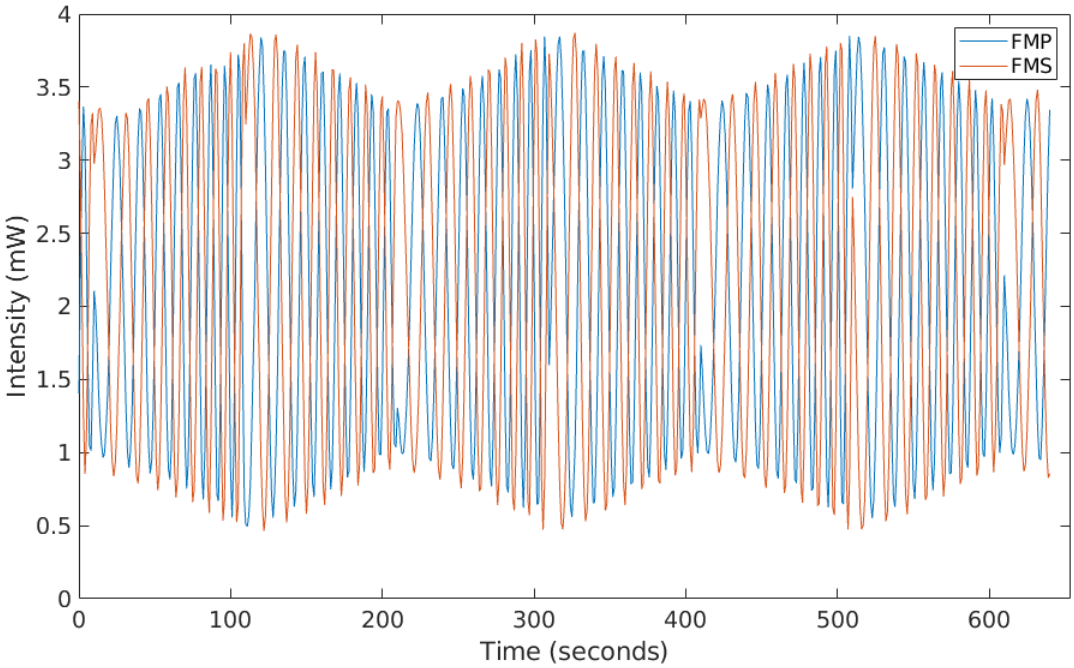

(a) Plot of the FMP and FMS intensity signals during the whole acquisition run.

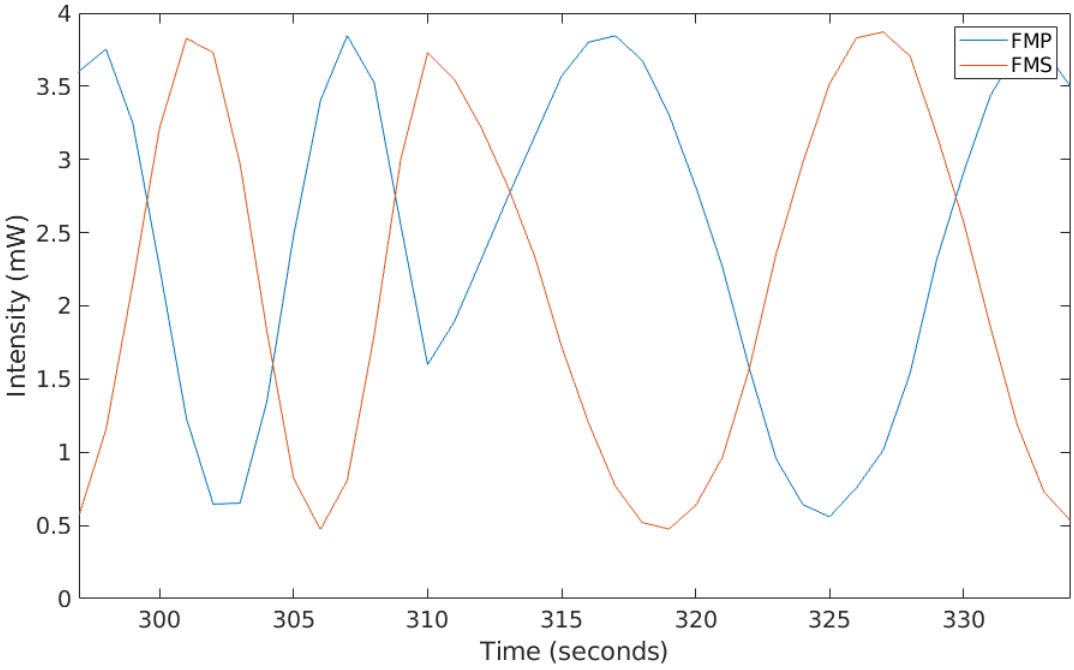

(b) 40 seconds long zoom on the intensity signals FMP and FMS. at second 310, one of the piezo's motion's inversion points is visible.

Figure 4.9: The intensity signal acquired by PD1 (FMP) and PD2 (FMS).

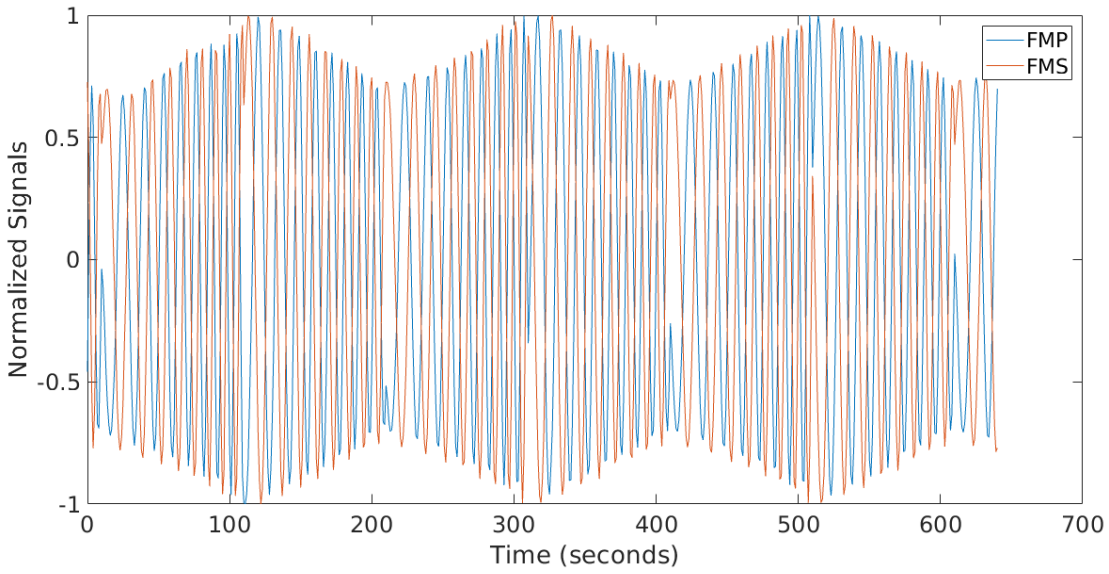

Figure 4.10: Plot of the normalized interferometric signals from FMP ($\sim \frac{\varepsilon(t)}{\varepsilon_0} cos(2k\Delta L)$ and FMS ($\sim \frac{\varepsilon(t)}{\varepsilon_0} sin(2k\Delta L)$ during the whole acquisition run. The two acquired signals lie now in the range [-1, 1] and the constant term has been subtracted.

A fundamental check before computing the atan2 is that of the phase offset between the two signals: only if it is $\frac{\pi}{2}$ the atan2 computation will work. The proper working and setting of the octal waveplate has to be checked. The best way to do it is to plot one signal versus the other one. If the offset is correct, the parametric plot of ($sin(\varphi)$, $cos(\varphi)$) should give an unitary circle. If the offset is not $\frac{\pi}{2}$ the plot is going to be ($sin(\varphi + \delta)$, $cos(\varphi)$) which is the parametric plot of an ellipse. The resulting plot is in figure 4.11:

As evident in figure 4.11(a) the offset induced by the octal-wave plate to the signal in the $\hat{s}$ polarization with respect to the $\hat{p}$ polarization is far away from $\frac{\pi}{2}$. This is probably due to a defect of the plate, as shown in appendix E.

Another step has then to be added to the analysis. The most straightforward way to correct this is to apply the sine addition equation (4.1):

$$sin(\varphi + \delta) = sin(\varphi)cos(\delta) + sin(\delta)cos(\varphi) \rightarrow sin(\phi) = \frac{1}{cos(\delta)}(sin(\varphi + \delta) - sin(\delta)cos(\varphi)) \tag{4.1}$$

Where $sin(\varphi)$ is now the correctly phase-offset sine signal, δ is the correction angle and $cos(\varphi)$ is the other signal, which has to be used as reference signal which establishes the null phase offset condition. The phase offset δ is chosen in order to make the points of the circle (y, x) with $x \sim -1$ to have y coordinate value as close to 0.

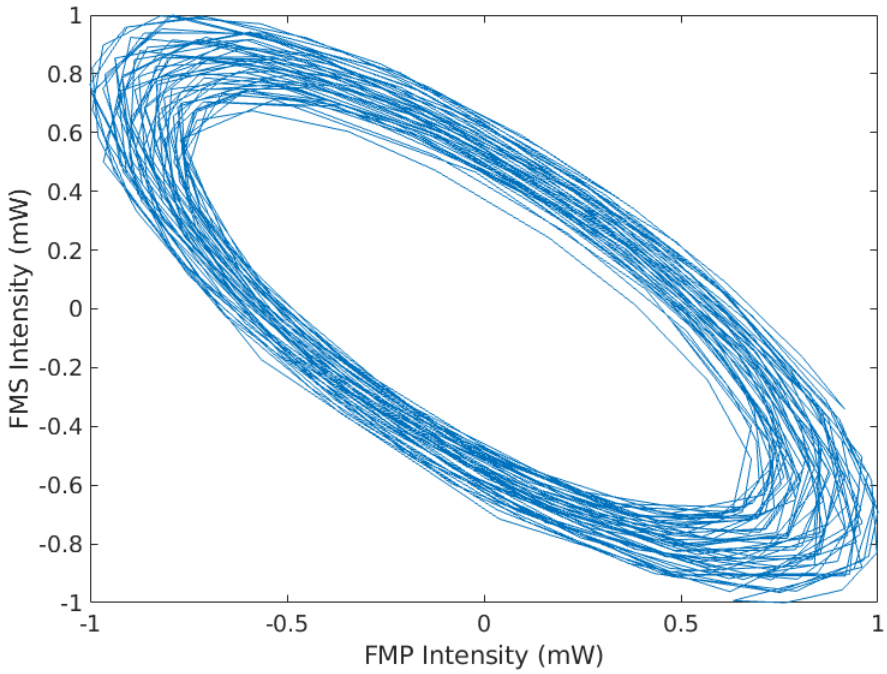

(a) The uncorrected FMS versus FMP plot

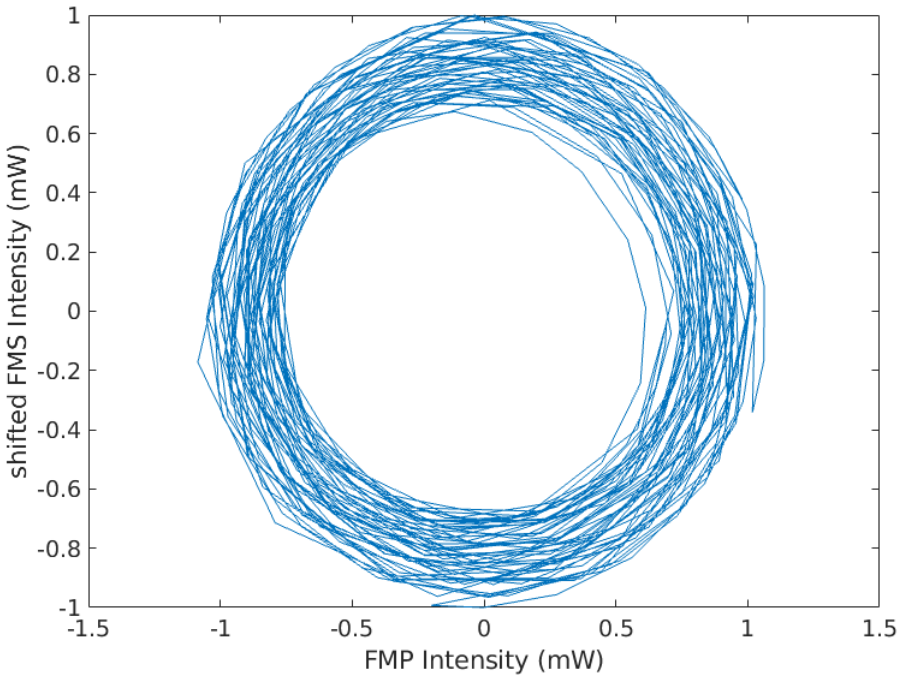

(b) The shifted FMS versus FMP plot

Figure 4.11: The FMS versus FMP plot to check the phase offset. The thickness of the ellipse is the effect of a non constant beam overlap.

At this point the atan2 computation can be performed, and as shown in section 3.4 the result will be independent on the normalization coefficient and on the beam overlap changes $\varepsilon(t)$.

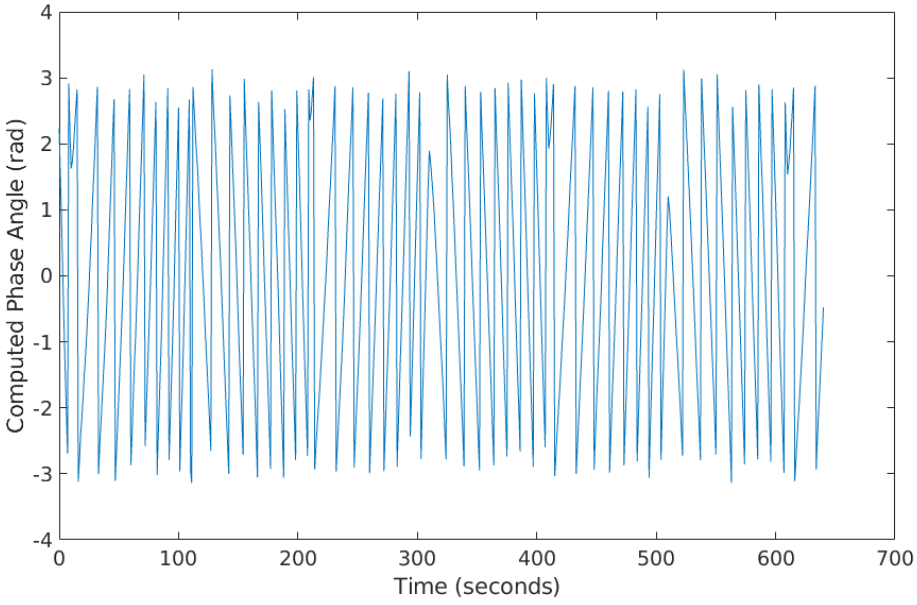

(a) Plot of the interferometer measured phase $phi(t)$ during the whole run.

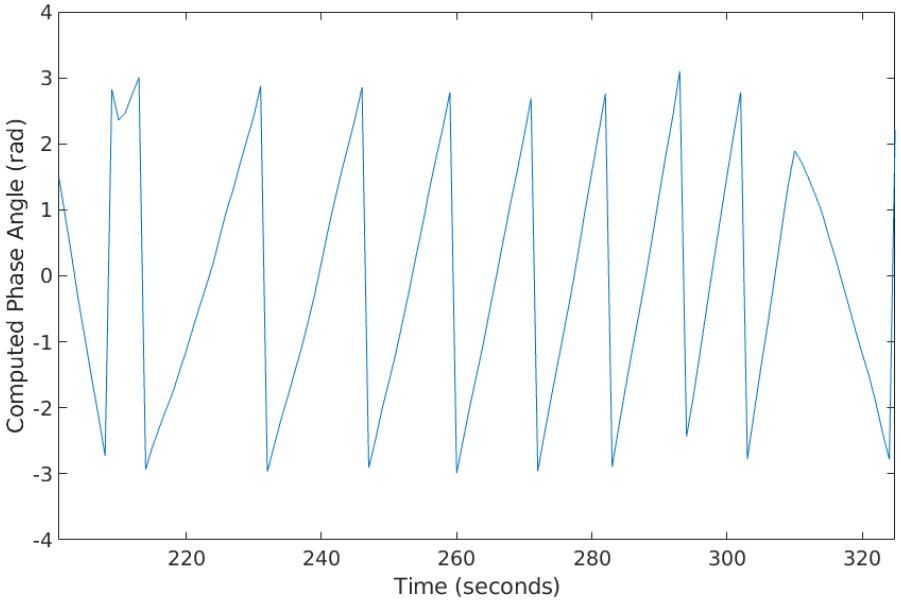

(b) Zoom of the interferometer measured phase $phi(t)$ along an increasing ramp. The vertical lines are the discontinuities due to the fringe crossings. A total of 8 fringe crossings is visible.

Figure 4.12: The computed phase $\phi(t) = atan2(sin(\varphi), cos(\varphi))$.

Figure 4.12(b) shows the interferometer measured phase. As evident from the zoomed region (4.12(b)), the number of fringe crossings between the two inversions is 8, rather than the 6 or 7 expected. The inversion points of the piezo's motion, corresponding to the changes of the ramp signal's slope, are also visible.

The result of the unwrapping and conversion into length is reported in figure 4.13:

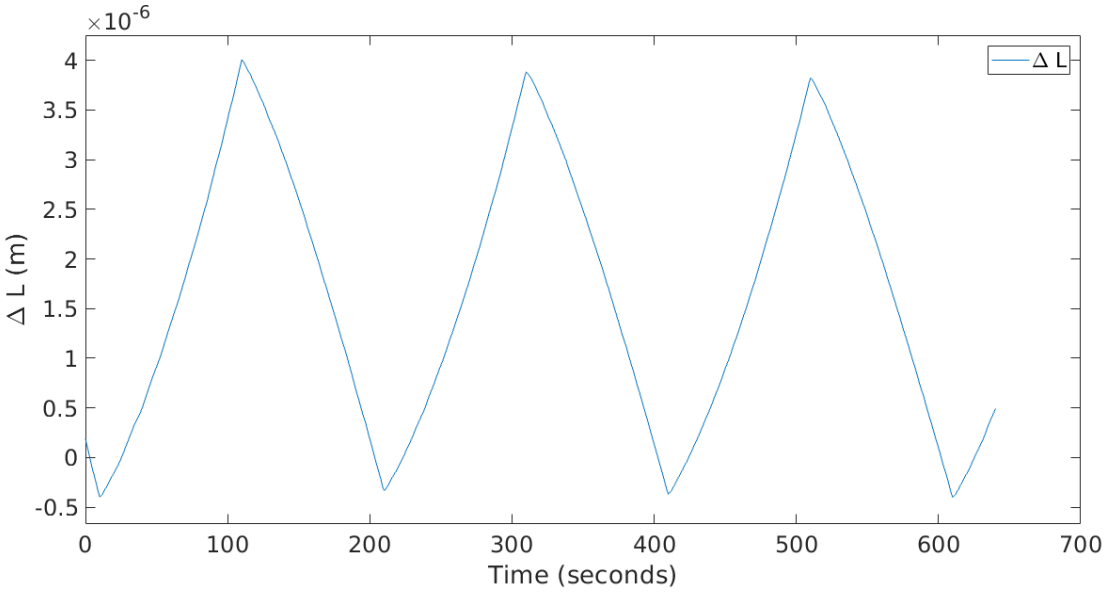

(a) The reconstructed motion during the full acquisition run.

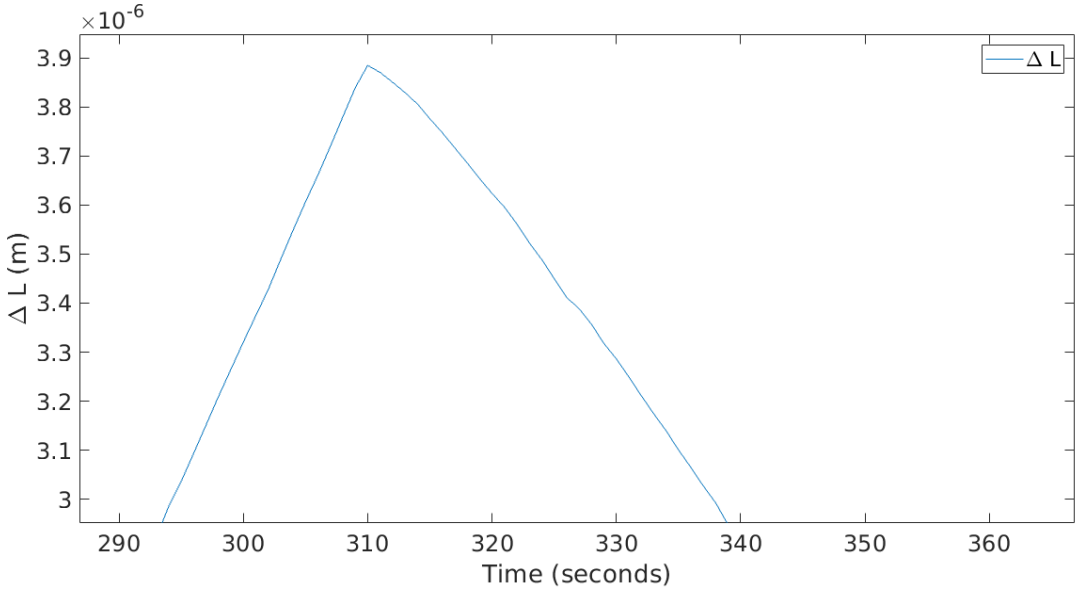

(b) Zoom on one inversion point of the piezo's motion.

Figure 4.13: The reconstructed position $\Delta L(t) = L_2(t) - L_1(t)$ of the piezo. $L_1(t) \approx L_1$ while $L_2(t) \approx L_{2,0} - x(t)$.

The unwrapping worked correctly, and all of the 2π jumps were removed. The ramp signal's shape, which guided the piezo's motion, is perfectly visible. The 'peak to peak' amplitude of the motion is $\Delta L = 4.41$, while the predicted amplitude of the piezo's motion is $\Delta x = k\Delta V = 3.44\mu m$. A "shark-fin" shape of the piezo's motion is visible, due to a non linearity in the piezo's response, and not to a readout error. Piezo crystals are known to have a non linear response as shown in [31].

In conclusion, the used method is able to follow the piezo's motion through more than one fringe, and the displacement measured with interferometry is compatible with the induced displacement of the mirror.

4.4 Test Setup Sensitivity to Temperature

A measurement was taken in the same conditions as picture 4.7 a whole night long to check what's is the effect of the room's temperature $T(t)$ on the interferometer. The analysis method was the same as previously. I show therefore the relative position of the two mirrors $\Delta L(t)$ (figure 4.14).

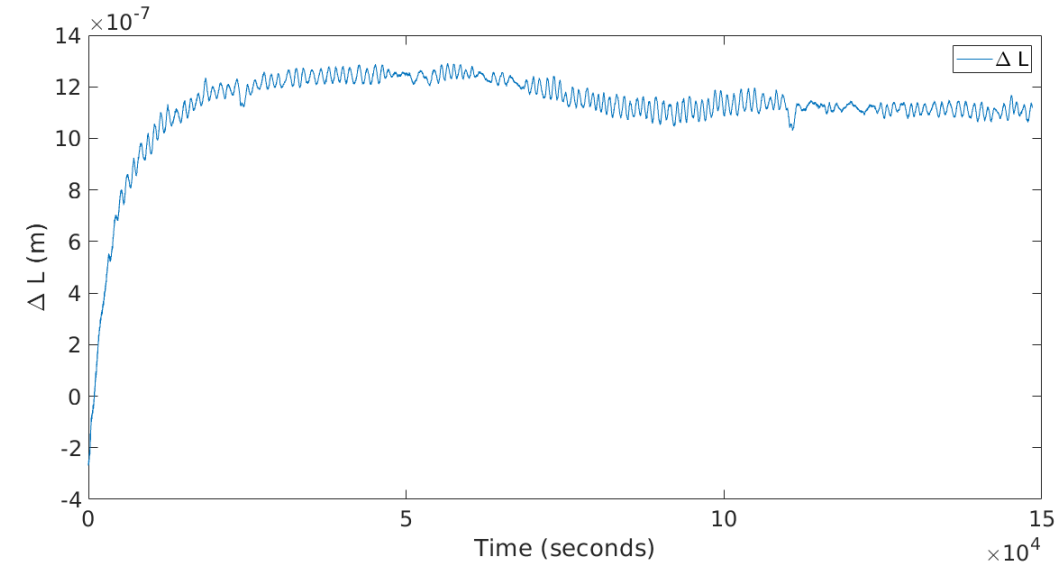

(a)

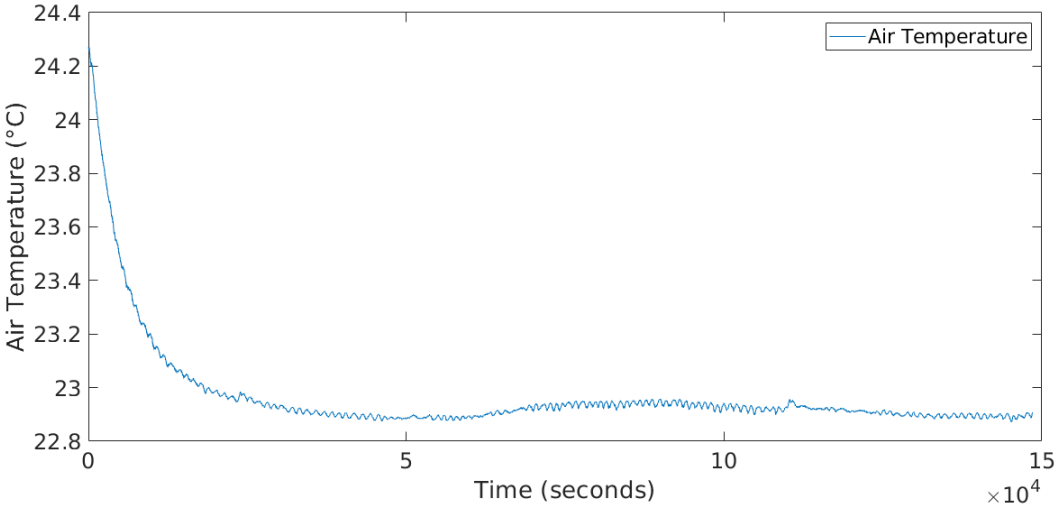

(b)

Figure 4.14: Above: the reconstructed relative distance of the two mirrors during the run. Below: the measured air temperatures during the night run.

The relative distance of the two mirrors ΔL changes quickly at the beginning of the measurement, and then slowly stabilizes, oscillating around a fixed value.

The temperature of the air in the room show a similar behavior, but with opposite sign (figure 4.14):

Correlation can be checked rescaling the temperature axis and plotting the temperature $T(t)$ together with $-\Delta L(t)$ (see figure 4.16). By zooming in one can see that both the

temperature and the relative distance oscillate on a 1000 second (20 minutes, 0.001Hz) scale, and that is the well known time scale of the cycles of the air condition system in the room.

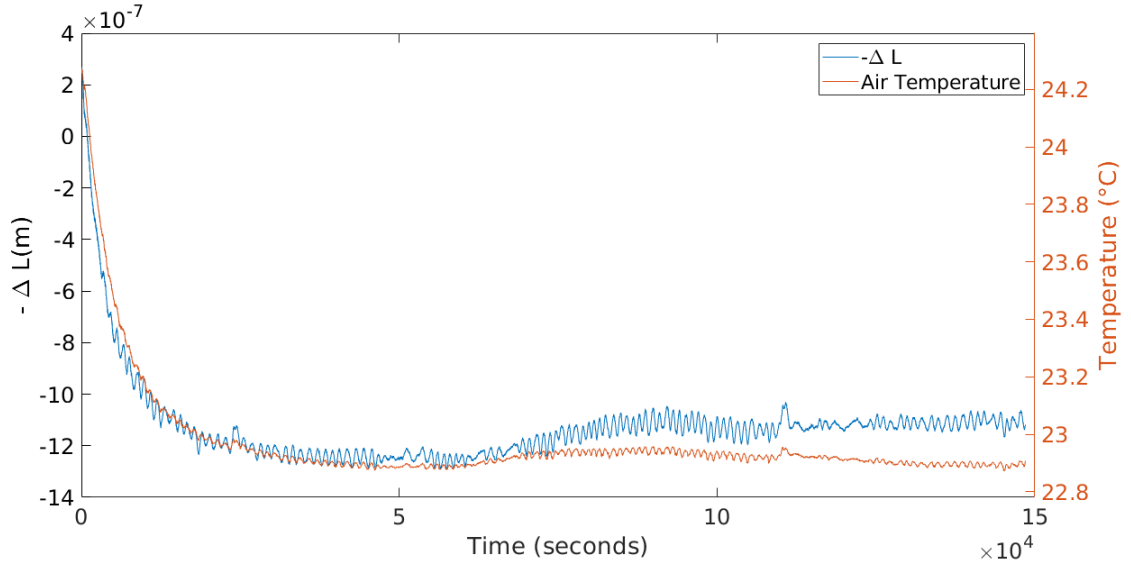

(a)

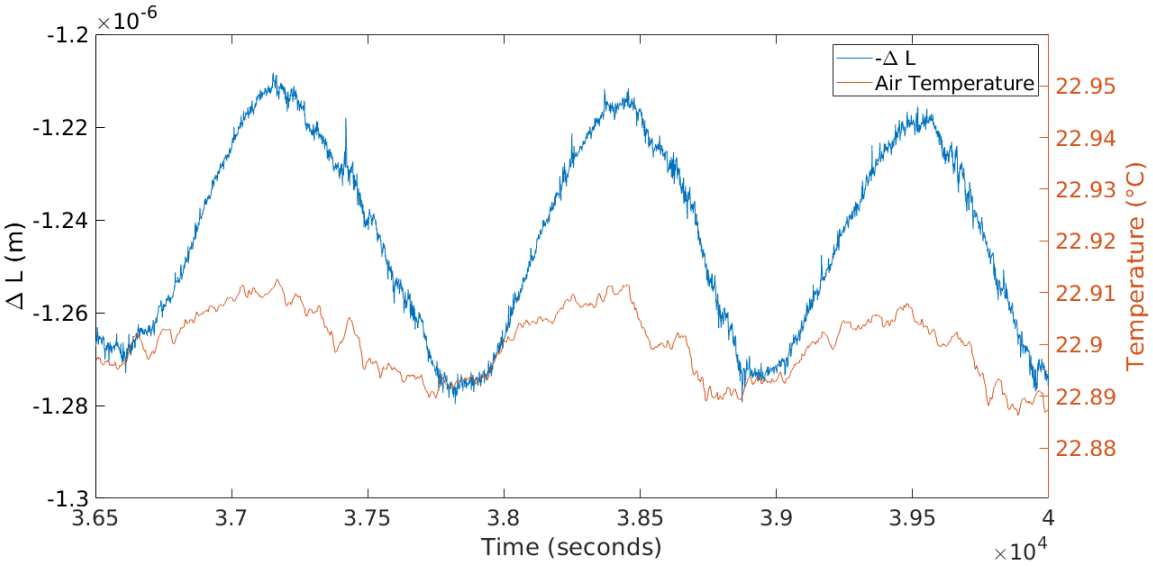

(b)

Figure 4.15: Above: Overlap of the two time series, the relative position $-\Delta L(t) = L_1(t) - L_2(t)$ (- Displacement) measured by the two interferometers and the rescaled temperature of the air. Below: a 1000 seconds long zoom showing three oscillations.

A ~ 0.03°C temperature variation in the air is inducing on the mirrors a relative motion of 0.1 μm. A magnitude square coherence computation (see appendix A) shows that $-\Delta L(t)$ and air temperature $T(t)$ are strongly correlated under $0.02Hz$ with a phase lag of $0.44rad$ ($\sim 70sec$ at $0.001Hz$) probably due to the thermal inertia of the mirror mountings.

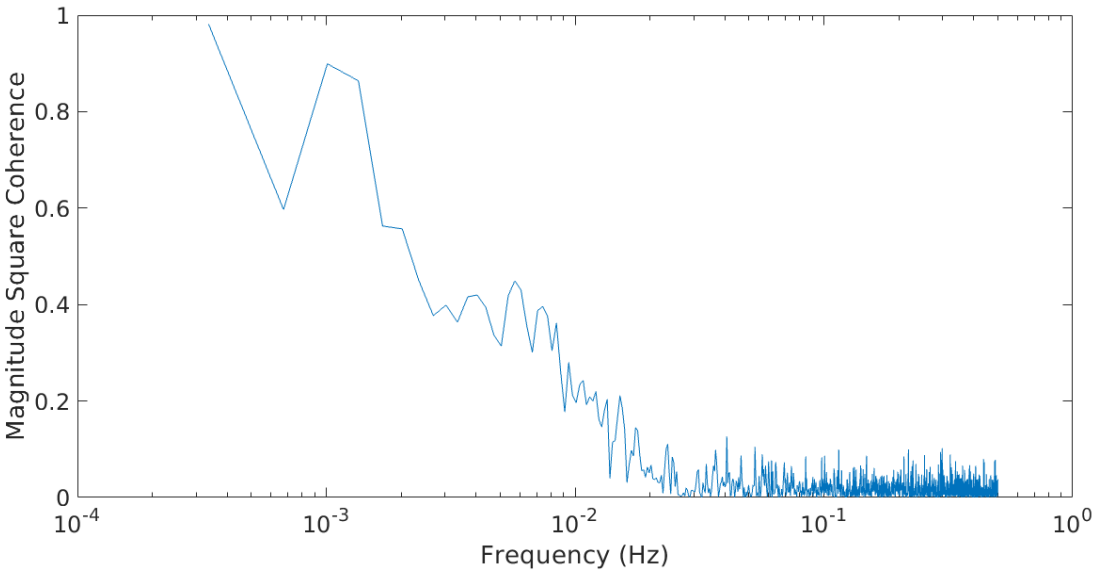

(a)

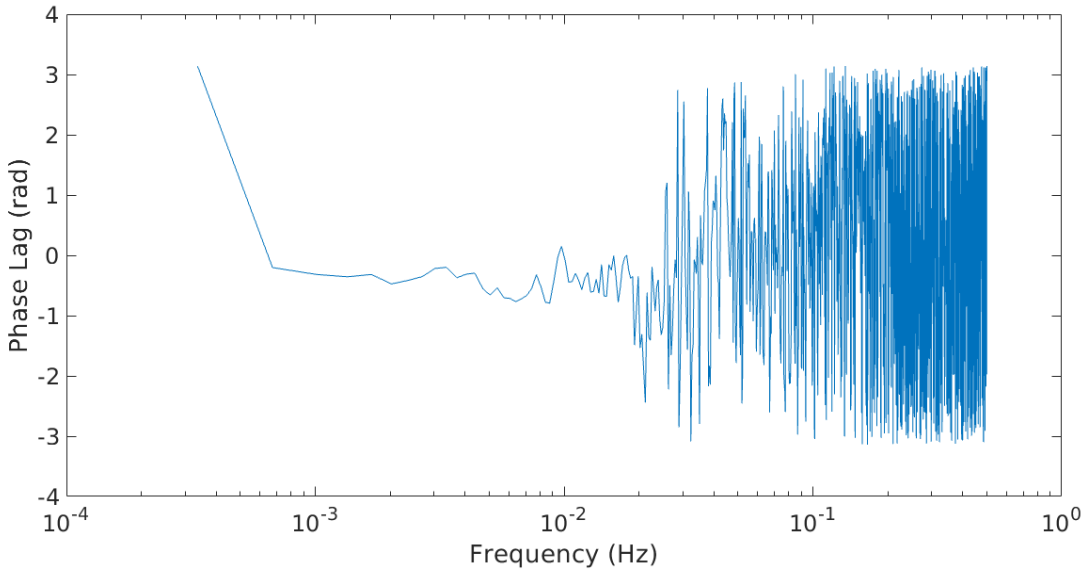

(b)

Figure 4.16: Above: magnitude square coherence of $-\Delta L(t)$ and air temperature $T(t)$. Below: phase lag between $-\Delta L(t)$ and air temperature $T(t)$.

This measurement is a direct check of how the setup in figure 4.7 is sensible to the air temperature's changes. During the experiment though the interferometer's bench will be kept in vacuum, and externally induced thermal effects are expected to be much smaller.

Chapter 5

Interferometric Measurement of the Oscillator's Motion

5.1 The Experimental Setup

After successful testing, we integrated the interferometer into our experiment. The interferometer bench is screwed to the two protrusions and lies right under the oscillator's cuboid mass (figure 5.1).

The oscillator needs to be isolated from noise factors that could excite the oscillator's resonance and hide the thermal noise's contribution. For our experiment, the principal noise issue is mechanical noise, caused both by sound waves in the atmosphere and seismic activity of the earth [9]. The oscillator is hence suspended through a cascade of mechanical filters and housed under vacuum. For the measurements reported in this thesis we re-used a setup that was developed as a prototype for the RareNoise experiment [9]. An additional mechanical filter is provided by the optical table supports which are pneumatic vibration isolators.

5.1.1 Heater

The heater (shown in figure 5.1)is a 3.6Ω resistance which heats due to Joule effect emitting radiation as a black-body at a temperature dependent on the flowing current, eg (6.0V, 1.8A) $\rightarrow 975°C$. The resistance is mounted in the focus of a parabolic mirror which reflects all the radiation towards the cuboid mass of the oscillator. The heater's datasheet reports that 80% of the radiated power is coupled with the heating target.

5.1.2 The Mechanical Filter

A mechanical filter is a mechanical oscillator resonating at a frequency f_0 much lower than the frequency of interest (the lowest frequency of interest is $300Hz$ in this case, since it is the frequency of the first transverse mode of the oscillator). An input vibration is then suppressed by the transfer function (5.1) in a low-loss regime:

$$T(\nu, \nu_0) = \frac{\nu_0^2}{\nu_0^2 - \nu^2} \tag{5.1}$$

The experiment re-uses the three-stage mechanical filter developed in the past as suspension prototype for the RareNoise experiment [9]. The three stages of our mechanical filter resonate at $\nu_0 \approx 38Hz$, while the whole system obviously exhibits a more complicated mode

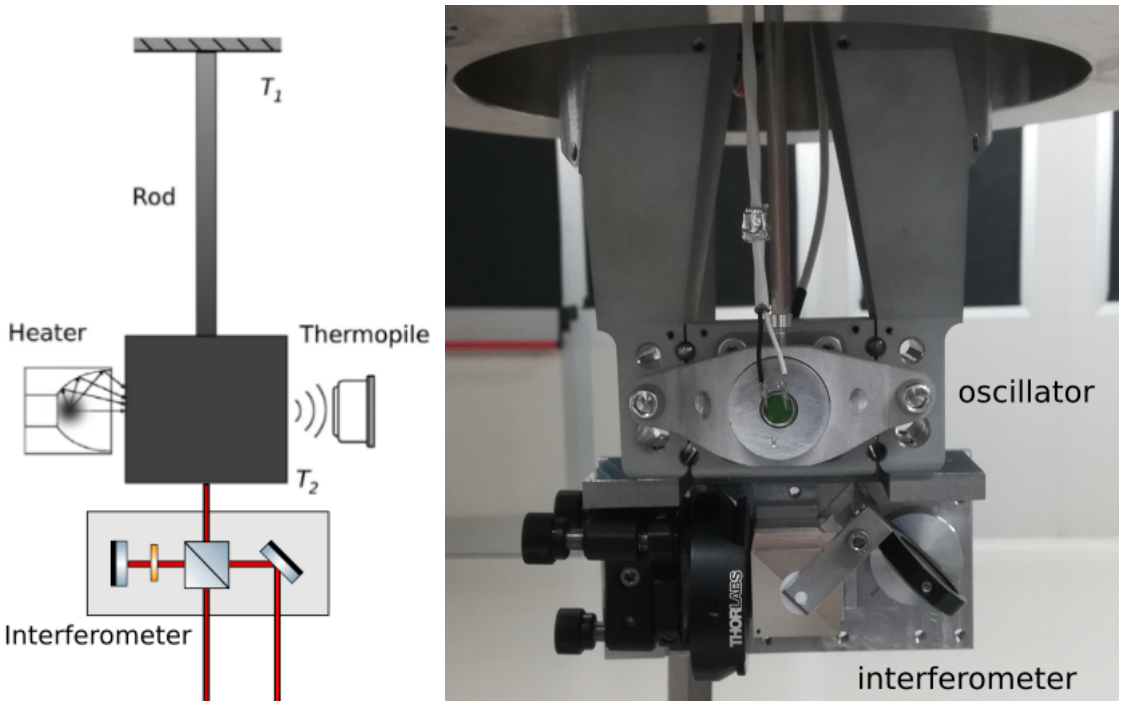

(a) (b)

Figure 5.1: (a) Scheme of the oscillator with the interferometer bench mounted under it, the thermopile and the heater. The beam's path is marked in red. The incoming beam is in the center. The forward output exits on the bottom right, and the return outputs follows the incoming beam's path the other way round. (b) Picture of the oscillator with the interferometer bench mounted under it. The interferometer bench hosts BS1, the rotator where the octal-wave plate is mounted and the reference mirror. In front of the oscillator's mass a support is holding the heater. For clarity, in figure (a) the oscillator, the heater and the thermopile are represented anticlockwise rotated of 90° on the vertical axis.

structure. The experimentally measured transfer function of the suspension is reported in figure 5.3. A picture of the suspension mounted over the vacuum chamber's base is reported in figure 5.2..

5.1.3 The Vacuum System

A scheme of the vacuum system is reported in figure 5.4. A glass window has been added on the base of the chamber to let the laser beam enter and exit. The vacuum chamber is set on the center of the optical table. The chamber's base lies on three cylindric $15cm$ long supports (figure 5.2). The vacuum pumping system used consists in a first stage dry scroll pump and in a second stage turbomolecular pump. A vacuum valve is placed between the turbo pump and the chamber. Three vacuum gauges (VG) are present to measure the pressure at the head of the first stage pump (VG3), at the head of the turbo pump (VG2), and in chamber (VG1).

If the turbo were directly connected to the chamber, it could lower the pressure in the chamber down to $\sim 10^{-6}mbar$, but it would induce a high mechanical noise to the optical table. Since we don't have vibration-free vacuum pumps available, we decided to add a sand box between the turbo and the vacuum chamber to absorb the vibrations. The sand box though has a very narrow vacuum tube inside with reduced conductance. The minimum

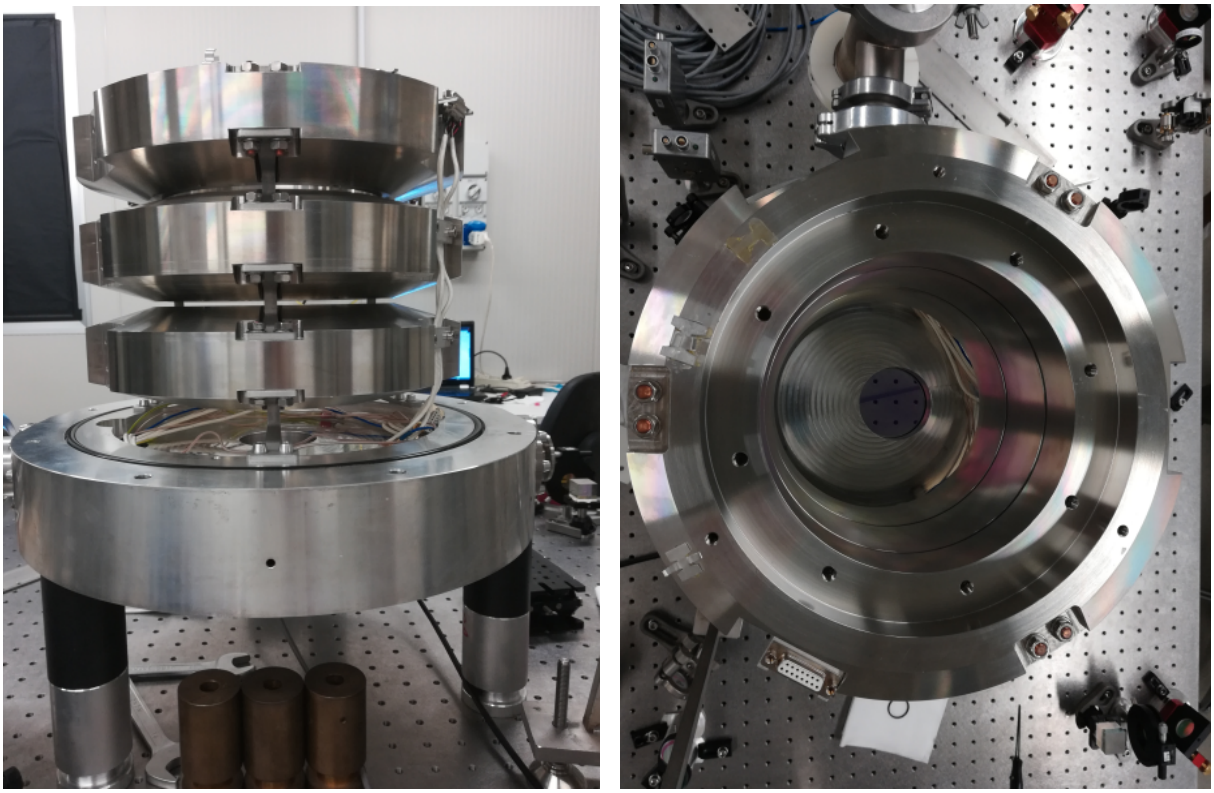

Figure 5.2: (left) Picture of the suspension system laying on the vacuum chamber's base. On the right of the suspension the white cables connecting the thermopiles, thermometers and heater are visible. (right) Picture of the suspension system seen from above. In the center at the bottom of the vacuum chamber the glass window is visible.

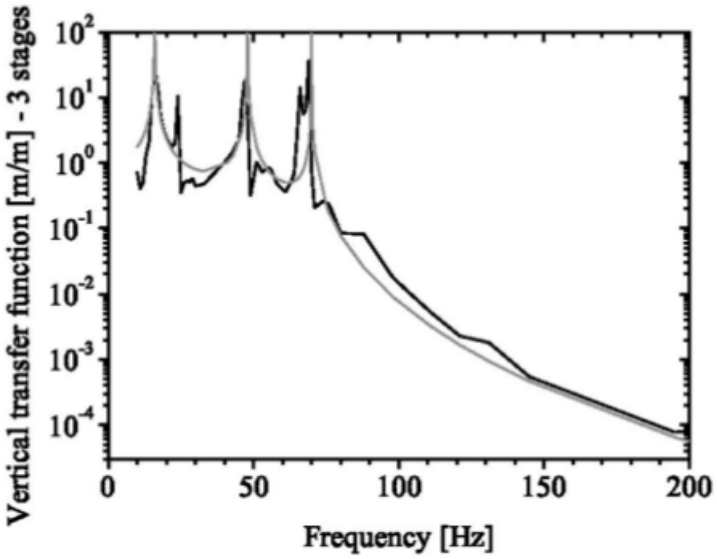

Figure 5.3: (left) Vertical Transfer function of the mechanical filter. The black line is the experimentally measured transfer function. The gray line is the prediction from the coupling in cascade of the three stages, which are three oscillators of masses, respectively, 17.4, 17.4, and 19.8kg and with $\nu_0 = 38Hz$. Picture from [9].

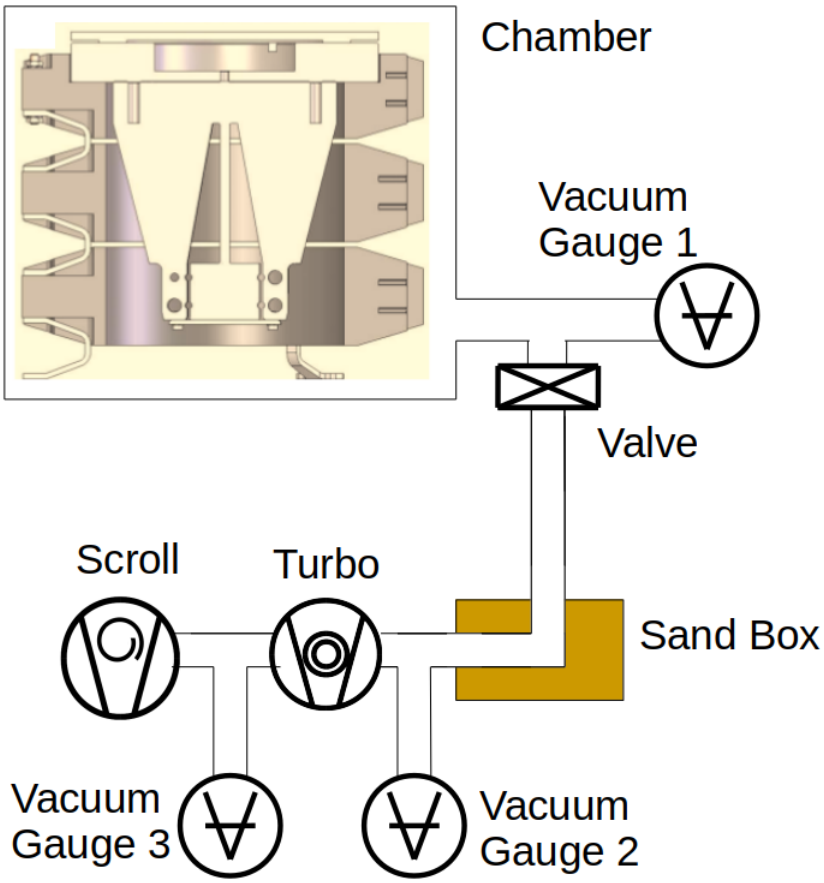

Figure 5.4: Scheme of the vacuum system used. In the vacuum chamber the oscillator is represented in white and lied over the three-stage mechanical filter. The vacuum in the chamber is achieved using first stage scroll pump and a second stage turbomolecolar pump. The pressure is measured in the points of interest with three vacuum gauges. The picture of the oscillator hosted on the suspension inside the vacuum chamber is taken from [9] and thus the fixed electrode is shown in place of the interferometer bench.

reached pressure in the chamber is $3 \cdot 10^{-5} mbar$.

5.1.4 Interferometer Setup

After the telescope depicted in figure 4.6(a) the beam is routed to the interferometer. The planned setup in figure 3.1 has been realized. Two leverage mirrors are used to divert the horizontally propagating beam upwards to the oscillator and then to divert the vertical, down propagating beam back to horizontal. The forward and backward outputs and PD5 are detected using SN7-11 characterized in section E.7. A schematic picture of the setup in the vacuum chamber is reported in figure 5.5. Two pictures of the entire setup are reported in figure 5.6. A detail of the two outputs is reported in figure 5.7.

5.1.5 Acquisition System

Our acquisition system is based on a National Instruments PXI platform. The outputs of the four photodiodes are acquired using a 24-bit resolution ADC NI PXI-4462 DAQ board, which acquired at 8k Samples/sec in a $\pm$10V range (fast channels). All temperature sensors (room temperature, T_1 and T_2 on the oscillator) and environmental monitor signals (the pressure in the chamber and after the pumping stages) are acquired at 1 Sample/sec by NI 9219 24-bit universal analog inputs (slow channels). NI LabView was used to develop the acquisition software, which during the acquisition also provides live data view from the fast acquired channels and from the slow channels. Data storage is arranged in txt data format. Data analysis is carried out offline with Matlab.

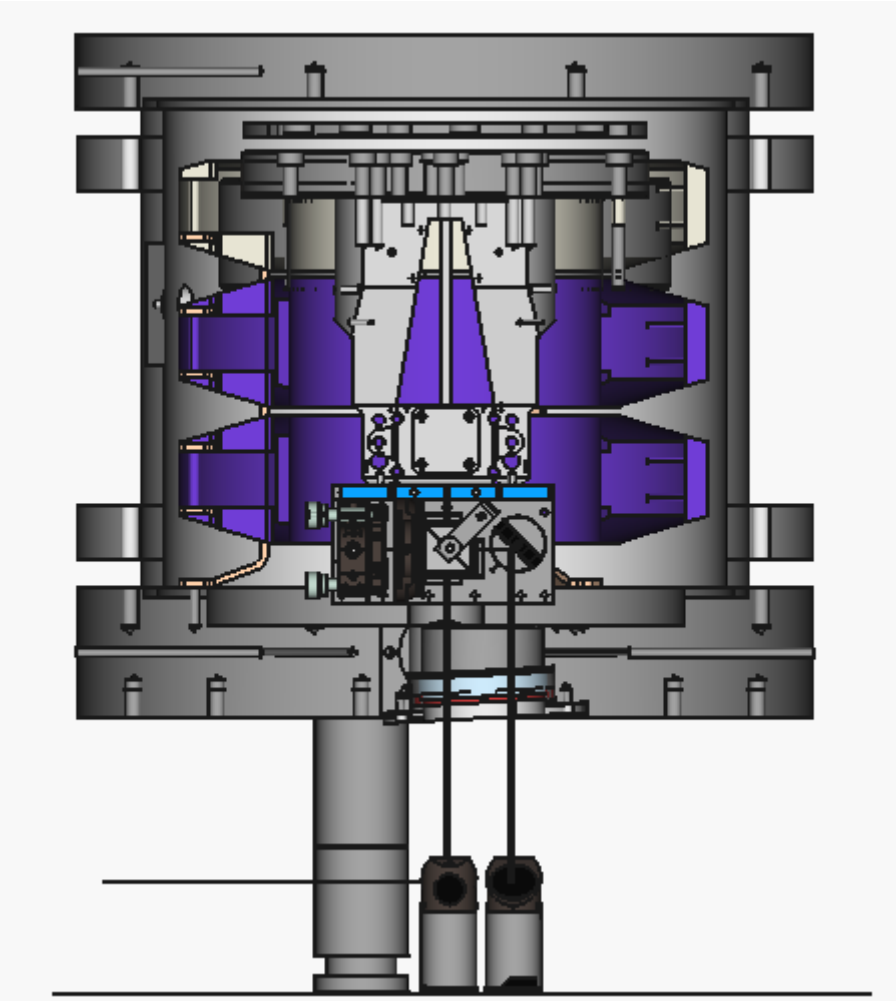

Figure 5.5: Schematic picture of the experimental setup. The oscillator (compare with figure 5.1) is in the center. The two protrusions beside the oscillator hold the interferometer bench. The top of the rod is holded by a cylindrical plate which is lied over the mechanical filter (compare with figure 5.2). The first two stages of the mechanical filter system are colored in purple, and the third stage is gray. The mechanical filter's bottom springs are screwed to the chamber's base. On the chamber's base the glass windows is drawn. The chamber lies over three cylindrical supports (only one is shown in this picture) which hold the chamber 15cm over the optical table. On the table the two 45° mirrors reflecting the beam (represented by the black lines) towards the interferometer are drawn.

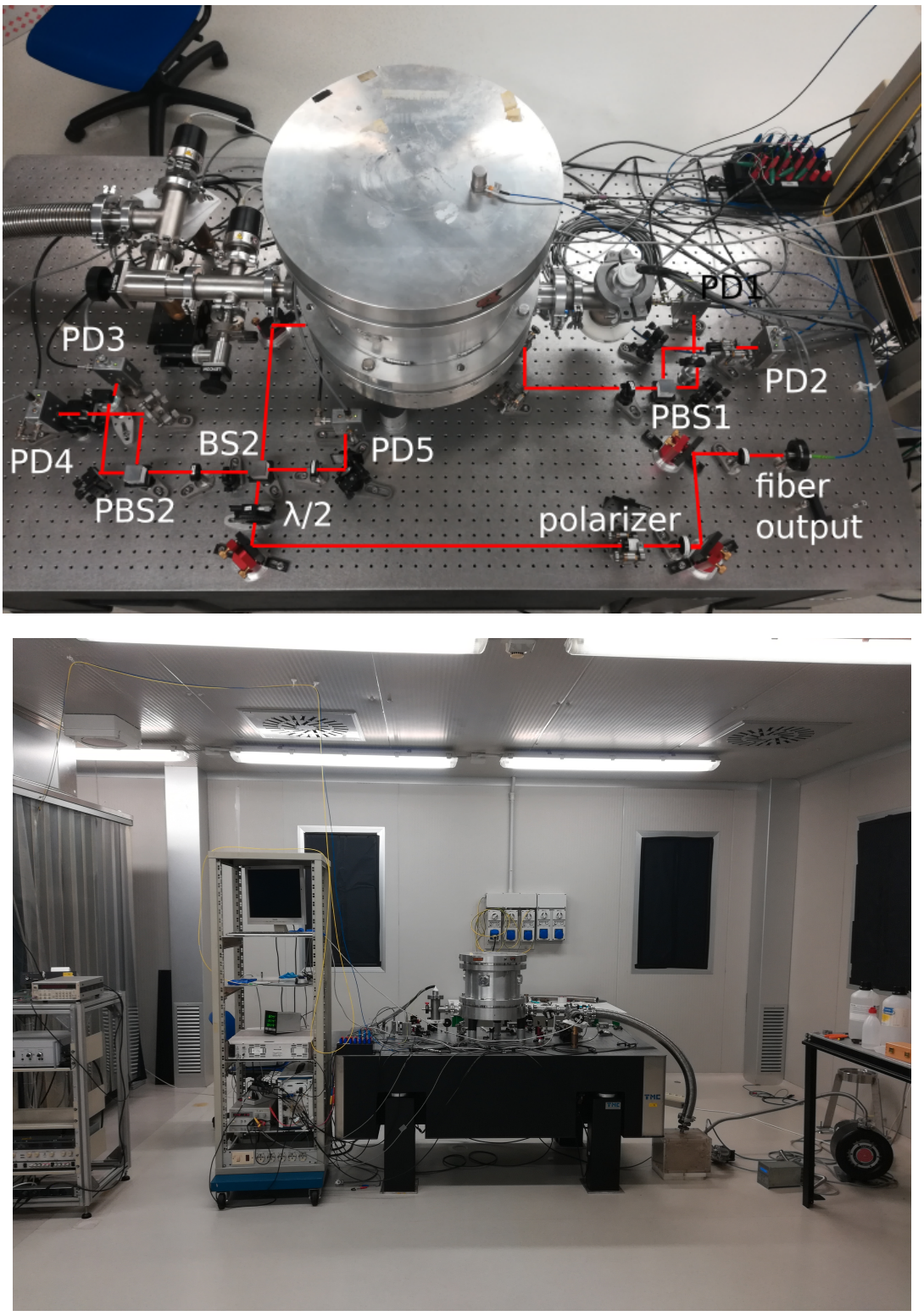

Figure 5.6: (above) Picture of the setup of our experiment. The setup is that of figure 3.1, where some mirrors and four more polarizers have been added. For a detailed picture of the outputs see figures 5.7. (below) Picture of the complete setup inside the clean room. The squeezer bench is on the left, hidden by the curtains. In the center the optical table is visible. The PM fiber is the blue 'cable' exiting from the squeezer bench, being hold on the ceiling and whose output is on the Rarenoise table. The vacuum chamber has then been set on the center of the bench, while on the right the two used vacuum pumps and the sand box are visible. The bottom level of the rack on the left is hosting the acquisition system, and the voltage supply modules.

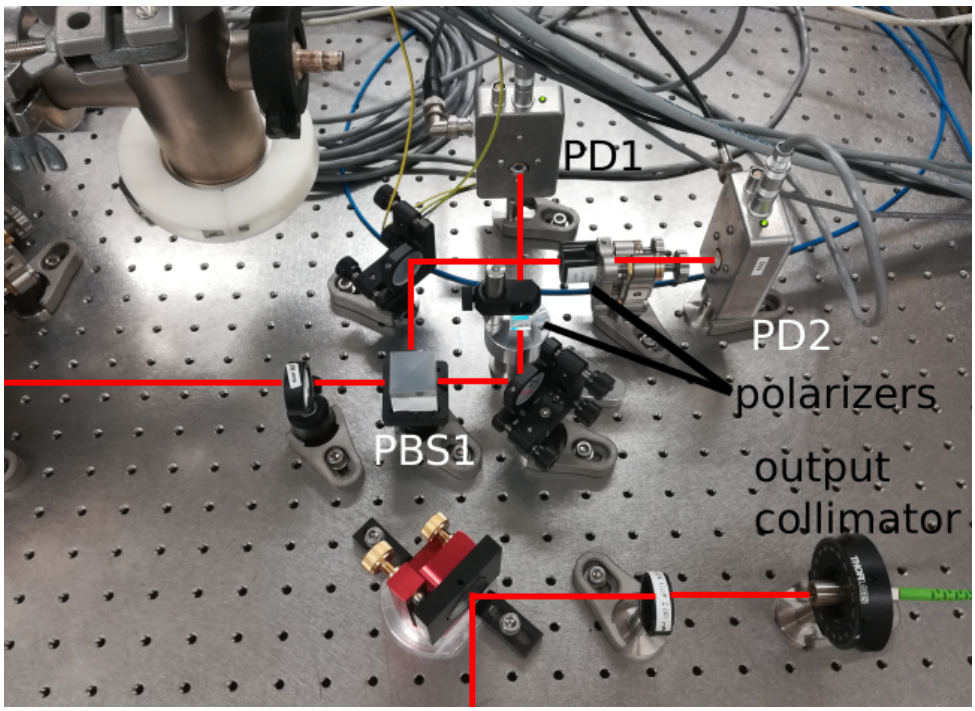

(a) Picture of the Forward Output of the interferometer. A lens focalizes the beam on the photodiodes. PBS1 splits the output beam in the two polarizations components. The two outputs are acquired by photodiodes SN7 as PD1 and SN9 as PD2. On the bottom the fiber's output and the optical telescope going to the interferometer are visible.

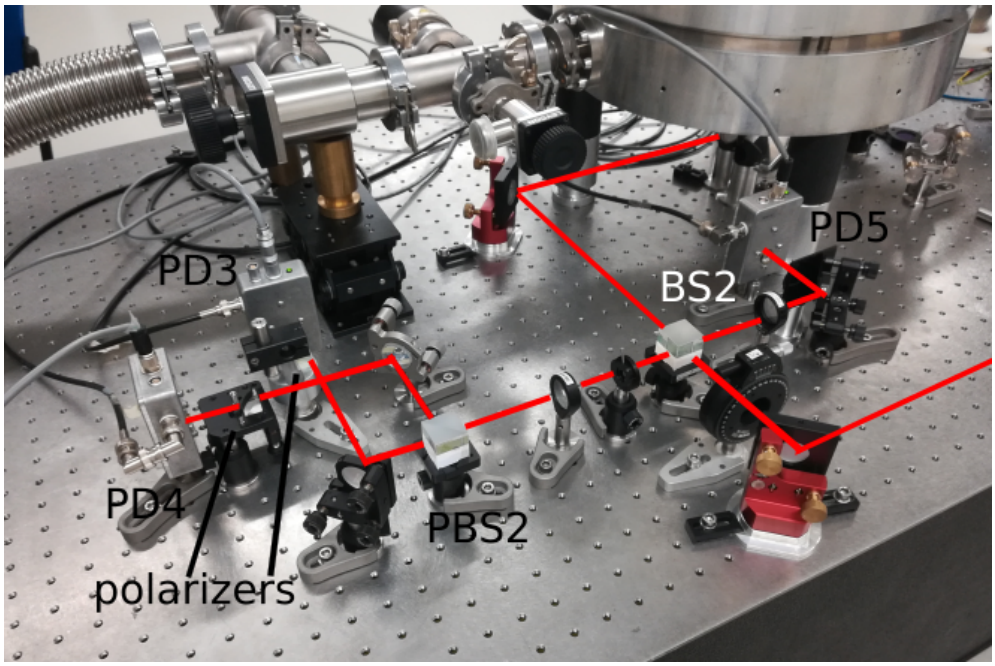

(b) Picture of the Return Output of the interferometer. The input beam is coming from the right of the picture. Half of the intensity is reflected by BS2 and is detected by the SN11 photodiode as PD5. Half of the beam is transmitted towards the interferometer. The returning beam is intercepted by BS2 and reflected towards second output. A lens focalizes the beam on the photodiodes. The beam is splitted by PBS2 into its two polarizations and reflected towards SN8 as PD3 and SN10 as PD4.

Figure 5.7: Pictures of the two interferometers' outputs with the beam's path highlighted. To improve the polarization selection, four polarizers have been added after PBS1 and after PBS2 (see section 5.4).

5.2 Noise Budget

We measured the dark noise of the five readout photodiodes to have a white spectrum from a 10Hz to 4000 Hz at a $2.5 \cdot 10^{-8} V/\sqrt{Hz}$ level (see figure 5.8). We set the maximum intensity from the interfering beam to be lower than 2mW, so that the two outputs FMP and FMS would not distort, exploiting the full 10V range of the ADC. The two outputs RMP and RMS have half of this intensity and were also acquired in the ±10V ADC range since the lower setting is $\pm 3.16V$. On the $\pm 10V$ range setting, the noise spectrum from the ADC was also measured to be a white spectrum at a $7 \cdot 10^{-8} V/\sqrt{Hz}$ level (see figure 5.8).

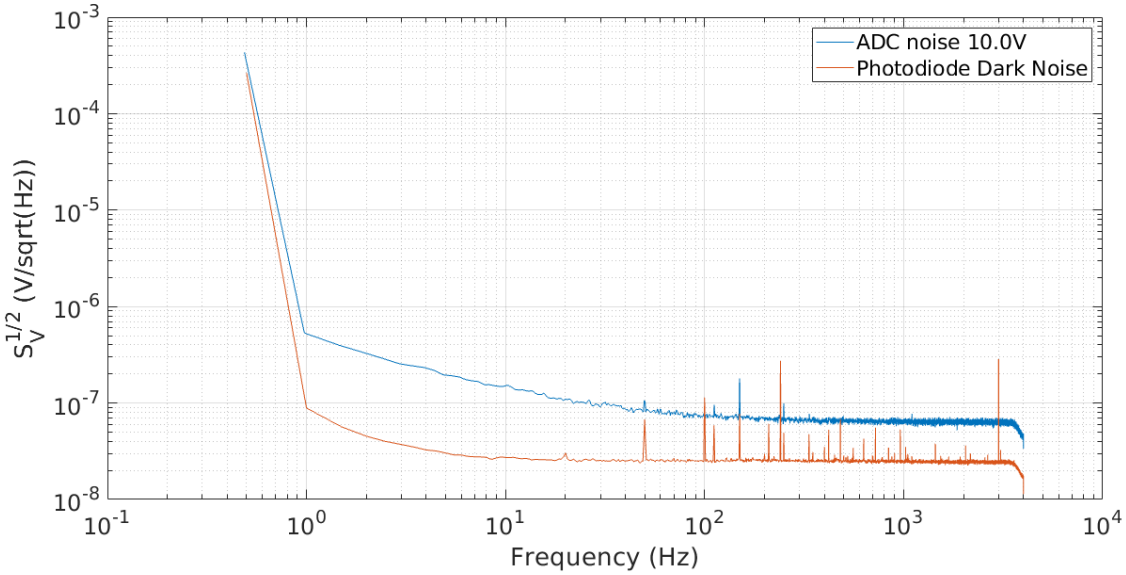

Figure 5.8: (blue) The dark noise from the SN7 photodiode. The five used photodiodes(SN7, SN8, SN9, SN10 and SN11) have the same white noise spectrum. The noise spectrum from the photodiodes is a factor ~ 3 lower than the acquisition noise. (red) The noise level from the ADC in the ±10V range measured in the first ADC channel with a 50Ω tap on it. The noise level in the 4 channels was the same.

The expected noise level caused by *shot noise* for a $2mW$ beam is:

$$S^{\frac{1}{2}}_{shot\,noise} = \sqrt{I\hbar\frac{2\pi c}{\lambda}} = 5.9 \cdot 10^{-12} W/\sqrt{Hz} \tag{5.2}$$

Using the calibration from the photodiodes, the shot noise level corresponds to $3.0 \cdot 10^{-8} V/\sqrt{Hz}$, and hence the photodiodes are shot noise limited.

We then computed the displacement noise induced by the :

$$I(\Delta L) = I_0(1 + cos(2k\Delta L)) \rightarrow \frac{dI}{d\Delta L}(\Delta L) = I_0 sin(2k\Delta L)2k \tag{5.3}$$

As expected, the sensitivity with respect to position of a single interferometer depends on where the interferometer is sitting in the fringe, and is the reason why we are using a *quadrature homodyne interferometer*. In a naive approach, taking into account one interferometer at a time, when one interferometer's sensitivity is low, the other $\pi/2$ offset interferometer's sensitivity is high and vice versa. The worse combined sensitivity happens when both interferometers sit at $2k\Delta L = \pi/4$ and $sin(2k\Delta L) = \frac{\sqrt{2}}{2}$. Hence one can evaluate the voltage

sources contribution in the case of worse sensitivity using

$$\frac{d\Delta L}{dI} = \frac{\lambda}{2\sqrt{2}\pi I_0} \tag{5.4}$$

and

$$S_{\Delta L}^{1/2}(\omega) = \frac{d\Delta L}{dI}\frac{dI}{dV}S_V^{1/2}(\omega) \tag{5.5}$$

where $\frac{dI}{dV} \sim 0.2\frac{mW}{V}$ is the calibration of the photodiodes (see appendix E). Comparing the three noise sources we conclude that the spectrum is dominated by the acquisition noise, and that the minimum achievable sensitivity with the setup is slightly below $2 \cdot 10^{-15} m/\sqrt{Hz}$. A plot of shot noise, photodiodes noise and ADC noise is reported in figure 5.9.

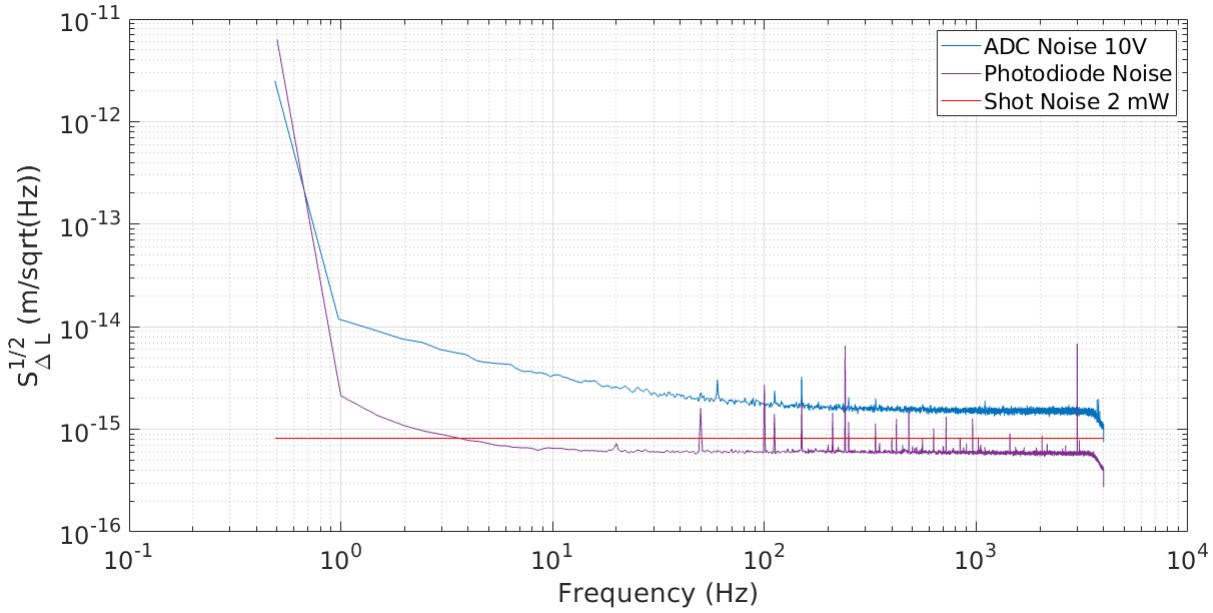

Figure 5.9: Plot of the noise level from shot noise $\sim 8.2 \cdot 10^{-16} m/\sqrt{Hz}$, photodiodes noise $\sim 6 \cdot 10^{-16} m/\sqrt{Hz}$ and ADC noise $\sim 1.2 \cdot 10^{-15} m/\sqrt{Hz}$

5.3 Three Photodiodes Phase Readout Results

We report the analysis results of a 10 minute long acquisition using the 3PDR described in section 3.5. Outputs FMP, FMS and the input intensity were acquired.

During this measurement, the measured $\Delta L(t)$ in smaller than one wavelength, and both interferometers are sitting at a fourth of the fringe, and hence the photodiodes measure a low intensity (see figure 5.10. Therefore to provide the calibration of the signal, at the end of the run we hit the suspended optical bench supporting the chamber thus making the two interferometer arms undergo a full fringe of relative motion. The measured visibilities are $V_{FMP} = 97.5\%$ and $V_{FMS} = 98.4\%$. Visibility is expected to be the same for the two outputs. The difference is probably caused by a non perfect polarization selection by PBS1. The setup is using the additional polarizers shown in figure 5.7.

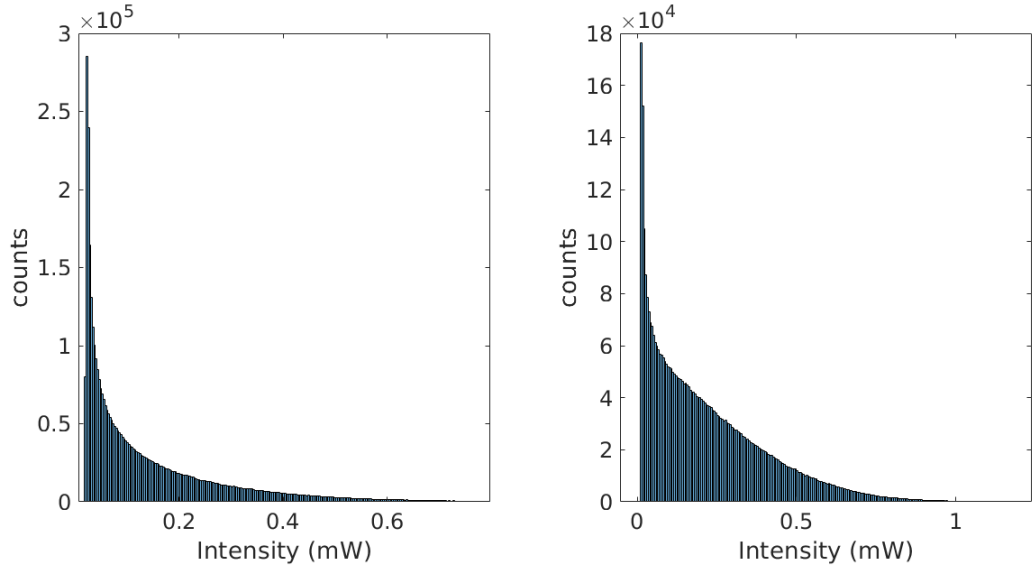

Figure 5.10: Histogram of the intensity measured by FMP (left) and FMS (right) during the run.

The measured phase angle can be shown plotting $(y, x) = (sin(\phi(t)), cos(\phi(t)))$ as shown in figure 5.11. The correction angle was different from the angle used during the testing in section 4.3 because while attaching the interferometer to the oscillator we did a few attempts to optimize the octal wave-plate rotation; however we were not able to obtain the desired $\pi/2$ offset between the two interferometers (see section E.6).

We finally computed the PSD of the measured relative position $\Delta L(t)$. Figure 5.12 shows the difference in performance between the Two Photodiode Readout and the 3PDR. The two perfectly match under $50Hz$, but then differ when laser intensity fluctuations dominate the noise. Laser intensity fluctuations limit the 2PDR's spectrum to reach a best of $\sim 10^{-13} m/\sqrt{Hz}$ sensitivity around $600Hz$ while the Three Photodiode Readout reaches a flat noise level of $4.8 \cdot 10^{-15} m/\sqrt{Hz}$ above $1350Hz$. This can be again checked plotting the *magnitude-square-coherence* of the input intensity $I(t)$ and relative displacement $\Delta L(t)$ (figure 5.13). Correlation between input intensity and relative displacement above $150Hz$ is strongly suppressed by adding the input intensity information to the analysis. The phase lag plots show that the lag is a continuous function of the frequency where the two signals are correlated.

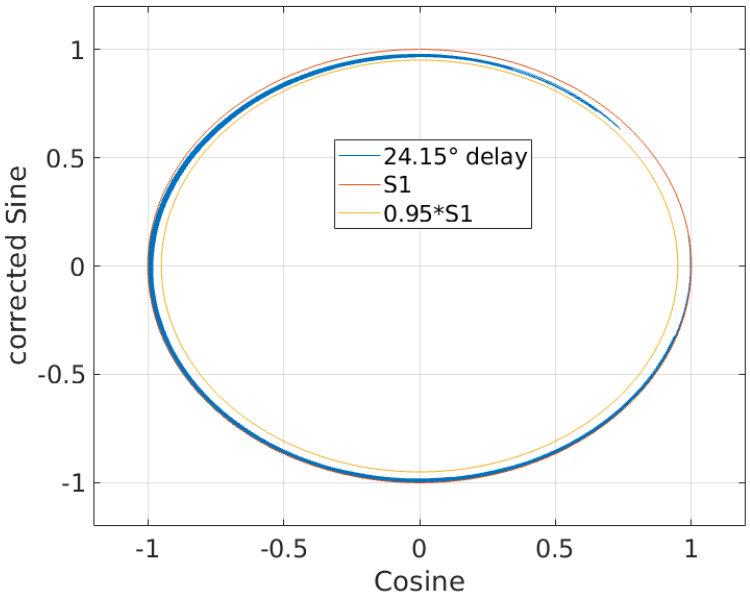

Figure 5.11: Plot of $(y, x) = (sin(\phi(t)), cos(\phi(t)))$. The $\hat{s}$ signal has been shifted by a 24.15° angle using equation (4.1). This plot can be compared with an unitary radius circle indicated by S1 and a 0.95 radius circle indicated by 0.95*S1.

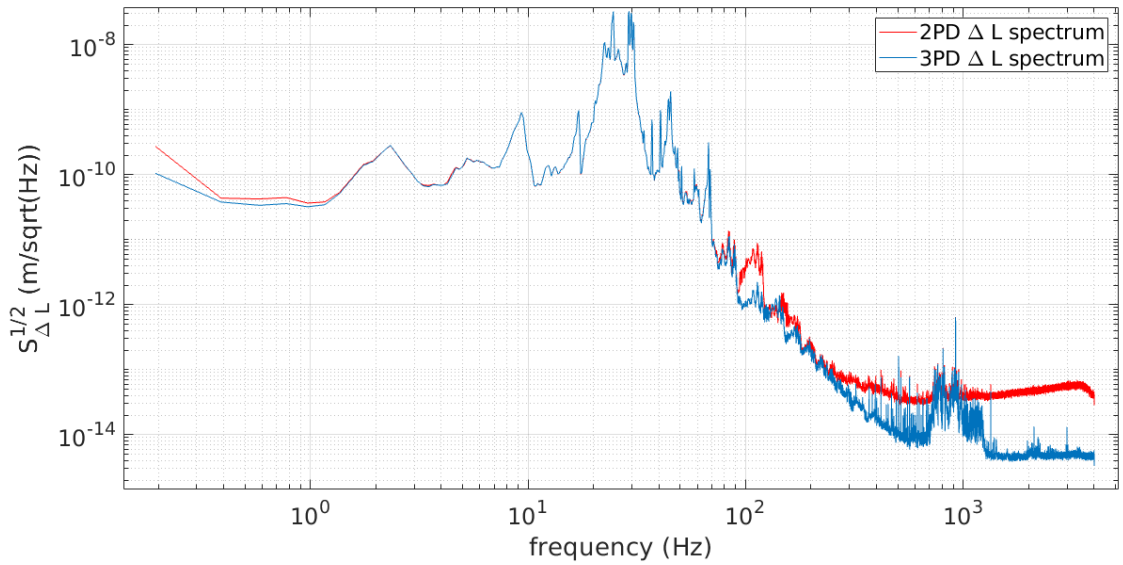

Figure 5.12: (blue) Square root of the time average PSD of $\Delta L(t)$ estimated with 3PDR. (red) Square root of the time average PSD of $\Delta L(t)$ estimated with 2PDR. The two spectra were computed from the same sample with a $0.194Hz$ resolution.

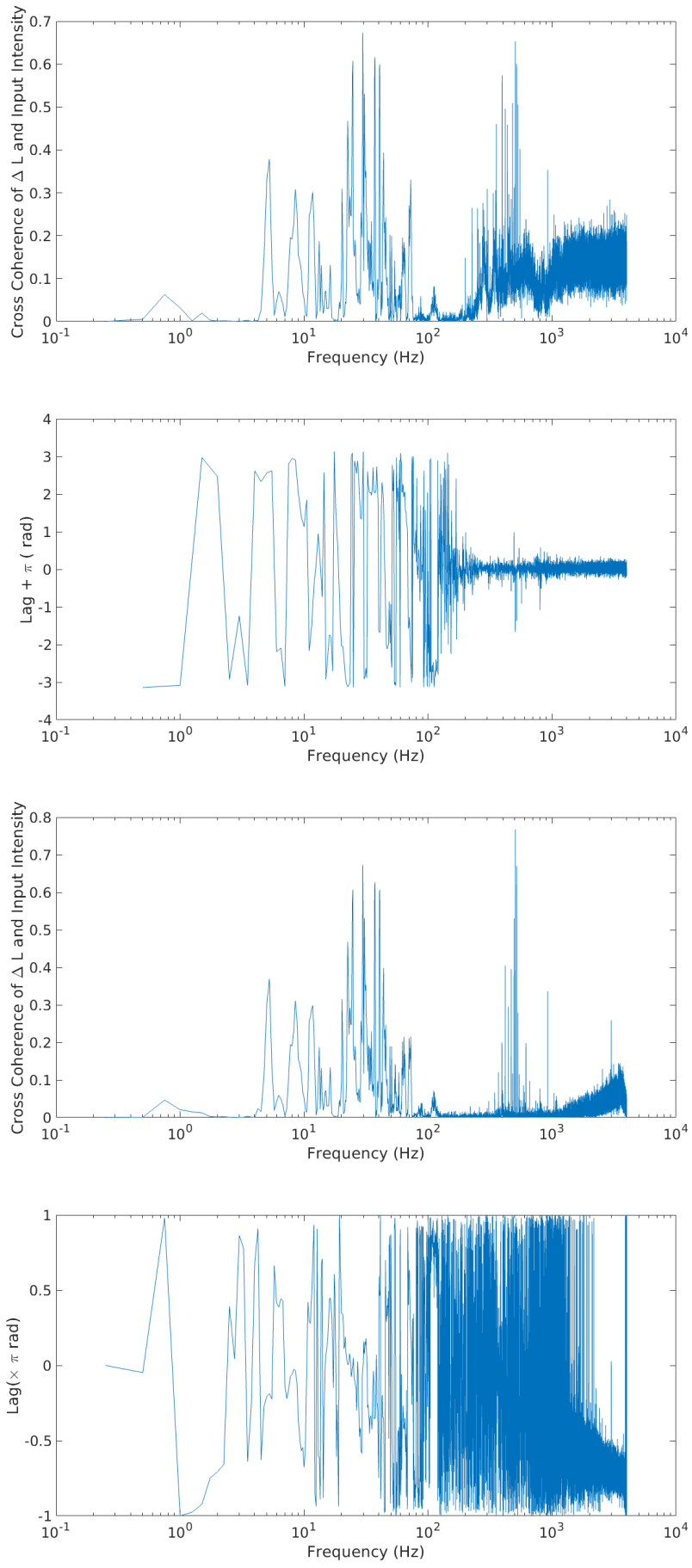

Figure 5.13: Magnitude square coherence and phase lag of input intensity $I(t)$ and relative displacement $\Delta L(t)$ measured with the 2PDR (above) and 3PDR (below).

5.4 Four Photodiodes Phase Readout Results

We report here the analysis result of the 4PDR (section 3.6). From a histogram of the measured intensities (figure 5.14) one can see that the $\hat{p}$ interferometer was sitting in the middle of a fringe while FMS was in the minimum and RMS at the maximum.

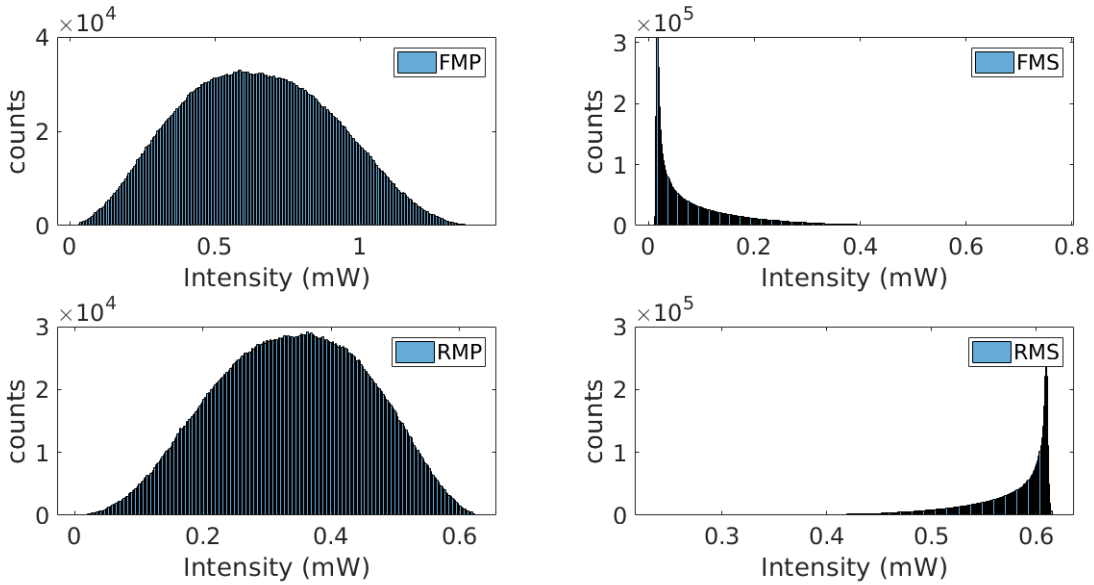

Figure 5.14: Histograms of the four acquired outputs.

The first step of the analysis is the estimation of the summation coefficients for $\hat{p}$ and $\hat{s}$. This can be done by plotting $(y, x) = (RMP(t), FMP(t))$ and performing a linear fit. In a simplified representation FMP: $\sim \alpha_f - \beta cos(\varphi)$ and RMP $\sim k_p(\alpha_r + \beta cos(\varphi))$, hence expressing RMP as a function of FMP:

$$(y, x) = (k_p(\alpha_r + \beta cos(\varphi)), \alpha_f - \beta cos(\varphi)\,) \rightarrow (y(x), x) = (k(\alpha_r + \alpha_2 - x), x) \tag{5.6}$$

The slope of the linear fit k_p multiplied by -1 gives the summation coefficient.

This procedure turned out to be useful also as diagnostic tool, being a strong check of the polarization selection by PBS1 and PBS2. The first time we tried this analysis, instead of two lines, two narrow ellipses appeared, manifesting a phase delay between the two same-polarization outputs. An example of this is reported in figure 5.15 . This was due to a non perfect separation of the two polarizations and hence a small part of the s-interfering signal was measured by the $\hat{p}$ photodiodes and vice versa. Therefore four more polarizers have been added to the setup, two before PD1 and PD3 selecting $\hat{p}$ and two before PD2 and PD4 selecting $\hat{s}$, obtaining a much better polarization selection as shown in figure 5.16. The spectra from the 3PDR would not have the current noise floor if no 4PDR diagnostic had been made.

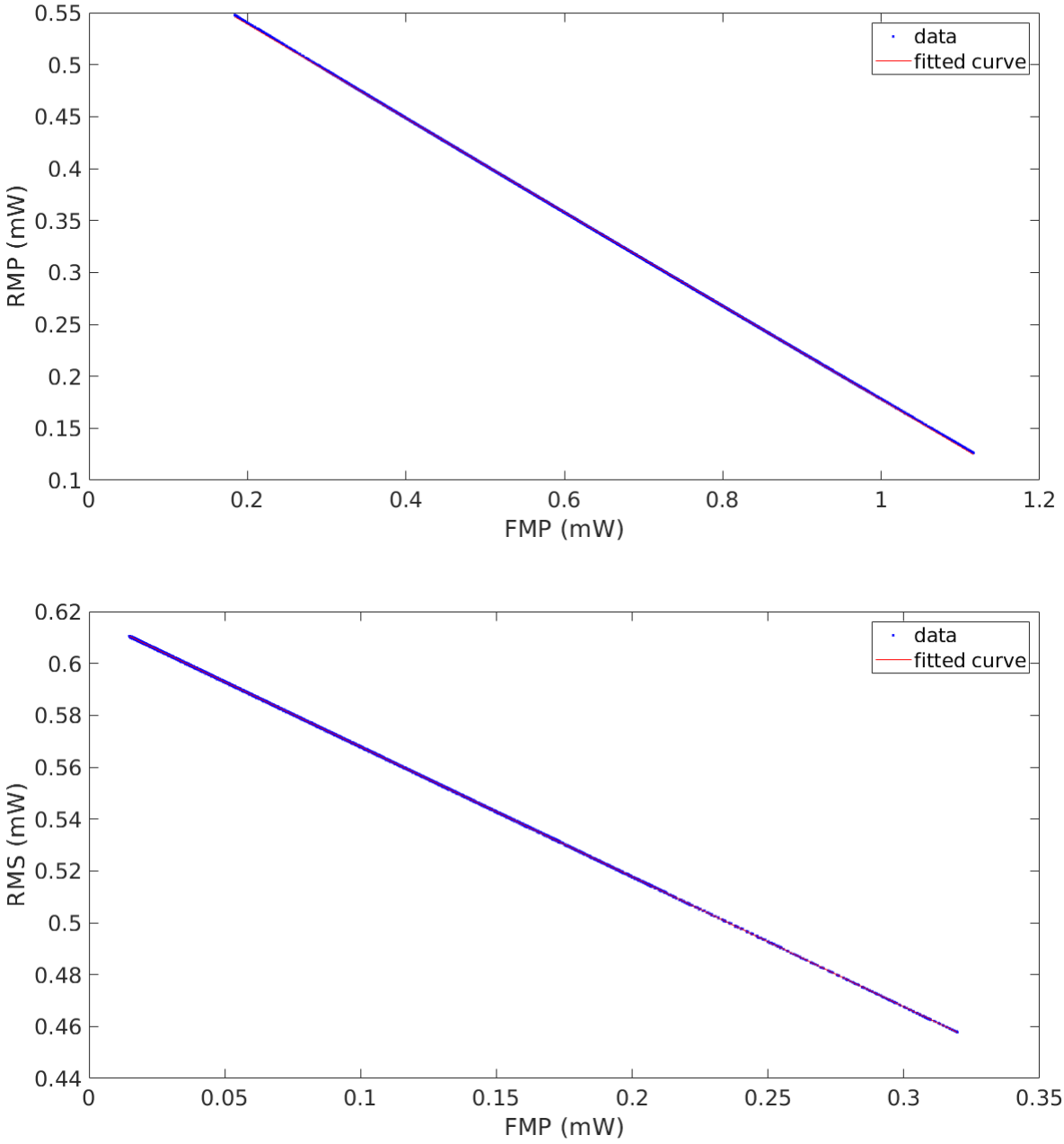

Figure 5.15: (above) Plot of $(y, x) = (RMP(t), FMP(t))$. The linear fit gives $k_p = 0.4518 \pm 0.0005$. (below) Plot of $(y, x) = (RMS(t), FMS(t))$. The linear fit gives $k_s = 0.5010 \pm 0.0002$.

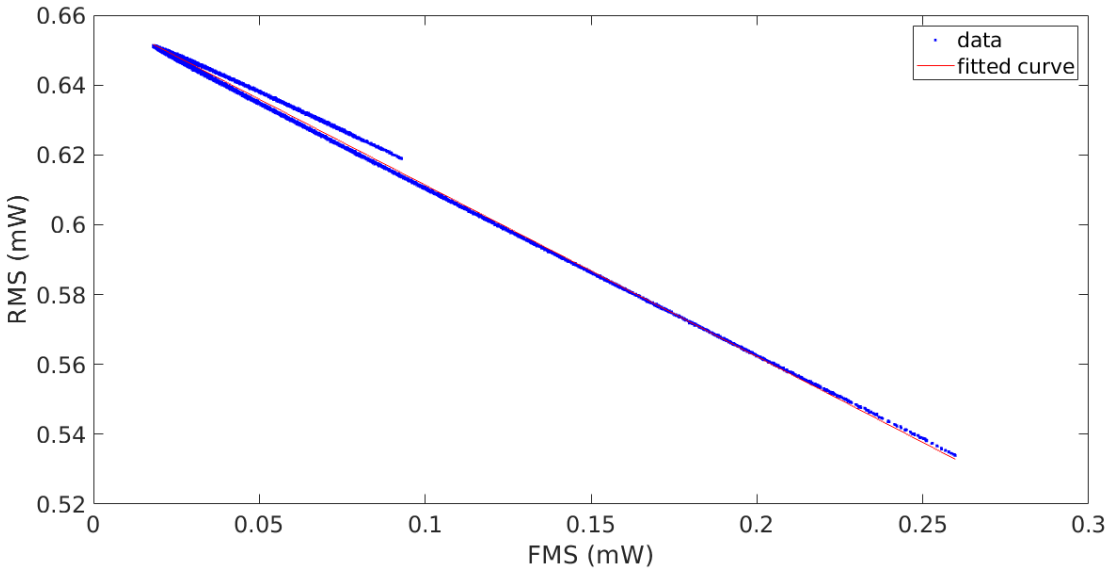

Figure 5.16: Plot of RMS versus FMS when the polarizers still were not added to the outputs. Instead of the straight line expected from theory, the result is a narrow ellipse.

The plot $(y, x) = (sin(\phi), cos(\phi))$ is reported in figure 5.17:

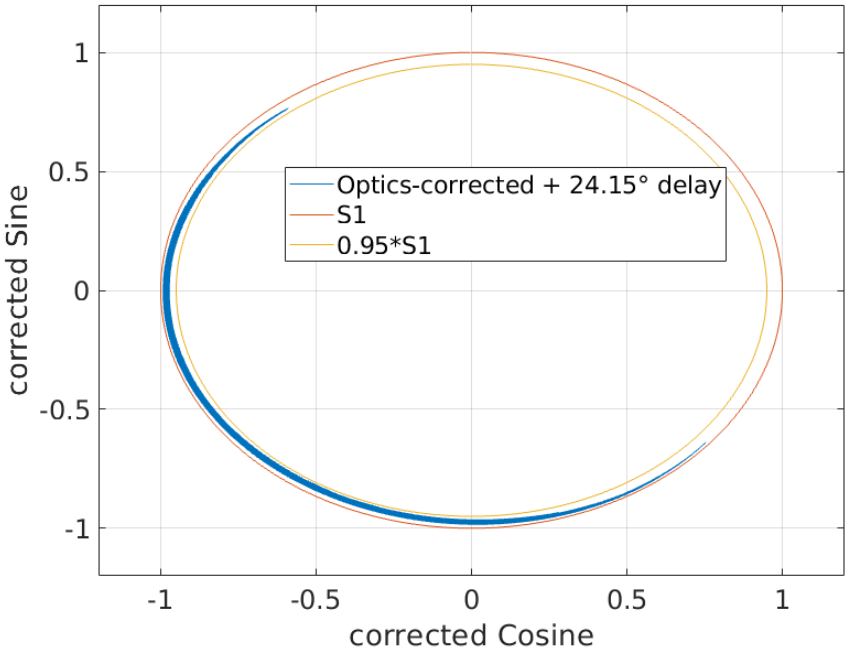

Figure 5.17: Plot of $(y, x) = (sin(\phi(t)), cos(\phi(t)))$. The $\hat{s}$ signal has been shifted of a 24.15° angle using equation (4.1). This plot can be compared with an unitary radius circle indicated by S1 and a 0.95 radius circle indicated by 0.95*S1.

We then report the computed relative displacement PSD, which also proved to have a lower noise level than the spectrum computed from the 3PDR, probably due to a better visibility fluctuation rejection. A 4-hour long sample was measured to achieve better resolution and more averages. The 4PDR measured spectrum is reported in figure 5.18.

The noise level in the spectra measured with the 4PDR is at the level of $3 \cdot 10^{-15} m/\sqrt{Hz}$ above $1000 Hz$, and is close to the noise from the ADC. In the $200 - 700 Hz$ frequency band the noise level is again lower using the 4PDR. In the $80 - 200 Hz$ frequency band noise is lower with the 3PDR, due to ha mechanical mode transient affecting the 4PDR measurement.

Using the 4PDR readout, a 500 seconds long measurement was performed closing the valve and turning the vacuum pumps off. The vacuum tubes to the chamber (shown in figure 5.6) were also disconnected. We report the measured spectra in figure 5.18(below):

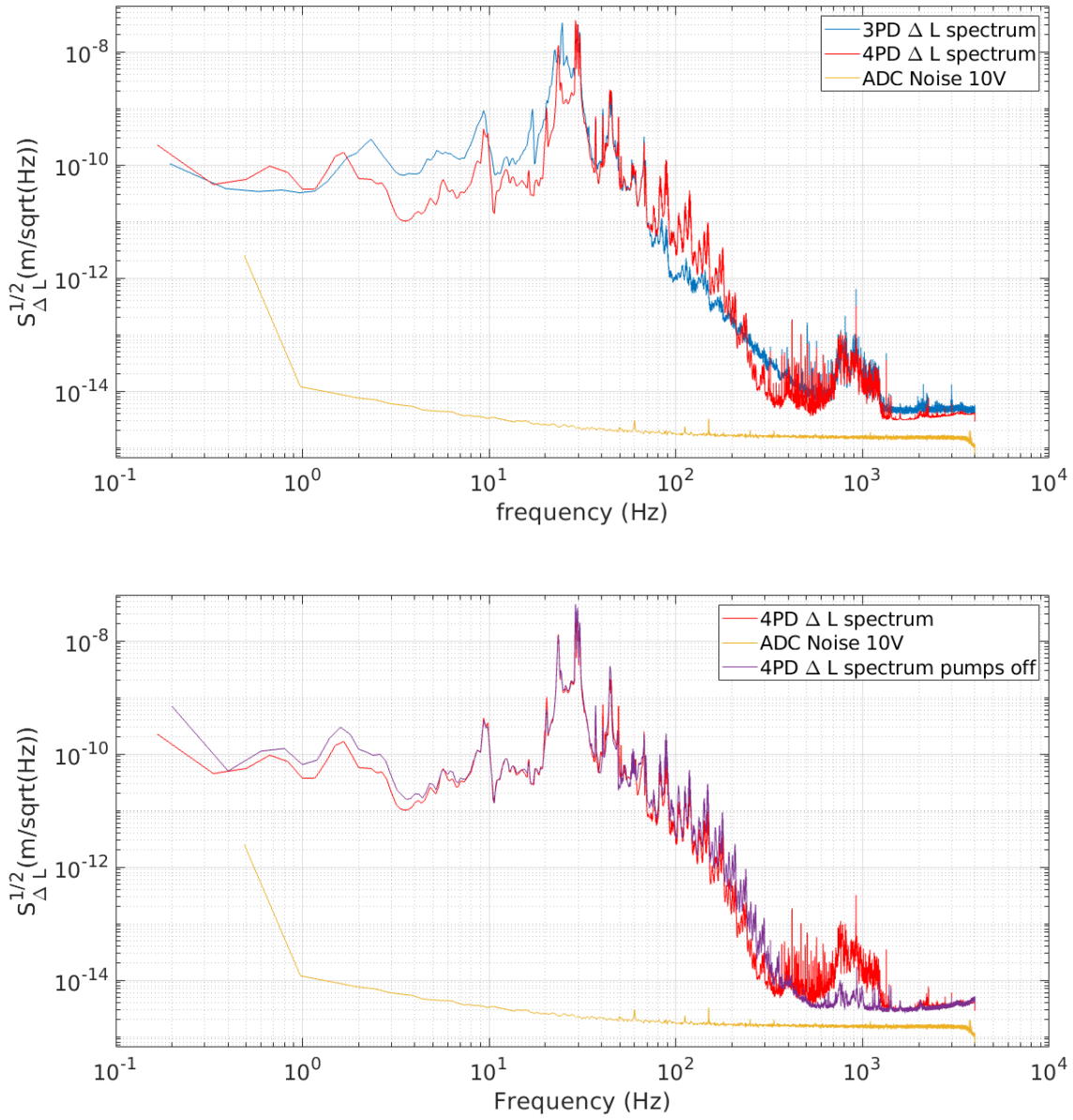

Figure 5.18: Above: (blue) Square root of the time averaged PSD of $\Delta L(t)$ measured with the 4PDR from a 4 hours long sample with a $0.18Hz$ resolution. (red) Square root of the time averaged PSD of $\Delta L(t)$ measured with the 3PDR also shown in figure 5.12. (yellow) The displacement noise caused by the ADC reported in figure 5.9. Below: (red) same spectrum as the red one above in this figure. (purple) Square root of the PSD of $\Delta L(t)$ measured with the 4PDR and vacuum pumps off with 0.5Hz frequency resolution. (yellow) same spectrum as the yellow one above in this figure.

The noise induced by the vacuum pumping system is causing the structures in the $350 - 1350Hz$ frequency band visible in the spectrum. The best measured spectrum is the spectrum with pumps off in figure 5.18. The spectrum is dominated by residual mechanical noise in low frequencies ($< 200Hz$), where the noise consists in a high structure at $29Hz$ and in its superior harmonics (probably due to a non linearity in the system) which gradually decrease in amplitude. At higher frequencies noise is probably dominated by the ADC noise.

Because of the better performance, all the measurements from here on were made using the 4PDR.

5.5 Measurement of the Heated Oscillator

We finally tested the interferometer to see if during the heating transients it is able to achieve the same sensitivity reached in the steady states measurements and if the total measured elongation of the arm's length corresponded to that computed using the aluminum's thermal expansion coefficient. We heated the cuboid mass of the oscillator giving a $2.5V$ supply to the heater, and hence a $9W$ power was hitting the cuboid mass. The oscillator was heated for a 5 hour time. We then started to measure the interferometer's signal, and turned off the heater 10 minutes later so that the oscillator cooled down and it's length reverted back to it's room temperature length.

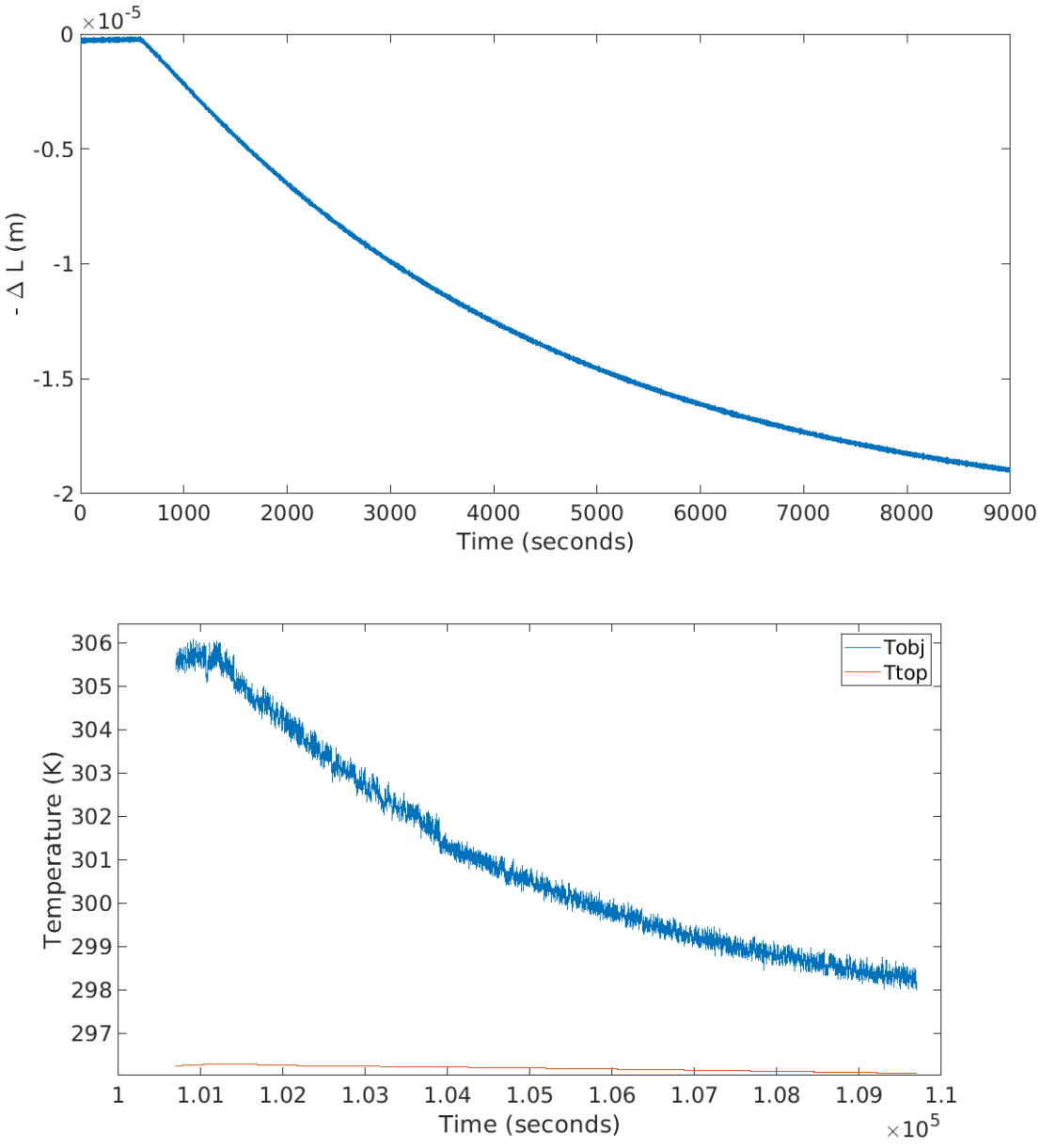

Figure 5.19: Above: $\Delta L(t)$ measured by the interferometer during the cool down. Below: (blue) cuboid mass temperature $T_2(t)$ measured by the thermopile. (red) temperature at the top $T_1(t)$ of the rod measured by the NTC thermometer.

The outputs of the interferometer and temperature measurements are shown in figure 5.19. The maximum temperature difference $\Delta T = T_2 - T_1$ was $8.8K$, while at the end of the

measurement the temperature difference was $1.7K$ We modeled the oscillator's temperature as if the cuboid mass had an uniform temperature T_2 and the rod had an uniform temperature gradient $\Delta T/L$ where L is the rod's length. This model would predict a $17.7\mu m$ elongation of the oscillator, while the elongation measured by the interferometer was of $16.9\mu m$. These two results are consistent considering how we have approximated the temperature profile of the oscillator. A total of 34 fringe crossings hence happened during the measurement.

We report in figure 5.20 some of the spectra computed using the $\Delta L(t)$ data measured during the cooldown transient. The noise level did not change, and was not affected by the 34 fringe crossings that happened during the measurement. The readout hence achieved the scope it was designed for.

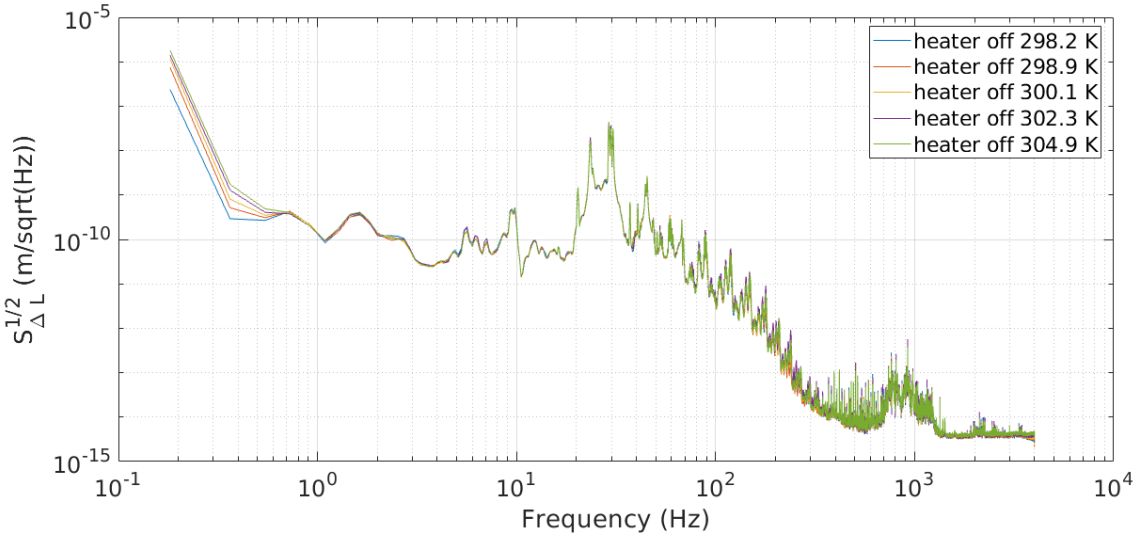

Figure 5.20: Plot of five spectra taken from a 10 minute long acquisition during the oscillator's cooldown. The legend shows the average temperature of the cuboid mass during the sample the PSD was computed from. The sensitivity during the transient is the same as in figure 5.18, with a noise level of $3 \cdot 10^{-15} m/\sqrt{Hz}$ at $1400Hz$.

5.6 Oscillator Modes' Peaks

Investigation of the thermal noise out of equilibrium falls out of the scope of this work, which was aimed at developing the interferometric readout. However, after reaching a sufficient sensitivity, we looked for the oscillator's modes on the spectra (see figure 2.2 for a description of the modes). The longitudinal mode at $\sim 1400Hz$ is detected by the interferometer according to its working principle, since it consists a displacement of mirror 2 in a direction parallel to the path of the beam. The transverse mode at $\sim 320Hz$ couples instead because of an unwanted, or at least uncalibrated, cross-talk. The mode is in fact described by the torsion angle, and the interferometer sees the angular displacement multiplied for the distance between where the beam is hitting the oscillator and the rotation pole, which we have not carefully controlled. Hence the amplitude information from the transverse mode cannot be used in quantitative considerations. The two mode's peaks are expected to have a high quality factor ($\sim 10^3$) because of the material the oscillator is made with, and are expected to decrease their resonance frequency with rising temperature, since the aluminum's stiffness decreases with temperature.

We used this last information to search for the longitudinal mode's peak around $1400Hz$ in the cooldown measurement. In figure 5.21 we report a zoom of figure 5.20 in the area where the longitudinal mode is expected to appear.

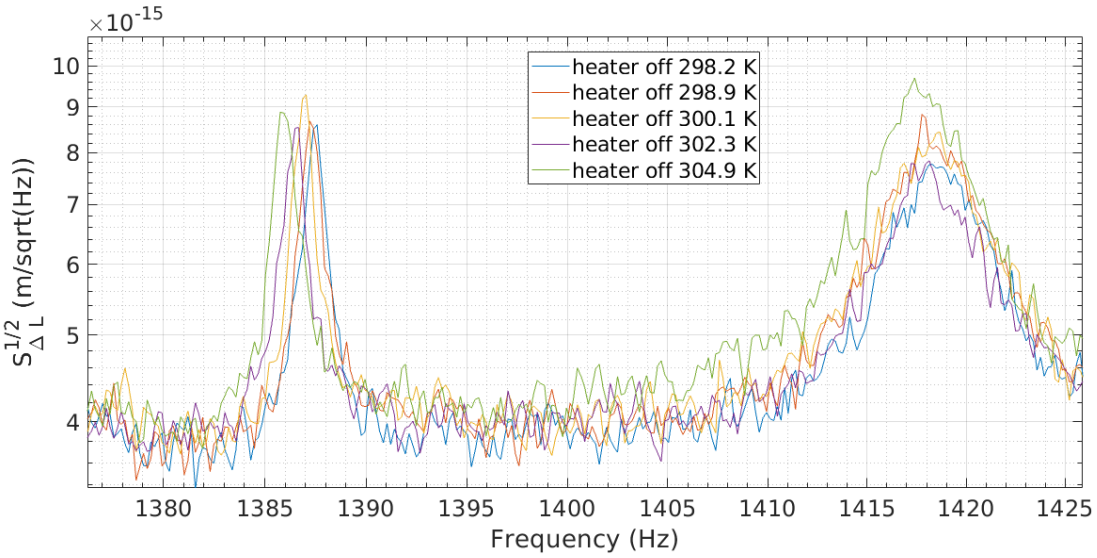

Figure 5.21: Zoom of figure 5.20 around $1400Hz$. The shown spectra were acquired ad various temperatures of the cuboid mass, which are reported in the legend.

We found two peaks: a wide peak at $1418Hz$ and a narrow peak at $1388Hz$. Only the narrow peak at $1388Hz$ appears to change its resonance frequency with temperature, and is behaving in the expected way, increasing it's resonance frequency while temperature decreases; it also shows a high quality factor. On the other hand, the dependence on temperature of the frequency of the peak at 1420 Hz is not clear, and its much lower Q suggests that it is probably not an oscillator mode. Pending further checks, we thus assume the peak at 1388 Hz to correspond to the longitudinal mode, while we have not yet investigated the source of the 1420Hz peak. In figure 5.22 we report the variation of the resonance frequency of the mode with the temperature of the cuboid mass for the longitudinal mode during the cooling transient. The variation of the resonance frequency with temperature is expected to be quadratic, but, since the explored region was small, a linear fit has been performed. We

found that the longitudinal mode's resonance frequency decreases by approximately of $1Hz$ when the cuboid mass's temperature increases by $4K$.

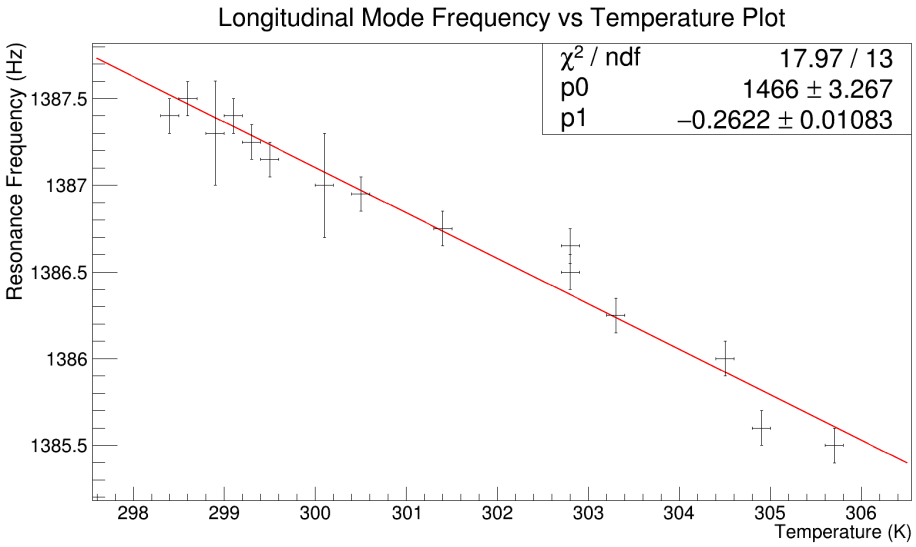

Figure 5.22: Fit of the variation of the resonance frequency with the cuboid mass's temperature.

Using the data of the 4-hour-run we computed a spectrum with high frequency resolution. THe peak was fitted using the laurentian function in equation 2.9 and the result is reported in figure 5.23.

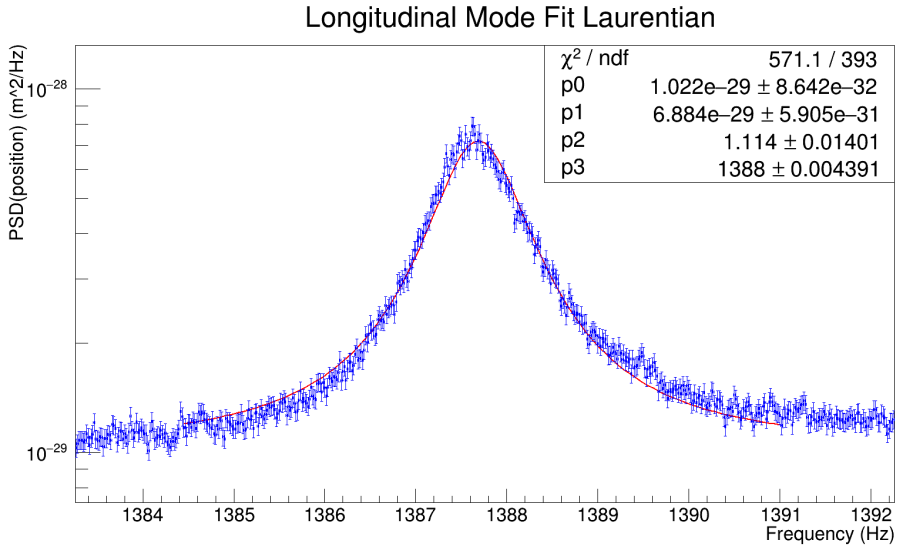

Figure 5.23: Fit of the peak at $1388Hz$ using function 2.9. The used spectrum was averaged 300 times and has a $0.0167Hz$ frequency resolution. The fitted laurentian function is missing the resonance frequency's estimation, probably due to a wrong modeling of the noise. The resulting quality factor of the mode is $Q_l = 1245$.

The resulting fit parameters are reported in table 5.1

The temperature of the mode can be straightforward calculated using equation 2.10

parameter name	symbol	value
readout noise (m^2/Hz)	p_0	1.022e-29 ± 9e-32
peak area$\times\frac{2}{\pi}$ (m^2)	p_1	6.884e-29 ± 6e-31
FWHM (Hz)	p_2	1.14 ± 0.01
resonance frequency (Hz)	p_3	1387.693 ± 0.004

Table 5.1: Resulting parameters of the laurentian fit (equation 2.9 reported in figure 5.23.

resulting in

$$T_{eff,l} = 2\pi p_1 \frac{2}{\pi}(2\pi p_3)^2 k_B^{-1} = (347.8 \pm 0.3)K \tag{5.7}$$

The excess with respect to room temperature is probably due to residual external mechanical excitation of the peak. We hence report in figure 5.24 a detail of figure 5.18(below) which shows that the pumping system is exciting the longitudinal mode, since the area and the height of the peak decreased in the spectrum with pumps off. The need for a vibration-free pumping system is an open issue of the experiment.

A laurentan fit has been performed on the longitudinal mode as in figure 5.23 using the data measured with the vacuum pumps turned off reported in figure 5.24(above). The resulting fit parameters are reported in table 5.2

parameter name	symbol	value
readout noise (m^2/Hz)	p_0	8.767e-30 ± 1e-31
peak area$\times\frac{2}{\pi}$ (m^2)	p_1	6.241e-29 ± 2e-30
FWHM (Hz)	p_2	1.07 ± 0.06
resonance frequency (Hz)	p_3	1387.68 ± 0.03

Table 5.2: Resulting parameters of the laurentian fit (equation 2.9) reported in figure 5.24(below).

The resulting temperature of the longitudinal mode from the fit in figure 5.24 is $(321.5 \pm 10)K$, and the result is compatible with the room's temperature, stating that the peak's area was compatible with that expected by thermal noise excitation, and that the readout is sensitive enouth to detect the thermal noise excitation caused by thermal noise.

We searched also for the transverse mode's peak with the same method. In figure 5.26(above) we report a detail of figure 5.20. The zoomed region is dominated by noise. Noise structures show peaks at the same frequencies in the 5 spectra. A narrow peak hardly stands over the noise and has the expected behavior of frequency vs temperature. The plot of the transverse mode's resonance frequency vs the cuboid mass's temperature is reported in figure 5.26(below). Again, the expected relation is quadratic, but a linear fit was performed since the temperature variation was small. The resonance frequency of the transverse mode has a smaller dependence on the cuboid mass's temperature with respect to what happens with the transverse mode.

We then fitted the peak using the equilibrium data using the curve expected from internal damping (equation 2.7), since the laurentian function 2.9 did not fit the data. The used function for the internal damping fit is (5.8):

$$\left\langle x^2(\omega)\right\rangle = \frac{4k_BT}{m\omega}\frac{\omega_0^2\phi(\omega)}{(\omega^2-\omega_0^2)^2+\omega_0^4\phi(\omega)^2} \rightarrow y(\nu) = p0 + \frac{p_1 p_2 p_3^2}{\nu((\nu^2-p_3^2)^2+p_3^4 p_2^2)} \tag{5.8}$$

where a parameter p_0 has been added to estimate the readout noise approximated as a constant, $p_1 = \frac{4k_BT}{m}$ where T is the absolute temperature, $k_B = 1.38 \cdot 10^{-23} kg\, s^{-2} m^2 K^{-1}$ is

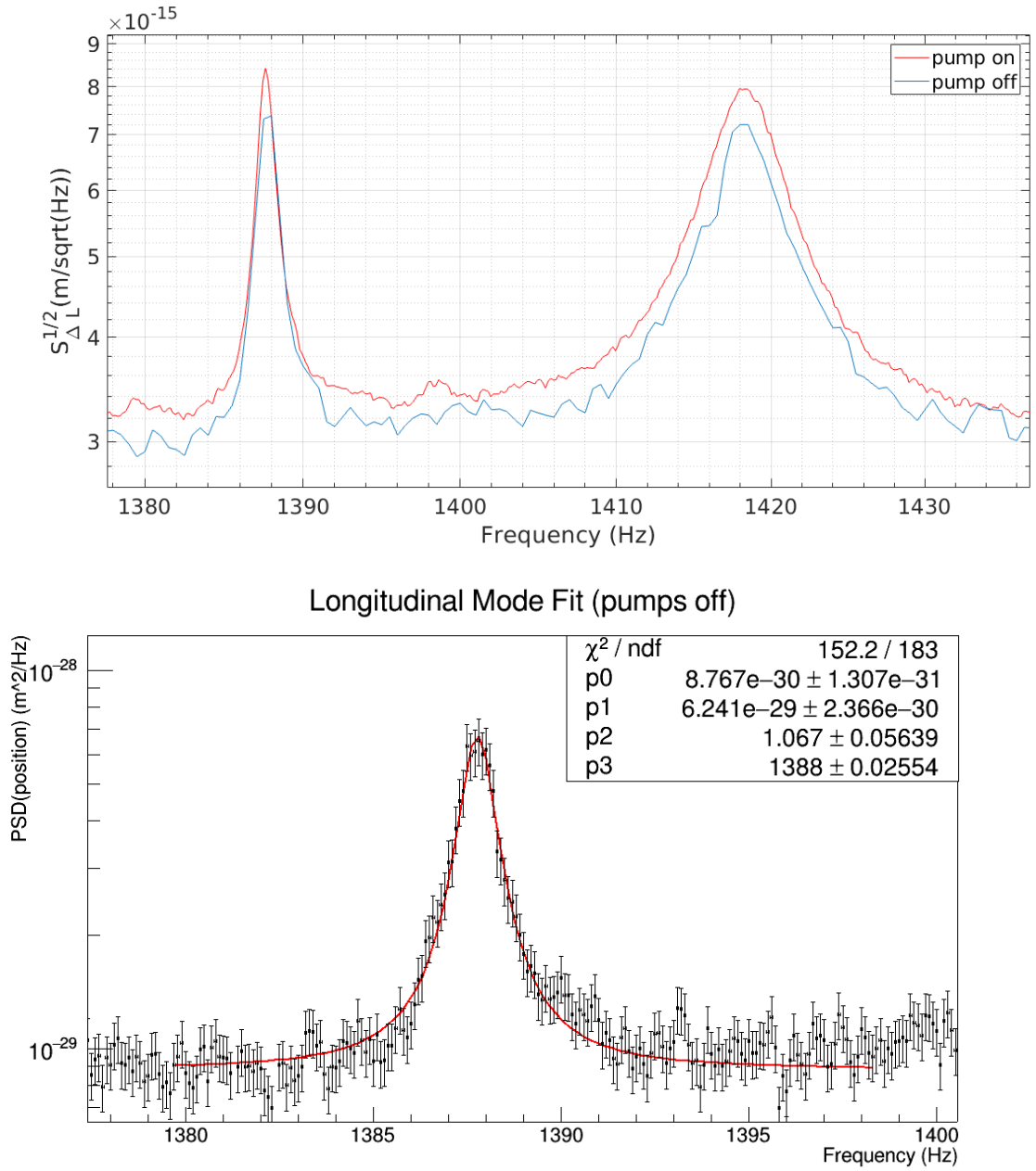

Figure 5.24: (Above) Zoom of figure 5.18(below) around the candidate transverse mode peaks. (Below) Fit of the longitudinal mode with the vacuum pumps off using the same data used to compute the spectrum in figure 5.18(below).

Boltzmann's constant and $m = 0.234kg$ [13] is the mode's mass, which is assumed to be half of the rod's mass plus the cuboid's mass, $p_2 = \phi(\nu_0) = 1/Q$ and $p_3 = \nu_0$ is the resonance frequency.

The fit using equation 5.8 is reported in figure 5.26

As said, the temperature cannot be inferred from the transverse mode. Using the information from the fit with the internal damping equation 5.8, we calculated the quality factor $Q_t = 12200 \pm 500$.

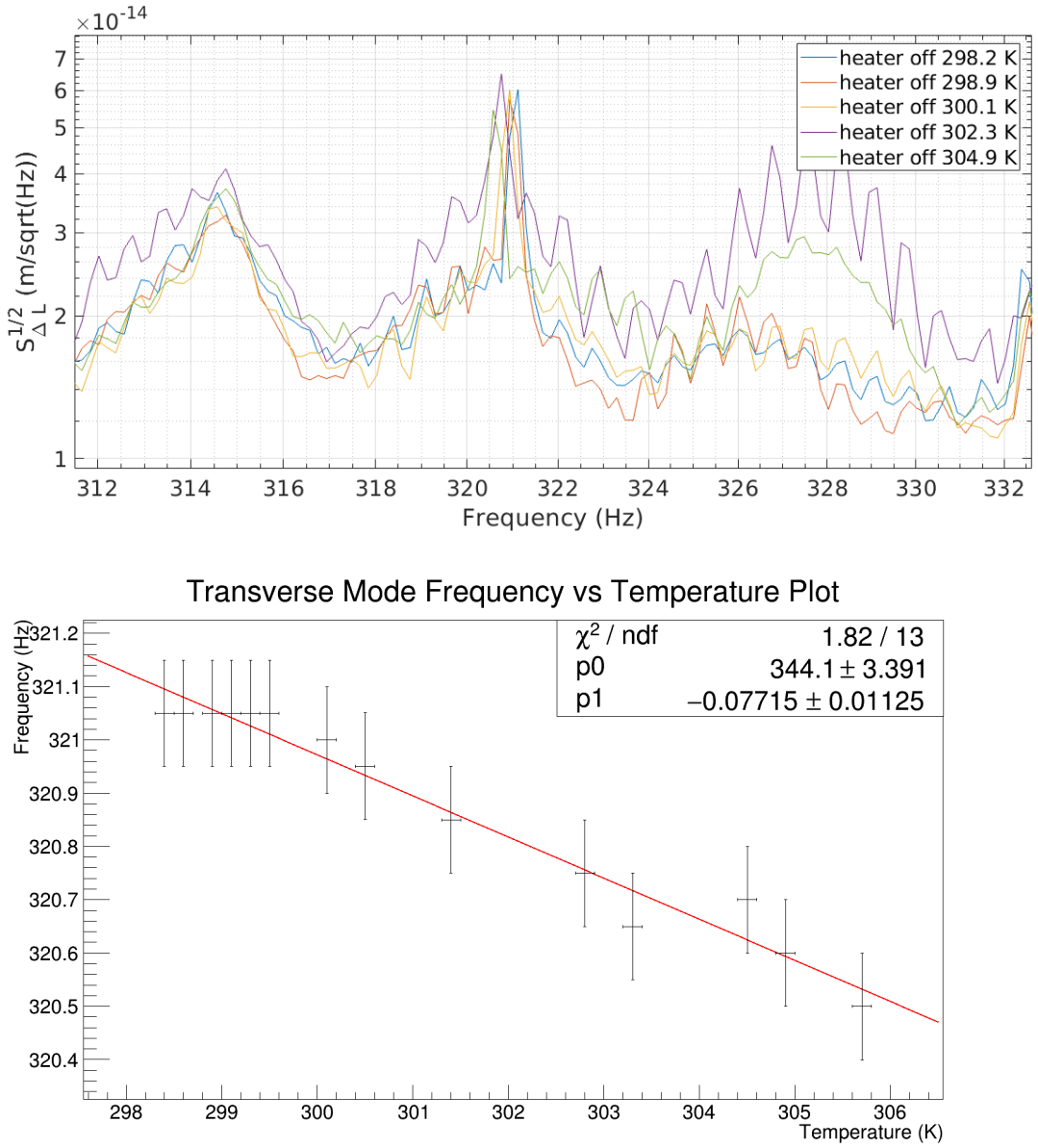

Figure 5.25: Above: zoom on figure 5.20 around $300Hz$ where the peak of the transverse mode is espected to be. Below: fit of the relation between temperature and resonance frequency for the transverse mode.

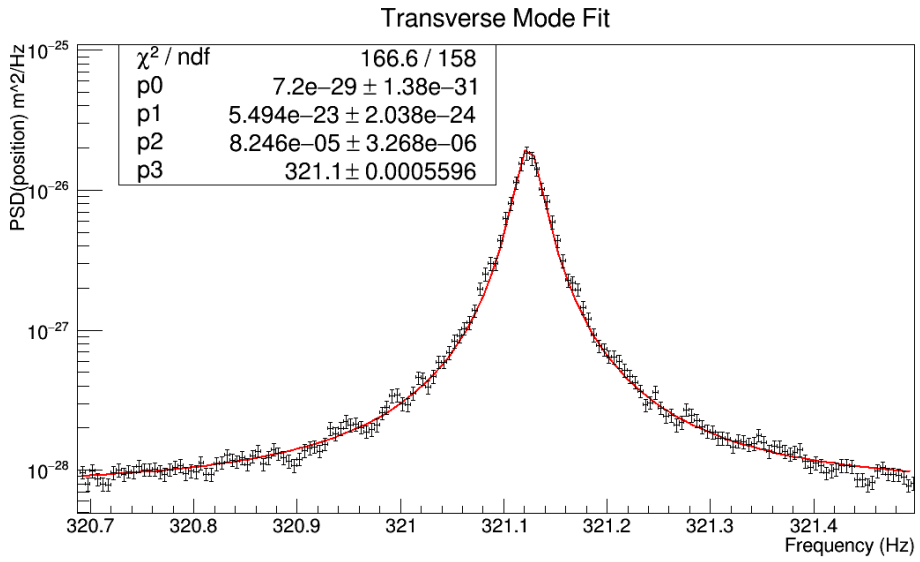

Figure 5.26: Fit of the transverse mode's peak using a the internal damping equation 5.8.

5.7 Future Improvements

The readout is probably limited by the ADC noise (see figure 5.9), which is limiting the ΔL sensitivity at about $1.5 \cdot 10^{-15} m/\sqrt{Hz}$. To increase the sensitivity the ADC range should be reduced. The lower ADC range is at $\pm 3.16V$ and has a noise level of $2 \cdot 10^{-8} V/sqrtHz$, which is slightly lower than the noise from the photodiodes (see section 5.2) and anyhow lower than the expected shot noise of the 2mW laser beam. Being able to reduce the acquisition range (maintaining the same beam intensity) would bring the readout to be limited by shot noise at a level of $8.2 \cdot 10^{-15} m/\sqrt{Hz}$. Shot noise cannot be reduced since the photodiodes saturate at $2mW$.

The most straightforward way to lower to $\pm 3.16V$ the ADC range would be to decrease the beam's intensity. The beam intensity should be lowered to $0.6mW$ but doing so the shot noise would overcome the current ADC noise level.

Another solution which is worth to investigate is the realization of a high pass filter with transfer function $T(\omega)$, capable of suppressing at least by a factor 3 the amplitude of the signal under $\sim 200Hz$. The voltage signal from the photodiodes $PD(t)$ lies in the range $[0; -10]V$ with a 2mW beam, and therefore needs to be acquired in the $\pm 10V$ ADC range, but the $10V$ intensity variations that constrain us to the chosen ADC range happen at a frequency lower than $50Hz$ as visible from the measured spectra in sections 5.3 and 5.4. By adding one of these filters after each acquired photodiode, the ADC would measure $T \cdot PD(t)$ in the $\pm 3.16V$ ADC range. During the analysis the signal would me multiplied by T^{-1} and the ADC noise's contribution would be lowered, taking the noise limit to that set by the $2mW$ shot noise at $8.2 \cdot 10^{-15} m/\sqrt{Hz}$.

The setup also needs a vibration free vacuum pump to lower mechanical noise in the $300 - 1350Hz$ frequency band.

Conclusions

During this thesis an interferometric readout has been built with the aim to detect the vibrations induced by thermal noise on a metallic oscillator. The readout needs to reach a sensitivity comparable to that of the previously used capacitive readout which was $\sim 3 \cdot 10^{-13} m/\sqrt{Hz}$ at a $300 Hz$ and $2 \cdot 10^{-15} m/\sqrt{Hz}$ at $1400 Hz$. The readout needs to maintain the sensitivity also during the same heating transients, when the oscillator's length will incrase of several μm. Self-calibration is also requested.

Quadrature homodyne interferometery has been implemented and tested. The interferometer has been built and characterized in sensitivity and calibration. Various measurements procedures and signal extraction algorithms have been studied. We found out that in order to achieve the best sensitivity, all of the 4 outputs from the interferometer need to be acquired. The achieved sensitivity was $3 \cdot 10^{-15} m/\sqrt{Hz}$ at $1400 Hz$. The performance was maintained during the heating transients of the oscillator. As expected the interferometer is self calibrated and the noise is not affected by fringe crossing

We finally looked for the oscillator's modes on the spectra, which have been found and characterized. They seem to be slightly above the thermal noise, problably excited by pumps.

The sensitivity seems to be limited at high frequencies by the noise from the ADC. We also propose a method to improve the sensitivity by whitening the photodiodes'output before acquisition so to better expoloit the dynamic range of the ADC.

The experiment is hence ready to perform the nonequilibrium measurements once a vibration-free pump has been added.

Appendix A

Power Spectral Density

In a formal definition, the Power Spectral Density (PSD) is the *Fourier transform of the auto-correlation function* $R(t,t') = \langle x(t), x(t')\rangle$. If $x(t)$ is a stationary process then $R(t,t') = R(\tau = t, t')$ and the PSD is defined as

$$S_{xx}(\omega) = \int_{-\infty}^{+\infty} d\tau R(\tau) e^{i\omega\tau} \tag{A.1}$$

The physical meaning of the PSD of a signal is the power density in the frequency space: if a filter is letting through only frequencies between ω_1 and ω_2, then the total output power would be

$$P_{\omega_1,\omega_2} = \int_{\omega_1}^{\omega_2} S_{xx}(\omega) d\omega \tag{A.2}$$

By definition, since the auto-correlation function is real, $S_{xx}(\omega) = S_{xx}(-\omega)$, hence the one-sided PSD is usually defined as $D_{xx}(\omega) = 2S_{xx}(\omega)$ for $\omega > 0$. The variance of the signal is the integral of the PSD in the frequency domain: $\sigma^2 = \int_0^\infty S(\omega) d\omega$.

The PSD computation would need a data set of infinite duration, while on the other hand measurements can be performed only on a finite amount of time T. In this case the data will have only Fourier components at $f_n = \frac{n}{T}$, and the frequency resolution is then $\Delta f = \frac{1}{T}$.

Finally, Nyquist theorem states that a signal can be sampled and correctly reconstructed only if its frequency content is such that $f_{max} < \frac{f_s}{2} = \frac{1}{2t_s}$, and since the data acquisition in my experiment is sampling at 8 kHz, the spectra I show never overcome the 4 kHz limit.

If one computes the correlation function between two different variables $x(t)$ and $y(t)$, its fourier transform is named *cross power spectral density* (CPSD):

$$C(\tau = t, t') = \langle x(t), y(t')\rangle \rightarrow S_{xy}(\omega) = \int_{-\infty}^{+\infty} d\tau C(\tau) e^{i\omega\tau} \tag{A.3}$$

Unlikely the PSD, CPSD is not real. From CPSD, the *magnitude square coherence* (MSC) is defined as

$$M(\omega) = \frac{S_{xy}}{S_{xx}^{\frac{1}{2}} S_{yy}^{\frac{1}{2}}}(\omega) \tag{A.4}$$

which lies the interval $[0, 1]$ and represents the correlation of the two signals in each frequency band. The imaginary part of the CPSD represents the phase lag between the two signals $x(t)$ and $y(t)$. For physical reasons, $\Im[CPSD](\omega)$ must be a smooth function of the frequency ω in order for the CPSD to represent a credible correlation.

Appendix B

Phase Unwrapping

An interferometer's output, as shown in equation 1.16, is a periodic function with period $\frac{\lambda}{4}$ of the relative position of the two mirrors $\Delta L(t)$. The atan2 computation is useful because its output has a 2π period and hence twice the usual atan's period, but the problem is not solved.

The problem of periodicity unwrapping can be thought the problem of counting how many times a point of coordinates $(y, x) = (sin(\varphi), cos(\varphi))$ turns around the origin of the y-x plane using an atan computation. If φ increases (or decreases) monotonically, the point turns around the origin, but an atan computation cannot count how many revolutions the point has completed, since it gives out just the angle formed by the line joining the point to the origin and the x-axis.

On the other hand, the atan2 is a monotone function, and hence discontinuities arise when the point completes a revolution. The unwrapping is the procedure which finds these discontinuities and removes them 'counting' the point's revolutions. For example, in the case of quadrature interferometry, if the phase φ is such that the computed phase $\phi = atan2(sin(\varphi), cos(\varphi)) = \pi - \delta$ with $\delta > 0$, and the mirrors move in order to make φ increase of 2δ, $\varphi = 2k\Delta L \rightarrow 2k\Delta L' = \varphi' = \varphi + 2\delta$, then new computed phase would be $\phi' = atan2(sin(\varphi'), cos(\varphi')) = -\pi + \delta$ and not $\pi + \delta$ as the continuity of the motion suggests. If one had to compute the relative mirror's position as $\Delta L = \phi\frac{\lambda}{4\pi}$ this would mean that the mirror has suddenly moved back of a distance $\sim \lambda/2$ (if δ is sufficiently small).

The unwrapping algorithm we used can be summarized as follows. If in a time series (as $\phi(t)$ is) a computed phase value $\phi(i)$ differs from the previous one $\phi(i-1)$ by less than $-\pi \rightarrow \phi(i) - \phi(i-1) < -\pi)$ (or more than $\pi \rightarrow \phi(i) - \phi(i-1) > \pi$), to that computed phase value and to all the following ones a 2π phase quantity is added (subtracted). This procedure goes on for each discontinuity in the time series.

Of course the result of this algorithm depends on the time series it is applied to: it cannot be applied to an angle time series where the noise's amplitude is comparable with π, because noise would be confused with the searched discontinuities. Even in low noise signals, the phase difference between each couple of consecutive points must anyway be much smaller than π, otherwise wrong fringe crossings would be counted: one can check that this statement translates in a constrain on how the sampling frequency (f_s) relates to the maximum expected time derivative of the differential lenght $\Delta L(t)$:

$$\phi(i) - \phi(i+1) << \pi \rightarrow \frac{4\pi}{\lambda}(\Delta L(i) - \Delta L(i+1) << \pi \approx \frac{d}{dt}(\Delta L) f_s^{-1} << \frac{\lambda}{4} \qquad \text{(B.1)}$$

so the sampling frequency must be such that $f_s > 4\frac{d}{dt}(\Delta L)\lambda^{-1}$. [25]

Figure B.1 shows the reconstructed phase computation starting from two generic $sin(\varphi(t))$ and $cos(\varphi(t))$ time series using (above) atan2 with and without unwrapping and (below) a single sine or cosine signal (a simple homodyne interferometer), computing the phase as $acos(cos(\varphi(t)))$ and $asin(sin(\varphi(t)))$.

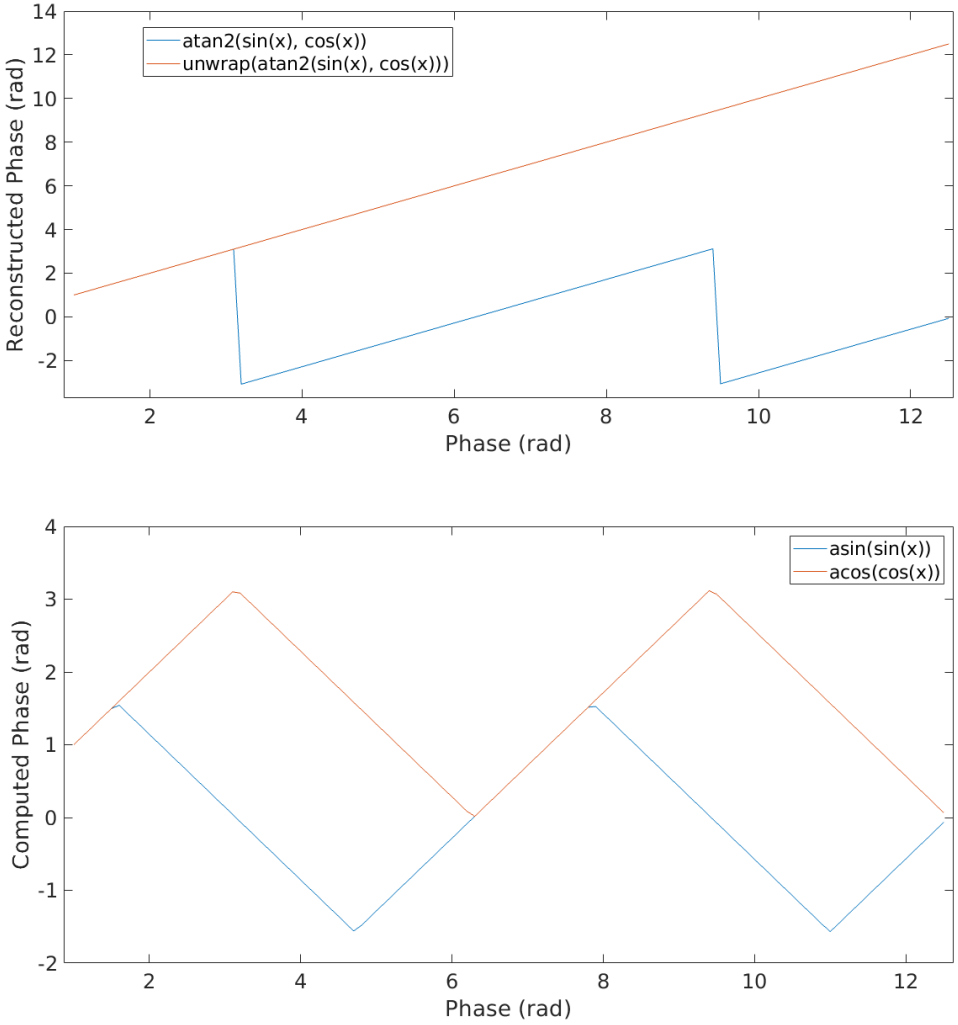

Figure B.1: Above: Example of simple atan2 computation and unwrapped atan2 computation. In this plot, the blue line is (y,x) = (atan2(sin(x), cos(x)) , x) (the *computed phase*) with $x \in [0, 4\pi]$, while the red line is (y,x) = (unwrap(atan2(sin(x), cos(x))), x) (the *unwrapped phase*) always with $x \in [0, 4\pi]$. The result of the simple atan2 computation lies in the range $[-\pi, \pi]$, and is a monotone function of the phase x in the atan2's codomain. The discontinuities are evident in $x = \pi, 3\pi$. The unwrapping algorithm removes the discontinuities adding multiples of 2π. The resulting unwrapped phase (y) is then equal to the original phase (x). Below: Examples of asin ad acos computations starting from a single signal. The blue line is (y, x) = (acos(cos(x)), x) and the red line is (y, x) = (asin (sin (x)), x) with $x \in [0, 4\pi]$. Since the slope changes sign during one period, this operation is not able to compute the motion. For example, let $\phi(t)$ be the computed phase and $\varphi(t) = 2k\Delta L(t)$ the original phase. If I had to measure $\dot{\phi}(t) > 0$, I would not be able to distinguish if both $\frac{d}{d\varphi}(acos(cos(\varphi)) > 0$ and $\dot{\varphi} < 0$ or $\frac{d}{d\varphi}(acos(cos(\varphi)) < 0$ and $\dot{\varphi} > 0$. The same happens with the sine case. Since no discontinuities are evident here (they manifest on the first derivative) no direct unwrapping algorithm exists. This does not happen in the atan2 computation.

Appendix C

Gaussian Beams

For a detailed description of gaussian laser beams see [24]. A laser beam is an electromagnetic field propagating in space. Since the magnetic field mimics the electric field's behavior, only one of the two needs to be described, and the electric field is traditionally chosen. A beam propagating along the z axis can be formalized as

$$E(x, y, z) = u(x, y, z)e^{-ikz} \tag{C.1}$$

where $E(x, y, z)$ is the scalar electric field, $u(x, y, z)$ is the complex amplitude and e^{ikz} is the oscillatory term, k is the wave-number $k = \frac{2\pi}{\lambda} = \frac{\omega}{c}$. The temporal oscillation $e^{i\omega t}$ is neglected. From Maxwell's equations we know that the electric field obeys the equation

$$(\nabla^2 + k^2)E(x, y, z) = 0 \tag{C.2}$$

If the anghe between the versors normal to the wavefronts (the 2-dimensional varieties where the argument of the exponential are constant ($-ikz = const$) and the beam's propagation direction is small, the *paraxial* approximation can be introduced. Equation C.2 can be approximated into

$$\frac{\partial^2 u}{\partial x^2} + \frac{\partial^2 u}{\partial y^2} - 2ik\frac{\partial u}{\partial z} = 0 \tag{C.3}$$

assuming

$$\left|\frac{\partial^2 u}{\partial z^2}\right| << \left|2k\frac{\partial u}{\partial z}\right|, \left|\frac{\partial^2 u}{\partial x^2}\right|, \left|\frac{\partial^2 u}{\partial y^2}\right| \tag{C.4}$$

Equation C.3 is often written as

$$\nabla_t^2 u(\mathbf{s}, z) - 2ik\frac{\partial u}{\partial z}(\mathbf{s}, z) = 0 \tag{C.5}$$

where ∇_t^2 is the laplacian relative to the transverse coordinates, and s are the transverse coordinates.

A Gaussian beam is the lowest order solution to the paraxial wave equation C.3:

$$u(x, y, z) = E_0\frac{w_0}{w(z)}e^{-\frac{x^2+y^2}{w^2} - i\left(l\frac{x^2+y^2}{2R(z)} - \psi(z)\right)} \tag{C.6}$$

where $w(z)$ is the beam's size (i.e. the radius where the intensity of the beam decreases by a factor e^{-2}), $R(z)$ is the wavefront's curvature radius, $\psi(z)$ is the Guoy phase (an extra phase

evolution with respect to a plane wave) and z_r is the Rayleigh range, and they are defined as:

$$w(z) = w_0\sqrt{1+\left(\frac{z}{z_r}\right)^2} \quad R(z) = z\left(1+\left(\frac{z}{z_r}\right)^2\right) \quad \psi(z) = atan\left(\frac{z}{z_r}\right) \quad z_r = \frac{\pi w_0^2}{\lambda} \tag{C.7}$$

where w_0 is the beam waist (the minimum beam's size) and λ is the beam's wavelength.

Putting together the first and the last equation from (C.7) one can obtain the beam's profile $W^2(z)$, i.e. the beam's width width as a function of the spatial coordinate z, $W^2(z)$

$$W^2(z) = W_0^2 + \frac{z^2}{W_0^2(\pi/\lambda)^2} \tag{C.8}$$

where the waist is positioned in $z = 0$. This is the relation I used to fit the gaussian beam's profiles in section 4.1. A Gaussian beam's profile is shown in figure C.1:

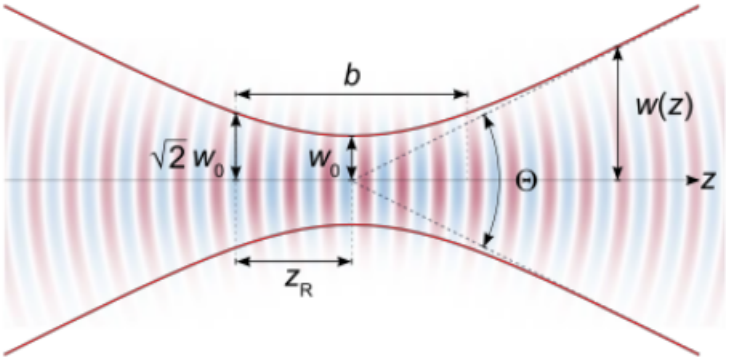

(a) A Gaussian beam's profile along the propagation axis z. (Credits: www.wikipedia.org)

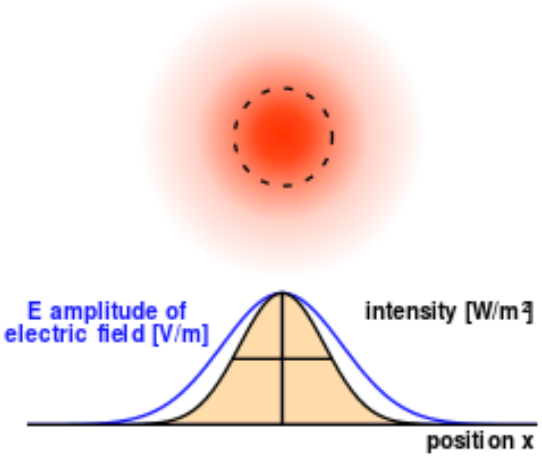

(b) A Gaussian beam's intensity profile. (Credits: www.wikipedia.org)

Figure C.1: A Gaussian beam's profile

Appendix D

Optics Formalism: Jones Calculus

Jones calculus is an easy way to describe the behavior of the electric field of the laser beams and its interaction with polarizers and wave plates, which are a key part of this experiment. I will briefly resume the concepts used in this thesis. A good reference is [26].

This formalism is meant to describe a beam propagating along one axis, let's name it z. The electric field $\vec{E}$ is lies in the plane perpendicular to the propagation direction, which is the 2-dimensional space we are interested to describe. This space then naturally has a canonical basis

$$e_x = \begin{pmatrix} 1 \\ 0 \end{pmatrix} \qquad e_y = \begin{pmatrix} 0 \\ 1 \end{pmatrix} \tag{D.1}$$

which is then identifying the two possible polarizations, respectively $\hat{p}$ and $\hat{s}$. Polarizations are fixed by the optical elements, and each optical element has its polarization eigenbasis, which is formed by the eigenvectors that make the matrix describing it 'diagonal'. From now on the $\hat{p}$ versor will identify an electric field direction perpendicular to the optical bench's surface, while the $\hat{s}$ versor will identify the direction parallel to the optical bench's surface. A generic beam, or electric field, can be written as:

$$\vec{E} = \begin{pmatrix} E_x \\ E_y \end{pmatrix} \tag{D.2}$$

while a $\hat{p}$ polarized beam (in this basis) would have only the e_x component. A generic beam's intensity is given by it's square modulus:

$$I = \begin{pmatrix} E_x \\ E_y \end{pmatrix}^* \cdot \begin{pmatrix} E_x \\ E_y \end{pmatrix} = E_x^* E_x + E_y^* E_y \tag{D.3}$$

A matrix can be associated to each optical element to describe it's effect on the electric field crossing it. The simplest optical element is the polarizer, which projects the electric field on a polarization axis. An ideal linear $\hat{p}$ polarizer and a $\hat{s}$ polarizer are described by the matrices

$$P_x = \begin{pmatrix} 1 & 0 \\ 0 & 0 \end{pmatrix} \qquad P_y = \begin{pmatrix} 0 & 0 \\ 0 & 1 \end{pmatrix} \tag{D.4}$$

Of course optics (as waveplates) may be set on a rotator, and their eigenbasis is hence rotated with respect to the $\hat{p}$ and $\hat{s}$ versors. In this case we can conserve the description of each optical element in its proper eigenbasis basis by applying rotation matrix to the optical

element's matrix. A $\hat{p}$ polarizer at a generic angle θ is then described applying a rotation matrix $R(\theta)$ to the matrix describing the polarizer in its eigenbasis:

$$P(\theta) = R(-\theta)P_x R(\theta) = \begin{pmatrix} cos^2\theta & sin\theta cos\theta \\ sin\theta cos\theta & sin^2\theta \end{pmatrix} \tag{D.5}$$

Of course one can see that a $\hat{s}$ polarizer is just a $\hat{p}$ polarizer rotated by 90°. If a polarizer is applied at a generic angle to a $\hat{p}$ polarized beam, the result is:

$$\vec{E} = \begin{pmatrix} cos^2\theta & sin\theta cos\theta \\ sin\theta cos\theta & sin^2\theta \end{pmatrix} \cdot \begin{pmatrix} E_x \\ 0 \end{pmatrix} = E_x cos\theta \begin{pmatrix} cos\theta \\ sin\theta \end{pmatrix} \tag{D.6}$$

The beam's intensity is then $I = |E|^2 = E_x^2 cos^2(\theta)$, and hence a polarizer is able to extinct a linearly polarize beam.

Wave plates (or phase retarders) have the effect of adding different phases to the $\hat{p}$ and $\hat{s}$ components of the beam that cross them. A matrix describing a wave plate in its eigenbasis is

$$R(\phi_x, \phi_y) = \begin{pmatrix} e^{i\phi_x} & 0 \\ 0 & e^{i\phi_y} \end{pmatrix} \tag{D.7}$$

The effect on the laser beam only accounts for the added phase difference $\phi_x - \phi_y$. For a half-wave plate $\phi_x - \phi_y = \pi$. Half-wave means that the phase delay one polarization gains with respect to the other one is exactly the phase delay that the beam would have gained in a $\frac{\lambda}{2}$ spatial propagation, in fact $\pi = k\frac{\lambda}{2} = \frac{2\pi}{\lambda} \cdot \frac{\lambda}{2}$. For a quarter-wave plate $\phi_x - \phi_y = \frac{\pi}{2}$, and for an octal-wave plate $\phi_x - \phi_y = \frac{\pi}{4}$.

The matrix describing a half-wave plate at a generic angle θ is then

$$R(\phi_x - \phi_y = \pi, \theta) = R(-\theta)R(0, \pi)R(\theta) = \begin{pmatrix} cos2\theta & sin2\theta \\ sin2\theta & cos2\theta \end{pmatrix} \tag{D.8}$$

The effect of a half-wave plate applied at a generic angle to a linearly $\hat{p}$ polarized beam is then

$$\vec{E} = \begin{pmatrix} cos2\theta & sin2\theta \\ sin2\theta & cos2\theta \end{pmatrix} \cdot \begin{pmatrix} E_x \\ 0 \end{pmatrix} = E_x \begin{pmatrix} cos2\theta \\ sin2\theta \end{pmatrix} \tag{D.9}$$

Rotating the half-wave plate's angle, one can change the polarization direction of a linearly polarized incoming beam.

If properly aligned with the incoming beam, quarter-wave plates can obtain a circular polarization starting from a linearly polarized beam, or obtain the inverse effect, as correcting a beam's ellipticity, making it linear. The octal-wave plate is used in our experiment to obtain the same effect of a quarter-wave plate by being crossed twice.

I report now two computations which were useful for the experiment.

Octal-wave plate The matrix describing an octal-wave plate at a generic angle is

$$R(\phi_x = 0, \phi_y = \frac{\pi}{4}, \theta) = \begin{pmatrix} cos^2\theta + e^{i\frac{\pi}{4}} sin^2\theta & (1 - e^{i\frac{\pi}{4}}) cos\theta sin\theta \\ (1 - e^{i\frac{\pi}{4}}) cos\theta sin\theta & sin^2\theta + e^{i\frac{\pi}{4}} cos^2\theta \end{pmatrix} \tag{D.10}$$

By sending a linearly $\hat{p}$ polarized beam to the octal-wave plate in a generic angle θ, and selecting only the $\hat{p}$ component, the output is

$$\begin{aligned} \vec{E} &= \begin{pmatrix} 1 & 0 \\ 0 & 0 \end{pmatrix} \cdot \begin{pmatrix} cos^2\theta + e^{i\frac{\pi}{4}} sin^2\theta & (1 - e^{i\frac{\pi}{4}}) cos\theta sin\theta \\ (1 - e^{i\frac{\pi}{4}}) cos\theta sin\theta & sin^2\theta + e^{i\frac{\pi}{4}} cos^2\theta \end{pmatrix} \cdot \begin{pmatrix} E_x \\ 0 \end{pmatrix} \\ &= E_x(cos^2\theta + e^{i\frac{\pi}{4}} sin^2\theta) \end{aligned} \tag{D.11}$$

The intensity is the square modulus of the electric field:

$$I = I_0 \left(1 - \frac{2-\sqrt{2}}{4} sin^2 2\theta\right) \tag{D.12}$$

where $I_0 = E_x^2$. The transmitted $\hat{p}$ intensity has 4 maxima (0, $\frac{\pi}{2}$, π, $\frac{3\pi}{2}$) and 4 minima ($\frac{\pi}{4}$, $\frac{3\pi}{4}$, $\frac{5\pi}{5}$, $\frac{7\pi}{4}$) where the intensity value is respectively I_0 and $(1 - \frac{2-\sqrt{2}}{4})I_o \approx 0.854\, I_0$.

Ellipticity by small phase delay A linearly polarized beam, with respect to a generic choice of the axes, can be represented as

$$\vec{E} = E_0 \begin{pmatrix} cos\theta \\ sin\theta \end{pmatrix} e^{i(kz-\omega t)} \tag{D.13}$$

where the time and spatial varying component is also reported. If the phase offset between the $\hat{p}$ and $\hat{s}$ components is not exactly 0, the polarization is not linear anymore, but starts to be elliptical. If the phase offset is $\frac{\pi}{2}$ and the amplitude of the two components is the same, polarization is circular.

The beam splitters had the collateral effect of acting as retardation plates, adding a small phase angle to one polarization with respect to the other one. In the interferometer's setup (see figure 3.1) both BS1 and BS2 are hit by a 45° (with respect to their intrinsic axis) linearly polarized beam, and make it slightly elliptical. This means that if the exiting beam is sent into a half-wave plate and a polarizer, it is not possible anymore to extinct it. I report the demonstration: indeed the resulting output electric field is the resulting product of a 45° linearly polarized beam, the beam splitter (neglecting the reflectance), a half-wave plate and a polarizer. Matrices are applied in the inverse order as the math requires.

$$\vec{E}(\theta,\delta) = \begin{pmatrix} 1 & 0 \\ 0 & 0 \end{pmatrix} \begin{pmatrix} cos2\theta & sin2\theta \\ sin2\theta & cos2\theta \end{pmatrix} \begin{pmatrix} 1 & 0 \\ 0 & e^{i\delta} \end{pmatrix} \frac{E_0}{\sqrt{2}} \begin{pmatrix} 1 \\ 1 \end{pmatrix} \tag{D.14}$$

The resulting intensity is

$$I(\theta,\delta) = \frac{I_0}{2}\left(1 + sin(4\theta)cos(\delta)\right) \tag{D.15}$$

If $\delta = 0$, by varying the θ angle one can obtain both total transmission or null transmission by the polarizer. But if $\delta \neq 0$ this is not possible. By inverting this relation at the minimum for the transmitted intensity, I obtained

$$cos(\delta) = 1 - 2\frac{I}{I_0} \tag{D.16}$$

which is the relation I used to characterize the ellipticity of the polarization and the behavior of the BS. A 45° polarized beam was sent to the BS and I tried to extinct it using a PBS and a half-wave plate. If the beam is linearly polarized, the minimum transmitted intensity is determined by the extinction ratio of the PBS. When the minimum transmitted intensity was higher than that stated by the extinction ratio, I inferred δ from the minimum transmitted intensity obtained turning the half-wave plate. Measurements are reported in section E.3.

Appendix E

Optics Characterization

Here I report the measurement results and procedures I followed to characterize the optics used in the interferometer. The measured parameters are crucial for the analysis of the experimental data.

E.1 Power Beam Splitter Lambda Research Optics NPB-25.4B-R1064-50 used as BS1

A non polarizing beam splitter nominally splits an incoming beam of intensity I_{beam} in two same intensity beams of intensity $I_{beam}/2$. In the realistic cas this is not true, and the reflected and transmitted intensities are respectively (equation E.1)

$$I_{reflected} = r_{BS}^2 I_{beam} \qquad I_{transmitted} = t_{BS}^2 I_{beam} \tag{E.1}$$

where the reflectance and transmitted parameters are squared since they refer to the electric field, and $I_{beam} \propto |E|^2$. I measured r_{BS}^2 and t_{BS}^2 of the beam splitter when the incoming beam was linearly p-polarized and s-polarized. The setup is reported in figure E.1:

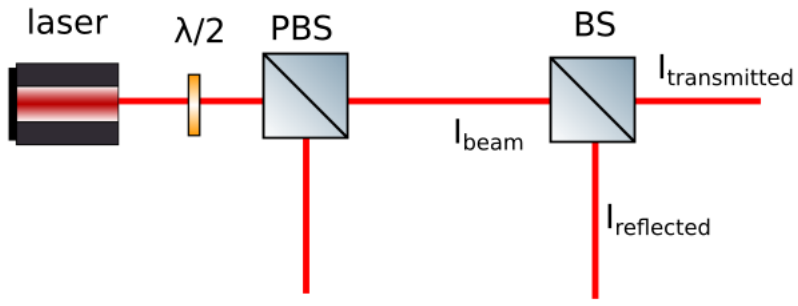

Figure E.1: Setup for the measurement of the BS's reflectance and transmission coefficients in each polarization.

The half-wave plate is used to set the beam's polarization, and hence vary the transmitted or reflected intensity. $\hat{p}$ characterization is measured using he beam transmitted by the PBS, and $\hat{s}$ characteristics are measured using the reflected beam. The intensities of the incident beam to the BS, of the transmitted beam by the BS and of the reflected beam from the BS were measured. The measurements were linearly fitted using equation E.1. The fits are reported in figure E.2. Results are in table E.1. F

Coefficient	Measured
$r^2_{BS,\hat{p}}$	(47.56 ± 0.02) %
$t^2_{BS,\hat{p}}$	(50.04 ± 0.02) %
$r^2_{BS,\hat{s}}$	(43.31 ± 0.05) %
$t^2_{BS,\hat{s}}$	(53.72 ± 0.05) %

Table E.1: Non-Polarizing Beam Splitter *Lambda Research Optics NPB-25.4B-R1064-50* Transmission and Reflectance in $\hat{p}$ and $\hat{s}$ polarizations.

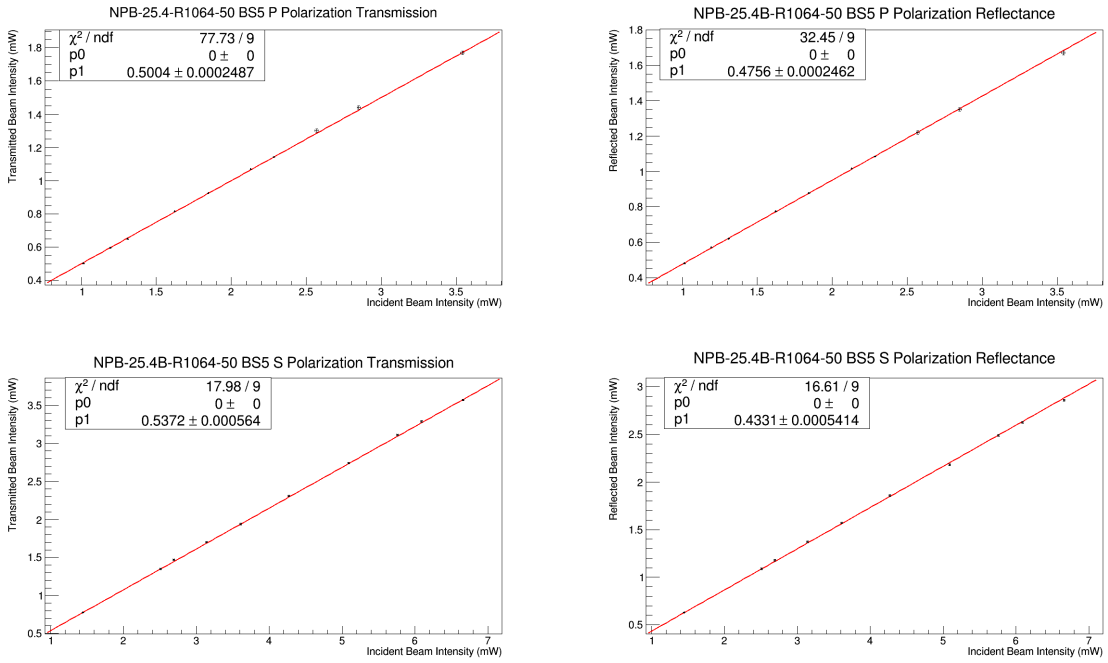

Figure E.2: Non-Polarizing Beam Splitter *Thorlabs BS5* Transmission and Reflectance in $\hat{p}$ and $\hat{s}$ polarizations.

E.2 Power Beam Splitter Lambda Research Optics NPB-25.4B-R1064-50 used as return interceptor

This Non Polarizing Beam Splitter has been characterized in the same way as the one above. Measurements and fits are reported in figure E.3, results are reported in table E.2.

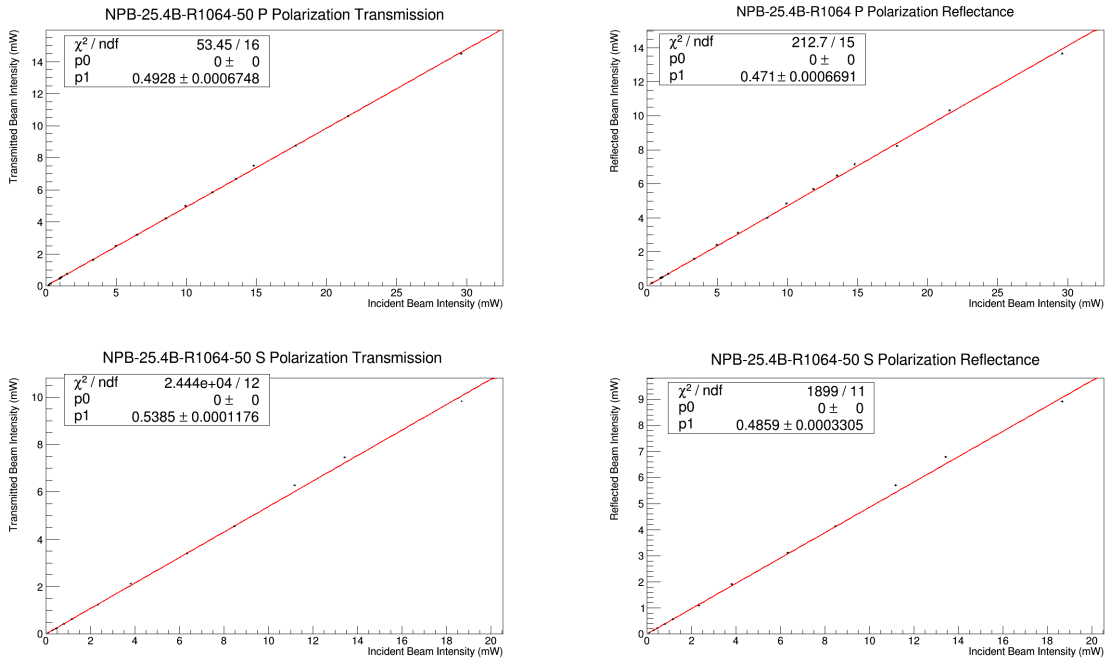

Figure E.3: Non-Polarizing Beam Splitter *Lambda Research Optics NPB-25.4B-R1064-50* Transmission and Reflectance in $\hat{p}$ and $\hat{s}$ polarizations.

Coefficient	Measured
$r^2_{BS,\hat{p}}$	(47.10 ± 0.07) %
$t^2_{BS,\hat{p}}$	(49.28 ± 0.07) %
$r^2_{BS,\hat{s}}$	(48.59 ± 0.03) %
$t^2_{BS,\hat{s}}$	(53.85 ± 0.01) %

Table E.2: Non-Polarizing Beam Splitter *Lambda Research Optics NPB-25.4B-R1064-50* Transmission and Reflectance in $\hat{p}$ and $\hat{s}$ polarizations.

E.3 Phase Offset induced by the Beam Splitters

We have characterized the interferometer's $\hat{p}$ and $\hat{s}$ outputs when the octal wave-plate was not inserted, and the input beam was polarized at a 45° angle. We noticed that there was a phase offset between the two outputs, which was not expected to be there, since the two independent beams in the two polarizations were supposed to behave in the same way. I found out that the Beam Splitters adds a phase to one polarization with respect to the other one, behaving so as a wave plate.

This behavior has been accurately characterized in order to minimize it. The used setup is that planned in D, and is reported in figure E.4.

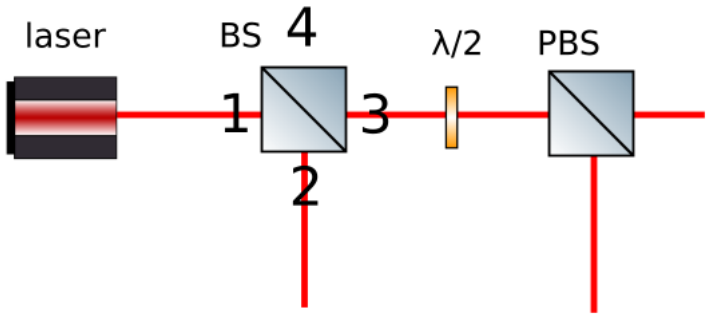

Figure E.4: The used setup for the measurement of the phase induced by the BS.

We were sending to the beam splitter, as it happens in the interferometer, a 45° linearly polarized beam with respect to the vertical axis. We were then controlling if both the reflected and transmitted beam were still linear, by adding a half wave plate and a PBS: if the beam is still linearly polarized, then the half-wave plate is capable of turning the polarization into $\hat{s}$, and the PBS will not transmit more than its maximum extinction ratio which is 1:1000. If instead a phase has been added to $\hat{s}$ with respect to $\hat{p}$, then the polarization is not linear, and half-wave plate and PBS is not be capable of extincting the beam, and the minimum transmitted intensity will give information about the phase offset between the two polarizations. I computed this in equation (D.16), which I remind here:

$$\Delta\phi = arccos\left(1 - 2\frac{I_{\min}}{I}\right) \tag{E.2}$$

Where $\frac{I_{min}}{I}$ is the measured extinction ratio obtained using half-wave plate and PBS. The beam transmitted by the PBS is then monitored with the power meter. We measured this property for all of the four possible ways of entering the BS. Here are what we obtained for the two BS:

Position	Transmission Extinction ratio	Offset(deg)	Reflection Extinction ratio	Offset(deg)
1	0.003%	6.3	<0.001%	<3.6
2	0.002%	5.2	0.003%	6.3
3	0.002%	5.2	0.009%	11
4	<0.001%	<3.62	0.006%	8.9

Table E.3: Phase Offset induced to one polarization with respect to the other one by transiting through the BS1.

Position	Transmission Extinction ratio	Offset(deg)	Reflection Extinction ratio	Offset(deg)
1	<0.001%	<3.6	0.002	5.2
2	<0.001%	<3.6	<0.001%	<3.6
3	<0.001%	<3.62	0.022%	17
4	<0.001%	<3.62	0.021%	17

Table E.4: Phase Offset induced to one polarization with respect to the other one by transiting through the BS2.

Then we decided to set the first beam splitter in the interferometer since the induced phase offsets were smaller. Computations state that BS2 can induce no offset to the inter-

ferometer, so its worse performance does not matter. The offset is due to the different phase offsets induced by the two different paths of tea transmitted and reflected beams along the two arms of the interferometer, and hence to the interferometer beam splitter BS1. After checking which was the non linearity of a beam being both transmitted and reflected by BS1, we measured that these two effects are cumulating (and not canceling), and we computed that the phase offset due to this effect along the beam's path is

$$\Delta\phi = (6.3 + 6.3 - 8.9 - 5.2)^\circ = -1.5^\circ \tag{E.3}$$

This offset sums up with that due to the octal wave-plate.

E.4 Aluminum Reflectance Characterization

E.4.1 Aluminum Surface

I measured the reflectance of an aluminum surface polished in the same way as the bottom surface of the oscillator, which we as using as mirror in one of the two arms of the interferometer. The reflectance was measured using an incident linearly polarized beam, in order to test if the reflection by the aluminum preserves the input polarization. I report the used setup in figure E.5:

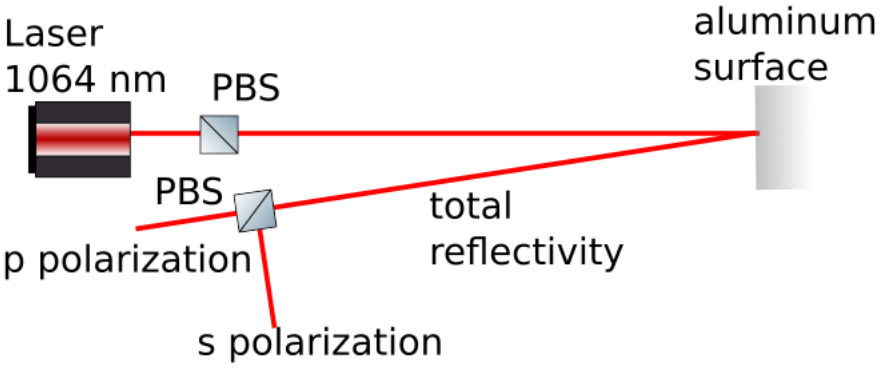

Figure E.5: Aluminum Reflectance measurement setup.

I performed the measurement using a $\hat{p}$ polarized beam (selected using a PBS). The reflected beam's intensity was measured both directly and both decomponed in it's $\hat{p}$ and $\hat{s}$ components, using a second PBS. The residual $\hat{s}$ polarization in the incident beam was also checked, in order to measure the PBS polarization quality. The measurement was performed in the two different incidence angles, 45° and 2.2° (which is the smallest incidence angle I could reach).

I figured out that when the beam's incidence angle was of $\sim 45^\circ$, polarization was not preserved, while when the incidence angle was very small, polarization is preserved. The ratios of the reflected beam and the incident beam are reported in table E.5.

E.4.2 Oscillator's Surface Reflectance

I measured the reflectance of the oscillator's bottom surface at an angle as close to 0°. The measuring setup used is the same as the one shown previously in E.5. Two mirrors in between to reflect the beam vertically. I measured the same quantities as in section E.4.1, varying the

angle	p(%)	s(%)	total(%)
45 °	$r^2_{\hat{p}\to\hat{p}} = 0.491$	$r^2_{\hat{p}\to s} = 0.399$	0.894
2.2°	$r^2_{\hat{p}\to\hat{p}} = 0.874$	$r^2_{\hat{p}\to s} = 0.006$	0.878

Table E.5: Aluminum surface's reflectance at a $\hat{p}$ polarized beam at various angles.

indicent beam's intensity. I plotted the reflected beam's intensity versus the incident beam's intensity and performed a linear fit with null intercept. The result is $r_2^2 = 0.920 \pm 0.04$ (see figure E.6):

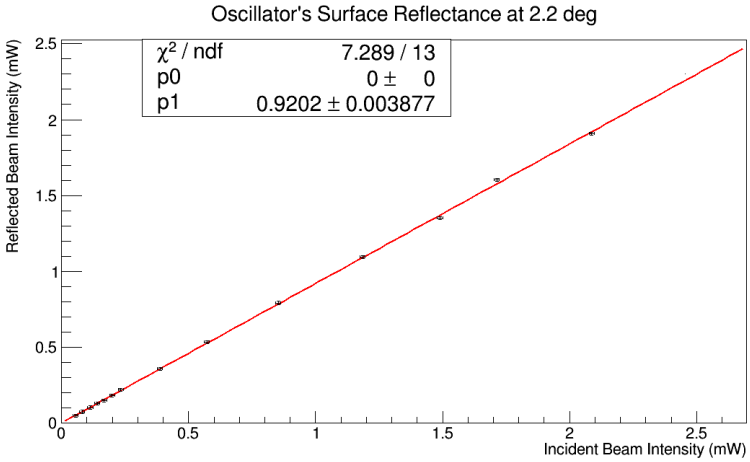

Figure E.6: The aluminum oscillator's fit.

Hence the oscillator's reflectance is slightly different than the surface one. This coefficient is of fundamental use for the 4PDR.

E.5 Reference Mirror Reflectance

I measured the reflectance of mirror 1 at it's working angle of 0°. I followed the same procedure a in the case of the oscillator's surface in section E.4.2. The measured reflectance is $r_1^2 = 0.998 \pm 0.001$ (see figure E.7).

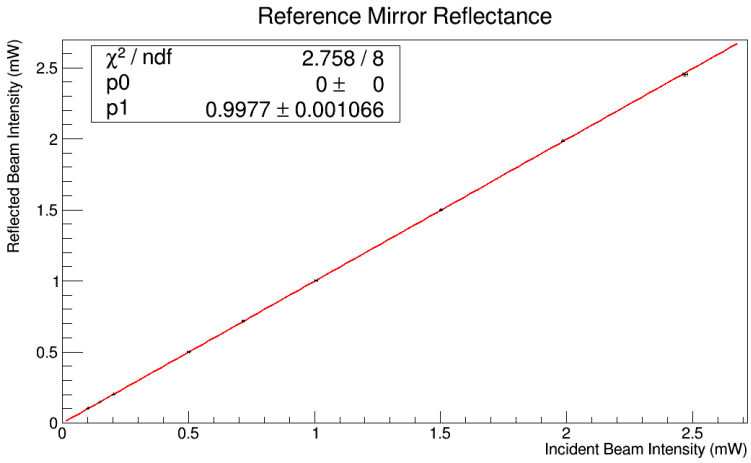

Figure E.7: The reference mirror's reflectance

E.6 The Octal-Wave Plate

I characterized the behavior of the octal-wave plate at various angles, by sendint into it a 8.87 mW $\hat{p}$ polarized beam. I checked the output beam's polarization components using a PBS and the power meter using the setup in figure E.8. I measured the minima and the maxima of the transmitted intensity by the PBS. The expected transmitted intensity as a function of the octal-wave plate's rotation angle is reported in equation (D.12). Measurements are reported in table E.6.

angle (deg)	PBS transmission (mW)
5±0.5	8.87 ±0.01
44±0.5	7.88 ±0.01
88±0.5	8.87 ±0.01
135±0.5	7.20 ±0.01
182±0.5	8.82 ±0.01
226±0.5	7.90 ±0.01
268±0.5	8.82 ±0.01
318±0.5	7.25 ±0.01

Table E.6: Measurement of the octal-wave plate behavior at various angles. The angles refer to the rotator the octal-waveplate was mounted on.

The measured values are not equally spaced by a 45° angle as equation D.12 states. As evident, the octal waveplate exhibits 4 compatible maxima values, and on the other hand exhibits 2 distinct couples of minima, none of them compatible with the expected value:

$$\frac{I_{min,1}}{I_0} = \frac{7.89}{8.87} = 0.8895 \neq 0.854 \qquad \frac{I_{min,2}}{I_0} = \frac{7.20}{8.87} = 0.8117 \neq 0.854 \tag{E.4}$$

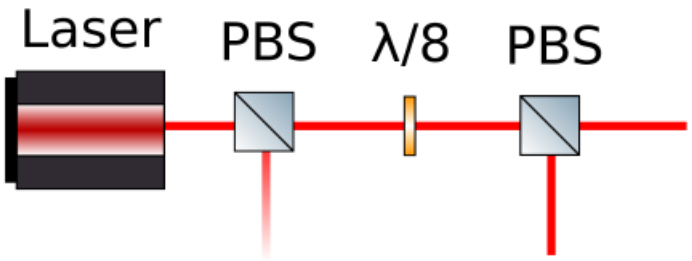

Figure E.8: Scheme of the experimental setup used for the characterization of the octal-wave plate

However, the average value of the two is close to the expected value: $0.8506 \sim 0.854$. This means that the octal waveplate is adding a phase delay[1] $\phi_2 = 50.94°$ if working at the angles 135° and 318°, and a different phase delay $\phi_1 = 38.83°$ if working at the angles 44° and 226°.. None of this two values is equal to the desired $\frac{\pi}{4}$ phase delay, and the two angles differ from 45° by $\sim 6°$. This is why the optimal phase delay of $\pi/2$ between the two interferometer's outputs cannot be reached experimentally and this effect has to be corrected during the data analysis. By aligning the waveplate's angle to one polarization, the two interferometers should be ofset by an $\sim 90° \pm 12°$ angle according to the above measurements. The correction angle is $\sim 24°$ and hence twice the angle extimated by this reasoning.

[1]This value can be computed with the same relation used for the BS delay, equation(D.16).

E.7 The Photodiodes Calibrations

During the test with the piezo mirror (section 4.3) three photodiodes were used. I will refer to with the names of PDTR3, PDZ and PDB. These photodiodes operate with a voltage supply of ± 12V. The calibrations are reported here (figurw E.9):

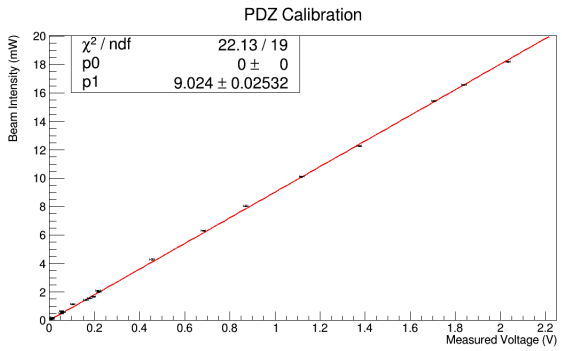

(a) PDZ calibration.

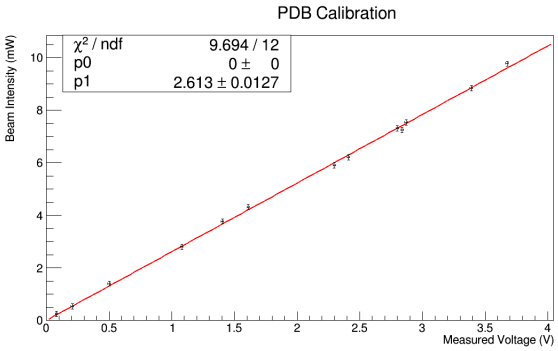

(b) PDB calibration.

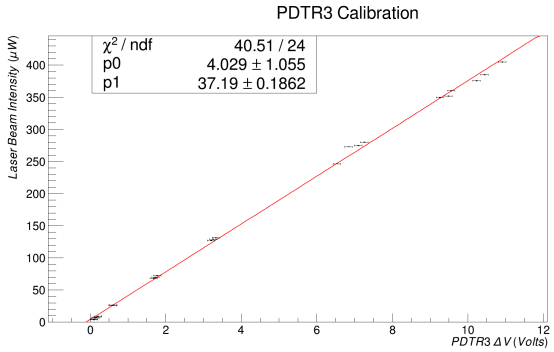

(c) PDTR3 calibration.

Figure E.9: The old photodiodes' calibration

The final setup of the experiment requires the use of five photodiodes. Three new photodiodes built in EGO[2] were available since may, and these were named SN7, SN8, SN9, SN10 and SN11. The EGO photodiodes work with a voltage supply of ± 15V and a bias voltage of 15V. For the final interferometer's setup, SN7 is used in FMP, SN9 is used in FMS, SN8 is used in RMP and SN10 is used in RMS. SN11 is used as input intensity monitor. The calibrations are in figure E.10:

The new photodiodes by EGO work particularly better than the old ones, so a good improvement for the experiment would be the substitution of the older photodiode.

[2]European Gravitational Observatory

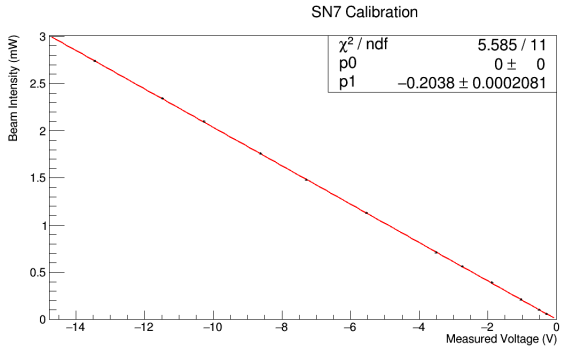

(a) SN7 calibration

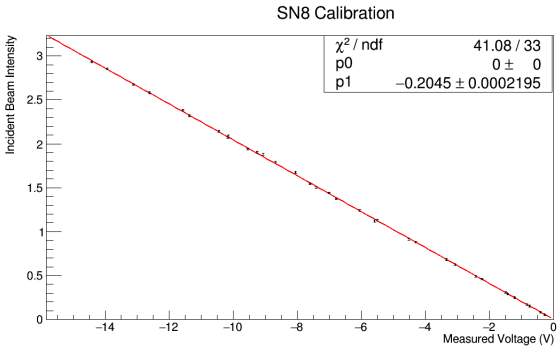

(b) SN8 calibration

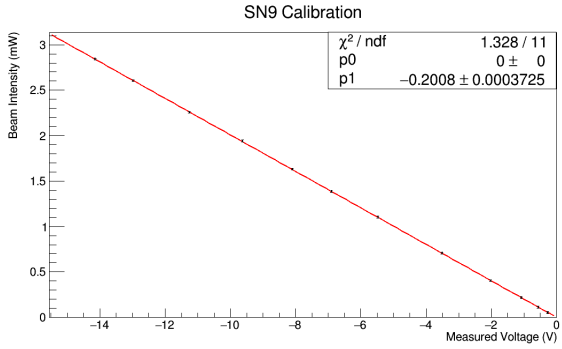

(c) SN9 calibration

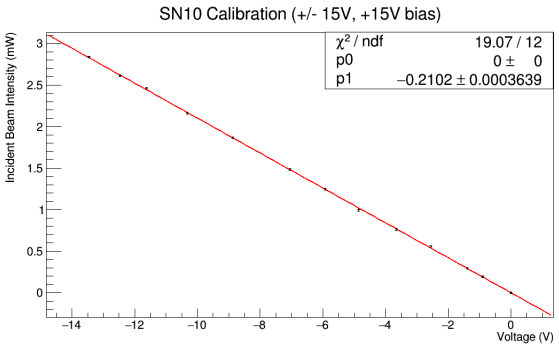

(d) SN7 calibration

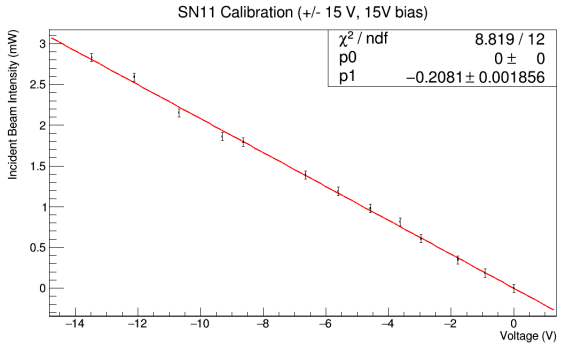

(e) SN8 calibration

Figure E.10: The EGO photodiodes' calibration.

Bibliography

[1] Odylio Denys Aguiar, *The Past, Present and Future of the Resonant-Mass Gravitational Wave Detectors*, Instituto Nacional de Pesquisas Espaciais, Divisão de Astrofísica, San Paolo, Brazil https://arxiv.org/pdf/1009.1138

[2] J. Weber *Detection and Generation of Gravitational Waves* Phys. Rev. 117, 306 – Published 1 January 1960

[3] Abadie et al, *All-sky search for gravitational-wave bursts in the second joint LIGO-Virgo run* The LIGO Scientific Collaboration and The Virgo Collaboration https://arxiv.org/abs/1202.2788

[4] *Measurements of mechanical thermal noise and energy dissipation in optical dielectric coatings* Tianjun Li et al, 1) Université de Lyon, Laboratoire de physique, ENS Lyon, CNRS, Lyon 69364, France 2)Laboratoire des Matériaux Avancés (LMA), IN2P3/CNRS, Université de Lyon, F-69622 Villeurbanne, Lyon, France 2014 https://arxiv.org/pdf/1401.0184.pdf

[5] *Gravitational-Wave Tests of General Relativity with Ground-Based Detectors and Pulsar-Timing Arrays* Nicolás Yunes and Xavier Siemens Living Rev. Relativity, 16 (2013) https://arxiv.org/abs/1304.3473

[6] *Gravitational waves from a binary black hole merger observed by LIGO and Virgo* The LIGO Scientific Collaboration and The Virgo Collaboration

[7] *Gravitational Waves - Volume 1 - Theory and Experiments* Michele Maggiore Oxford University Press 2008

[8] *General Relativity: an Introduction for Physicist* M.P. Hobson, G. Efstathiou, A. N. Lasenby Cambridge University Press 2006

[9] *A compact, passive setup for a low vibration noise measurements in the frequency and (300-2000) Hz* Mario Saraceni, Michele Bonaldi, Lorenzo Castellani, Livia Conti, Abdul Basheed Gounda, Stefano Longo and Matteo Pegoraro

[10] *LISA (Laser Interferometer Space Antenna* https://lisa.nasa.gov

[11] *LIGO (Laser Interferometer Gravitational-Wave Observatory)* https://www.ligo.caltech.edu

[12] *Thermal noise in mechanical experiments* Peter R. Saluson, Joint Institute for Laboratory Astrophysics, National Institute of Standards and Technology and University of Colorado, Boudler, Colorado 80309-0440 8 June 1990 Phys. Rev. D (42) (8)

[13] *Effects of Breaking vibrational energy euipartition on measurements of temperature in macroscopic oscillators subject to heaf flux* Livia Conti, Paolo De Gregorio, Gagik Karapetyan, Claudia Lazzaro, Matteo Pegoraro, Michele Bonaldi and Lamberto Rondoni

[14] *Non-equilibrium "thermal noise" of low loss oscillators* G. Karapetyan, D. Agguiaro, M. Bonaldi, L. Castellani, R. Hajj, C Lazzaro, D. Mazzaro, M. Pegoraro, C. Poli, R. Thakur, L. Conti

[15] *Pulsar timing arrays* R. N. Manchester CSIRO Astronomy and Space Science, PO Box 76, Epping NSW 1710, Australia

[16] *Gravitational radiation from cosmic (super)strings: Bursts, stochastic background, and observational windows* Thibault Damour and Alexander Vilenkin Phys. Rev. D 71, 063510 – Published 11 March 2005

[17] *Fisica Sperimentale del Campo Gravitazionale* G. Pizzella La Nuova Italia Scientifica, 1993

[18] *Observation of Gravitational Waves from a Binary Black Hole Merger* B. P. Abbott et al. (LIGO Scientific Collaboration and Virgo Collaboration) Phys. Rev. Lett. 116, 061102 – Published 11 February 2016

[19] *GW151226: Observation of Gravitational Waves from a 22-Solar-Mass Binary Black Hole Coalescence* B. P. Abbott et al. (LIGO Scientific Collaboration and Virgo Collaboration) Phys. Rev. Lett. 116, 241103 – Published 15 June 2016

[20] *INTEGRAL IBIS, SPI, and JEM-X observations of LVT151012* V. Savchenko et al

[21] *GW170814: A Three-Detector Observation of Gravitational Waves from a Binary Black Hole Coalescence* B. P. Abbott et al. (LIGO Scientific Collaboration and Virgo Collaboration) Phys. Rev. Lett. 119, 141101 – Published 6 October 2017

[22] *GW170817: Observation of Gravitational Waves from a Binary Neutron Star Inspiral* B. P. Abbott et al. (LIGO Scientific Collaboration and Virgo Collaboration) Phys. Rev. Lett. 119, 161101 – Published 16 October 2017

[23] *Multi-messenger Observations of a Binary Neutron Star Merger* LIGO Scientific Collaboration, Virgo Collaboration, Fermi GBM, INTEGRAL, IceCube Collaboration, AstroSat Cadmium Zinc Telluride Imager Team, IPN Collaboration, The Insight-Hxmt Collaboration, ANTARES Collaboration, The Swift Collaboration, AGILE Team, The 1M2H Team, The Dark Energy Camera GW-EM Collaboration, the DES Collaboration, The DLT40 Collaboration, GRAWITA: GRAvitational Wave Inaf TeAm, The Fermi Large Area Telescope Collaboration, ATCA: Australia Telescope Compact Array, ASKAP: Australian SKA Pathfinder, Las Cumbres Observatory Group, OzGrav, DWF (Deeper, Wider, Faster Program), AST3, CAASTRO Collaborations, The VINROUGE Collaboration, MASTER Collaboration, J-GEM, GROWTH, JAGWAR, Caltech- NRAO, TTU-NRAO, NuSTAR Collaborations, Pan-STARRS, The MAXI Team, TZAC Consortium, KU Collaboration, Nordic Optical Telescope, ePESSTO, GROND, Texas Tech University, SALT Group, TOROS: Transient Robotic Observatory of the South Collaboration, The BOOTES Collaboration, MWA: Murchison Widefield Array, The CALET Collaboration, IKI-GW Follow-up Collaboration, H.E.S.S. Collaboration, LOFAR Collaboration, LWA: Long Wavelength Array, HAWC Collaboration,

The Pierre Auger Collaboration, ALMA Collaboration, Euro VLBI Team, Pi of the Sky Collaboration, The Chandra Team at McGill University, DFN: Desert Fireball Network, ATLAS, High Time Resolution Universe Survey, RIMAS, RATIR, SKA South Africa/MeerKAT

[24] *Lasers* Anthony E. Siegman, Stanford University 1986

[25] *Quadrature Phase Interferometer for high resolution force spectroscopy* Pierdomenico Paolino, Felipe A. Aguliar Sandoval and Ludovic Bellon

[26] *Introduction to Matrix Methods in Optics (1st ed.)* Gerald, A.; Burch, J.M. (1975).

[27] *Irreversibility and generalized noise* H. Callen and T. Welton, , Phys. Rev.83, 34 (1951)

[28] *RareNoise: non-equilibrium effects in detectors of gravitational waves* L. Conti, M. Bonaldi and L. Rondoni 2010

[29] *A compact, large-range interferometer for precision measurement and inertial sensing* S. J. Cooper, A. C. Green, C. Collins,D. Hoyland, C. C. Speake, A. Freise and C. M. Mow-Lowry

[30] *Just an other mode Matching tool* Developers: A. Thüring and N. Lastzka http://www.sr.bham.ac.uk/dokuwiki/doku.php?id=geosim:jammt

[31] *Piezo Technologes - Non Linearity of voltage-dependent displacement curves in piezo actuators* https://www.piceramic.com/en/piezo-technology/properties-piezo-actuators/displacement-behavior/